Development and Characterization of the OSIRIS USASK Observatory

A Thesis
Submitted to the Faculty of Graduate Studies and Research
in Partial Fulfillment of the Requirements
for the Degree of
Master of Science
in the Department of Physics and Engineering Physics

by
Michael Stoicescu
Saskatoon, Saskatchewan

©Copyright

For Lena Mulder and Beatrice Voegeli.

Abstract

The OSIRIS instrument on board the Odin satellite uses limb viewing techniques to measure scattered sunlight and so determine the vertically resolved concentrations of atmospheric constituents including ozone. Initially, a proof of concept instrument was built and tested. This instrument, the Developmental Model, is now housed at the third floor clean room of the Physics Building on the University of Saskatchewan campus.

The Developmental Model was incorporated into a system designed to monitor scattered sunlight above Saskatoon. The system was set up to transmit skylight to the Developmental Model using a fiber optic cable and to perform all measurements automatically and with minimal user interaction. The system was calibrated to determine the pixel to wavelength response. Characterizations of the point spread function and relative intensity response of the detector were also made. A shutter system was designed and constructed to measure the detector dark current. An enclosure was built on the top of the Physics Building to provide a weather proof environment and so allow data collection throughout the year. Zenith sky measurements were taken during twilight hours to provide information on the depth of absorption in the Chappuis band, an indicator of the total ozone column. The absorption depth was converted to a Dobson Unit measurement for the ozone column.

Analysis of collected data provides two conclusions. The first is that a measurement set in the presence of clouds shows different signatures than a clear measurement set. The second conclusion is the detection of a diurnal trend in the total ozone column with greater amounts measured in the morning. The OSIRIS USASK Observatory is now operational and collecting data for future analysis of scattered sunlight measurements above Saskatoon.

Acknowledgements

I would like to thank the Institute of Space and Atmospheric Studies at the University of Saskatchewan for the opportunity to further my education and learn from some of the greatest minds in their fields. Ted Llewellyn deserves many thanks for supervising and overseeing my project, always challenging my mind and ensuring that I considered all aspects to a problem and all possible solutions.

Thanks to Adam Bourassa who, under expense of his own time, would willingly help with any problems I encountered, including much help with computer code and even a little carpentry. I am greatly appreciative of his selflessness in giving his own time to help my understanding of everything from atmospheric science to a myriad of different programming problems.

Also deserving thanks are Nick Lloyd and Reid McDonald. Nick, like Adam, also had no problem helping with my programming troubles and general physics problems. I put in a few sleepless nights with Reid in our quest together to complete our thesis projects and his knowledge and friendship was greatly enjoyed throughout our work together.

Lastly, a big thank you must be extended to Doug Degenstein. His wealth of knowledge and great leadership are the reason I have taken so much from our work together. His commitment to his students, his intelligence, and his easy-going nature have made him an ideal supervisor and I am proud to have had the guidance of such a great scholar and great person.

Contents

List of Figures

List of Tables

Glossary of Terms

BUV	Backscatter UltraViolet
CCD	Charge Coupled Device
DM	The OSIRIS Developmental Model
DN	Digital Number output from the OSIRIS Developmental Model
GOME	Global Ozone Monitoring Experiment
GOMOS	Global Ozone Monitoring by Occultation of Stars
GUI	Graphical User Interface
MODTRAN	MODerate spectral resolution atmospheric TRANsmittance algorithm and computer model
MLS	Microwave Limb Sounder
OSIRIS	Optical Spectrograph and InfraRed Imager System
ROE	ReadOut Electronics
SCIAMACHY	SCanning Imaging Absorption spectroMeter for Atmospheric CHartographY
SZA	Solar Zenith Angle
TOMS	Total Ozone Mapping Spectrometer
UV	UltraViolet radiation

Chapter 1

Introduction

1.1 Introduction

The scattering, transmission, and absorption of solar radiation by the Earth's atmosphere has been used for many years to study the composition of the atmosphere. Minor chemical species such as O_3 (ozone) and NO_2 (nitrogen dioxide) are identified via their absorption features in the observed spectrum while aerosols are detected by the broad spectral shape modifications associated with Mie scattering processes.

Ozone is an important component of the Earth's atmospheric chemistry as it absorbs most of the solar UltraViolet (UV) radiation (in the Hartley-Huggins bands). Without ozone, the Earth's surface would be bathed in UV radiation that causes biological damage such as sunburns, cataracts, and melanoma.

In this thesis the design of a ground-based optical facility that is housed in the Physics Building and built around the Developmental Model (DM) for the OSIRIS (Optical Spectrograph and InfraRed Imager System) instrument on the Odin satellite is described. This facility allows the acquisition of calibrated spectra of scattered sunlight across the entire visible region and the near infrared (267-810 nm). The primary objective of the present work is the design and construction of the optical facility and its use to study radiative transfer processes within the atmosphere. This is demonstrated through measurements of the ozone density at sunrise and sunset over Saskatoon for a one year period using the ozone Chappuis absorption feature between 400 and 650 nm.

1.2 Ozone Background

The Earth's atmosphere undergoes natural ozone fluctuations depending on the time of day, time of year, and geographic location. Experimental measurements of the atmosphere lead to the development of models that can predict how atmospheric constituents react with each other and their local concentrations at various places around the globe. An improved knowledge of ozone distributions helps improve existing models and contributes to a better understanding of atmospheric processes. In particular it is important to understand the relationship between ozone and other chemicals in the atmosphere in order to determine anthropogenic effects on the natural ozone cycle.

Ozone is dispersed throughout the stratosphere and mesosphere and in an unpolluted atmosphere is created through the 3-body recombination of atomic oxygen and molecular oxygen,

$$O_2 + O + M \rightarrow O_3 + M. \tag{1.1}$$

A theory for the formation and destruction of ozone in the atmosphere was initially proposed by *Chapman* [1930] in his seminal Bakerian lecture to the Royal Society in London.

1.2.1 Chapman Photochemistry

In the Chapman theory, molecular oxygen is photodissociated by solar UV light with wavelengths less than 242 nm,

$$O_2 + h\nu \ \ (\lambda < 242 \ \ \mathtt{nm}) \rightarrow 2O. \tag{1.2}$$

The resultant atomic oxygen reacts with another oxygen molecule and a third body, usually O_2 or N_2, to form ozone,

$$O_2 + O + M \rightarrow O_3 + M. \tag{1.3}$$

The third body, M, is required for the conservation of energy and momentum. The formed ozone molecule can then follow one of two paths. It is either photodissociated

back to $O_2 + O$ through the absorption of a photon,

$$O_3 + h\nu \rightarrow O_2 + O, \tag{1.4}$$

or it can combine with an oxygen atom to form two oxygen molecules. If the O_2 photodissociation product is in an excited state then absorption in the Hartley band (< 310 nm) is the responsible process. If the O_2 product is in the ground electronic state then the photo-absorption is in the Chappuis band (< 770 nm). The reaction with atomic oxygen, Equation 1.5,

$$O_3 + O \rightarrow 2O_2, \tag{1.5}$$

can be described as a form of neutral dissociation recombination. The measurement of the ozone column is recorded in Dobson Units [*Dobson et al.*, 1929]. A Dobson unit is defined as a $1/100^{th}$ mm high column if the ozone column is compressed to standard temperature and pressure. Thus, if the entire atmospheric column was at a temperature of $0°C$ and atmospheric pressure a 3 mm thick ozone column would correspond to 300 Dobson Units. It is of value to note that compressing the atmosphere to standard temperature and pressure results in a total vertical air column of about 7 km. A typical measurement for the ozone column is approximately 200 Dobson Units at the equator and increases with latitude to about 300 Dobson Units over Europe [*Chapman*, 1930]. The ozone density also varies with season as it exhibits a maximum in spring and a minimum in the fall. Figure 1.1 shows a typical vertical distribution of ozone above 10 km for Saskatoon. These data were obtained by the OSIRIS instrument.

Ozone in the atmosphere is mainly between 10 and 35 km with a maximum in the 20-25 km region; this peak altitude is latitude dependent. Ozone is not present in large quantities above 35 km due to the increased solar UV flux that rapidly dissociates ozone according to Equation 1.4. There is little ozone production below 20 km, as the required solar UV radiation, Equation 1.2, has been absorbed at higher altitudes. Thus there is little atomic oxygen production and so less ozone production. Ozone lifetimes are less than an hour (3100 s) in the stratosphere, at 32 km, and increase to weeks or months in the lower stratosphere and troposphere between 10 and 20 km [*NASA*, 2005]. This ozone lifetime gradient causes the ozone

concentration to be dominated by photochemical processes above the ozone peak at 25 km and by transport mechanisms below the peak. There are three main transport mechanisms that drive the global circulation of ozone; the Brewer-Dobson circulation, planetary waves, and tropospheric folding. These transport mechanisms cause ozone from equatorial latitudes to be dispersed to mid and high latitudes, as well as allowing ozone rich stratospheric air into the troposphere.

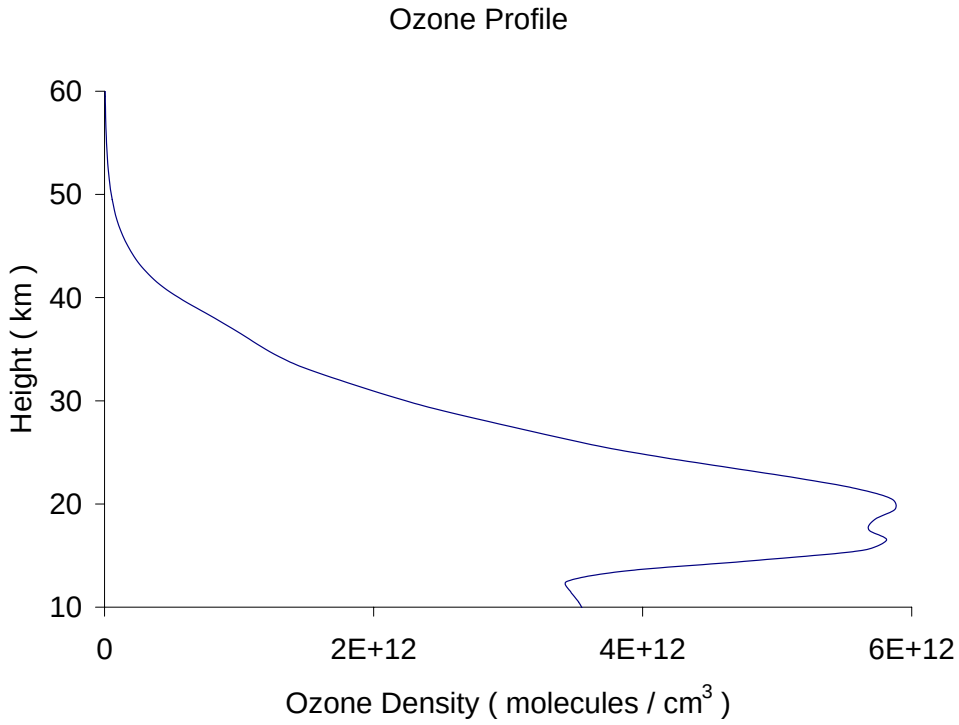

Figure 1.1: The vertical distribution of ozone as measured with OSIRIS above Saskatoon[*Degenstein*, Private Communication]. Note the peak in the ozone density at 21 km.

1.3 Ozone Measurement Background

Ozone can be measured in a variety of different ways with numerous instruments that measure absorption in the solar spectrum, the thermal radiation signature of ozone, or through the chemical reaction of ozone (e.g. optical, radiometric, ozone

sonde). The instruments used for ozone measurement operate from different platforms; satellite, rocket, balloon, or ground-based. The main optical techniques include Backscatter UltraViolet (BUV), occultation, and limb scattering. These techniques require the measurement and analysis of a spectrum to determine the ozone amount. Measuring spectral features to determine ozone amounts requires knowledge of the unattenuated spectrum for comparison with the collected measurements. With a satellite the unattenuated spectrum is measured when the radiation source is observed outside the atmosphere. For a ground based instrument this is not possible and some other method for the determination of the unattenuated spectrum is required.

1.3.1 The Dobson Spectrophotometer

The Dobson Spectrophotometer determines the total ozone column by measuring the spectral intensity at two close wavelengths ($\sim$ 20 nm difference) that have different ozone absorption coefficients [*Dobson*, 1957]. The ratio of the measured signals at these two wavelengths is designed to cancel any attenuation due to aerosols and Rayleigh extinction and leave only the attenuation due to ozone absorption. The instrument was initially designed by *Dobson* [1931] and can be used to make either direct sun measurements or scattered sunlight measurements for analysis with the Umkehr method [*Gotz et al.*, 1934]. A double quartz spectrometer is used to isolate the absorption bands used in the absorption ratio. The ratio is determined by allowing radiation from the two wavelengths to be incident consecutively on a photoelectric cell by means of a rotating sector wheel. As one of the wavelengths is more intense than the other it is reduced in intensity through an optical absorption wedge. When the beams have equal intensity the attenuation introduced by the wedge is a measure of the ozone absorption. The Umkehr method involves measuring the absortion at sunrise and sunset in order to determine the vertical distribution of ozone in the atmosphere, albeit with a low altitude resolution.

The Dobson Spectrophotometer has been used for many years and there has been a network of instruments around the globe in order to monitor long term ozone trends. In an effort to maintain precision and accuracy among the different instruments they are all calibrated against the same instrument. Dobson Spectrophotometer 83 [*Komhyr and Grass*, 1989] has been used both directly and indirectly to

calibrate at least 100 different instruments worldwide, in some cases many times, and has been designated the primary standard Dobson Spectrophotometer for the world. As this instrument was developed in the 1930's, the available technology was quite limited. For example, quality assurance for the optical wedge, which is subject to variation with time, introduces uncertainty in the measurements and so justifies the need for the global calibration standard. Advances in technology led to the development of the Brewer Spectrophotometer [*Brewer*, 1973], which was intended as a replacement for the aging Dobson Spectrophotometer.

1.3.2 The Brewer Spectrophotometer

The Brewer Spectrophotometer, designed in 1973, removes the need for an optical wedge by using a photomultiplier tube to measure the incident photon flux. *Dobson* [1957] found that there is a significant increase in the accuracy of the ozone measurements if two wavelength pairs are used instead of the standard one pair. The Brewer Spectrophotometer incorporates this improvement by measuring four different wavelengths in a near simultaneous fashion and so allows for six different wavelength pairs to be measured. This redundancy results in an increased precision for the measurements. There is another advantage for the Brewer Spectrophotometer over the Dobson Spectrophotometer. The Dobson technique is sensitive to any changes in the atmosphere and it is possible for an appreciable change in the intensity of radiation before the optical wedge has been adjusted for the second intensity. The Brewer design measures the four separate wavelengths, one at each time, by covering three of the four slits and storing the photo-generated charge for the relevant wavelength bin. This slit is then covered and a different slit exposed. The photo-generated charge is again measured and stored in the appropriate wavelength bin. Each wavelength is cycled through before repeating the entire cycle in order to accumulate charge in each of the wavelength bins. An exposure time of 28 ms [*Brewer*, 1973] is used for each bin and it takes 128 ms to complete the cycle and expose all the wavelengths. This is done for a maximum of 512 cycles ($\sim$ 1 min) and the accumulated signals are used to determine the ratio of intensities and so calculate the column concentration of ozone.

1.3.3 Backscatter UltraViolet

The BUV method, which necessarily requires a satellite platform, uses two pairs of measurements to determine the total ozone column. Incoming and backscattered light is measured at two wavelengths, one that is strongly absorbed by ozone and one that is weakly absorbed. The measurements using the weakly absorbing wavelength are considered as the control case and yield the signal that is expected for no ozone absorption. The difference in absorption between the strong and weak absorption wavelengths gives the total ozone column. Good horizontal resolution can be obtained with this method but there is a limited vertical resolution capability. The Global Ozone Monitoring Experiment (GOME) was launched in 1995 and provides a horizontal resolution of 40 x 320 km^2 using the BUV method for data collection [*Burrows et al.*, 1999]. The BUV technique is also used with the Total Ozone Mapping Spectrometer (TOMS) [*Krueger et al.*, 1995]. Various forms of this instrument have collected total column ozone data since 1978; the measurement approach used six fixed wavelength bands between 312 and 380 nm.

1.3.4 Occultation

The occultation technique is primarily a satellite-based technique but has been investigated by *Mcdonald* [2006] for a ground-based platform application. The instrument on board the satellite looks through the atmosphere at the sun, moon, or a star and tracks the radiation source as it rises or sets. The unattenuated signal is taken by measuring the spectrum of the source as the line of sight is above the atmosphere. The comparison of the unattenuated signal with that obtained when the line of sight passes through the atmosphere yields the ozone column. The vertical resolution of this technique is about 1-2 km [*Nett et al.*, 2001]. The requirement for the radiation source to rise or set restricts the data collection for any given celestial object to twice per orbit. Thus it takes many orbits to match the spatial coverage of the BUV technique. GOMOS (Global Ozone Monitoring by Occultation of Stars) on board ENVISAT was launched in 2002 and tracks rising stars through the atmospheric limb and so provides an improved global coverage from that possible with solar occultation. The GOMOS ozone measurements extend over the altitude range from 15-80 km [*Nett et al.*, 2001].

1.3.5 Limb Scattering

The limb scattering technique uses scattered sunlight to measure the absorption of ozone and other gases in the atmosphere. This technique is similar to occultation as it has a similar viewing geometry and gives good vertical resolution. The approach is also similar to the BUV technique as it provides coverage throughout the entire sunlit atmosphere. The instrument SCIAMACHY (SCanning Imaging Absorption spectroMeter for Atmospheric CHartographY) uses the limb scatter technique to measure trace gas vertical profiles. The limb scattering technique is also the one used by OSIRIS to measure ozone, NO_2, sulphate aerosols, and other minor species [*von Savigny et al.*, 2003]. OSIRIS was one of two instruments launched on board the Odin satellite in 2001. The OSIRIS instrument measures limb-scattered sunlight in order to determine the vertical and spatial distribution of ozone as well as of other trace gases. The OSIRIS Developmental Model was designed and built as a precursor to the flight model in order to test the instrument and to facilitate design optimization.

1.3.6 Other Ozone Measurement Techniques

Other ozone measurement techniques that are used but are less relevant to this thesis include ozone sondes and limb emission. An ozone sonde is a method that measures the vertical distribution of ozone by physically lifting the measuring device into the stratosphere by means of balloon or rocket. There are two type of ozone sondes that employ optical and electro-chemical methods to measure ozone. For the spectrograph device the column concentration as a function of height is differentiated to determine the local concentration. This technique has limited accuracy at low heights, where the amount of ozone is small compared to the total ozone column, so the change with respect to height is small and the measurements are inaccurate. An electro-chemical device that interacts with atmospheric ozone was used in the place of a spectrograph by *Brewer and Milford* [1960] in the Oxford-Kew Ozone Sonde. This device used iodine to react with ozone to produce electrically charged ions, which can be collected and used to determine the amount of ozone present.

The limb emission technique uses long wavelength infrared or microwave radiation, which is thermally emitted in the atmosphere, to measure the amount of ozone along the line of sight. This viewing geometry is very similar to that for

the occultation technique but the technique itself is quite different. Limb emission depends on the thermally generated emissions from trace gases. Good vertical resolution (3 km) is possible with this method but because the path length through the atmosphere is long, the horizontal resolution is compromised. The Microwave Limb Sounder (MLS) on the AURA satellite was launched in 2004 and measures microwave radiation 118-2500 GHz (2500-120 μm) [*Read et al.*, 2006] to determine the concentrations of atmospheric trace gases.

A final technique used with ground-based instruments involves measurements at only one wavelength. Attenuation is measured when the sun is high and when the sun is low, ie. small and large solar zenith angles. It is assumed that there are no differences in the background atmosphere for the two measurements. In this case the difference in the two measurements is due to the different path lengths in the atmosphere. Thus absorption measurements as a function of solar zenith angle (SZA) can be used to retrieve the ozone column [*Flittner et al.*, 2000].

1.4 Thesis Objective

The objective of this thesis work is to design and test an automated system that collects scattered sunlight measurements from the ground during twilight hours using the OSIRIS DM. It is expected that these measurements will create a scattered sunlight data set that can be used to determine trends in atmospheric aerosols and ozone. A preliminary data set has been collected and analyzed as a proof of concept.

1.5 Summary of Thesis

A description of the Developmental Model including the experimental system setup and software design is presented in Chapter 2. The calibrations required to convert the DM's digital numbers (DN) into meaningful line of sight radiances are described and discussed in Chapter 3. A presentation of the radiative transfer as well as the method of determining an ozone concentration are included in Chapter 4. The methods of data analysis as well as the results obtained are described in Chapter 5 and conclusions and recommendations for future work are presented in Chapter 6.

Chapter 2

The OSIRIS USASK Observatory

2.1 Introduction

The OSIRIS USASK Observatory was set up at the University of Saskatchewan to monitor long term trends in scattered sunlight over Saskatoon. It uses the Developmental Model of the OSIRIS instrument to measure scattered sunlight in the local zenith. The DM measures light that originates at the sun, propagates through the atmosphere, is scattered by molecules and aerosols above Saskatoon, and further propagates downward towards the roof of the Physics Building at the University of Saskatchewan. The changing solar zenith angle causes differing amounts of absorption due to differing path lengths through the atmosphere. The DM was developed as a precursor to the flight model in order to determine any design modifications needed before putting the instrument in orbit. Previous work was done by *Wilcox* [2002] in retrieving the DM from ROUTES Inc. in Ottawa and setting it up in the clean room of the Physics Building at the University of Saskatchewan. Wilcox also designed a dark current removal system based on the temperature of the detector.

The Observatory consists of three sections: front end optics, the DM, and a data storage system. The front end optics collect scattered sunlight in the local zenith, provide a means to block unwanted sky signal, and direct the collected light into the DM. This system consists of a fiber optic cable, a shutter system, and a collimating mirror. The DM collects the redirected photons and produces a digital number proportional to the input intensity. Finally, the data storage system consists of a server computer that commands the DM and a client computer that controls the

server and stores collected data.

The fiber optic cable illustrated in Figure 2.1 is used to transmit the light from the outside to the DM. A shutter has been placed in this chain to eliminate the outside signal and provide a measure of ambient light and thermal signal. The light collected by the fiber optic is reflected by the collimating mirror and incident on the aperture of the DM.

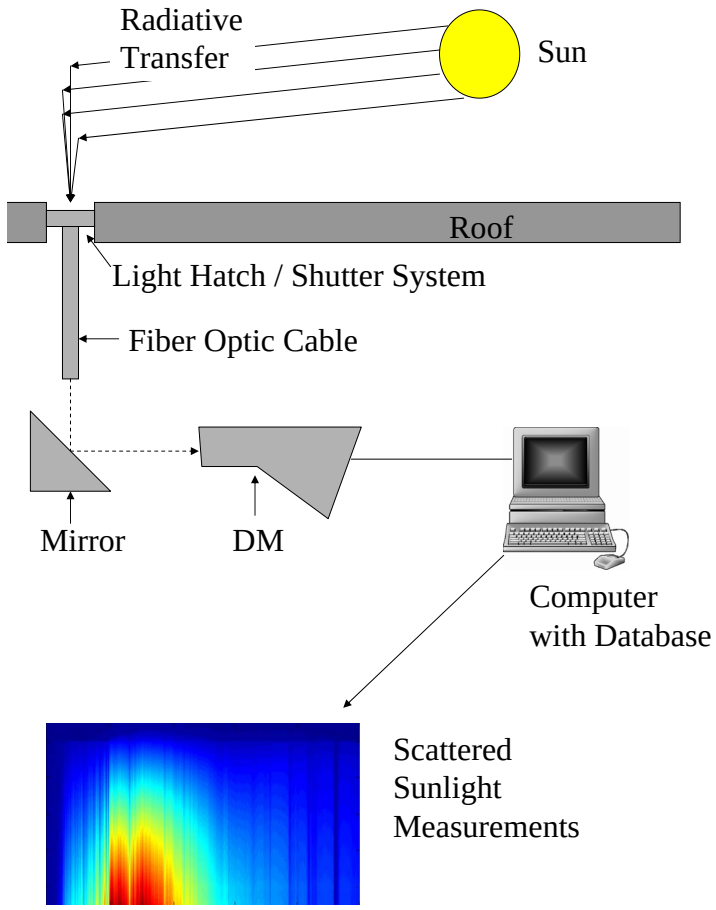

Figure 2.1: General setup of the OSIRIS USASK Observatory.

The DM accepts the input light signal and measures the energy in those wavelengths to which the charge coupled device (CCD) is sensitive, near UV through the visible into the near infrared. The instrument is housed in a clean room on the top floor of the Physics Building to ensure the optics are kept dust free in order to

minimize stray light in the system. Light that is within the small acceptance cone of the DM will pass through the optical chain where its intensity is measured by the CCD and converted to a digital number by the readout electronics (ROE). The DM is described in detail in Section 2.3.

A server computer with a data acquisition program (described in Section 2.4) controls the operation of the DM through a network connection. The server is currently a computer in the clean room with the DM but may be any computer with access to the University network. The server computer sends commands to the DM and receives the collected data back for archival, calibration, and scientific analysis. The interfacing of the system components is shown in Figure 2.2.

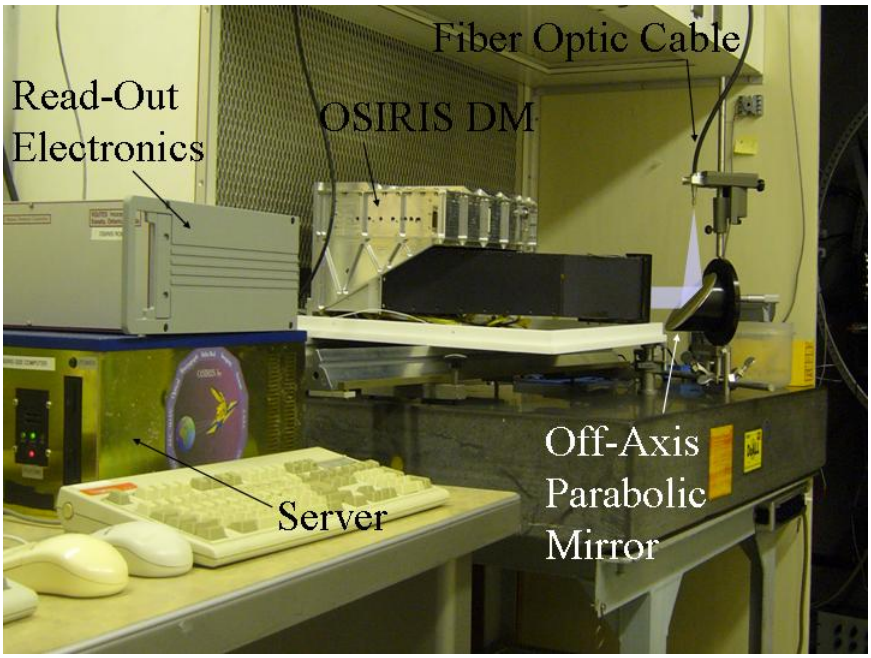

Figure 2.2: Interfacing of system components in the clean room.

2.2 System Setup

The first three components in the system setup are the fiber optic cable for light transmission, the shutter system to exclude any unwanted signal, and the off-axis parabolic mirror to reflect light into the DM. Together these three components form the light collection system setup.

2.2.1 Fiber Optic Cable

A fiber optic cable is used to pipe the collected light into the clean room where the DM is housed. As the DM is a sensitive instrument, this allows it to be kept clean and to reduce unwanted signals. Ideally the DM would be exposed to direct sunlight, however the requirement for a clean environment requires the use of a fiber optic cable. The fiber optic cable must have good transmission throughout the entire wavelength range of the DM.

The DM has a wavelength response that extends from 280 nm in the UV to 800 nm and most fiber optic cables have poor transmission over this wavelength range. The requirement for this broad-band transmission led to the selection of the AS200 from FiberTech Optica. A transmission curve for this cable is shown in Figure 2.3. Between approximately 400 nm and 700 nm the attenuation is small with some

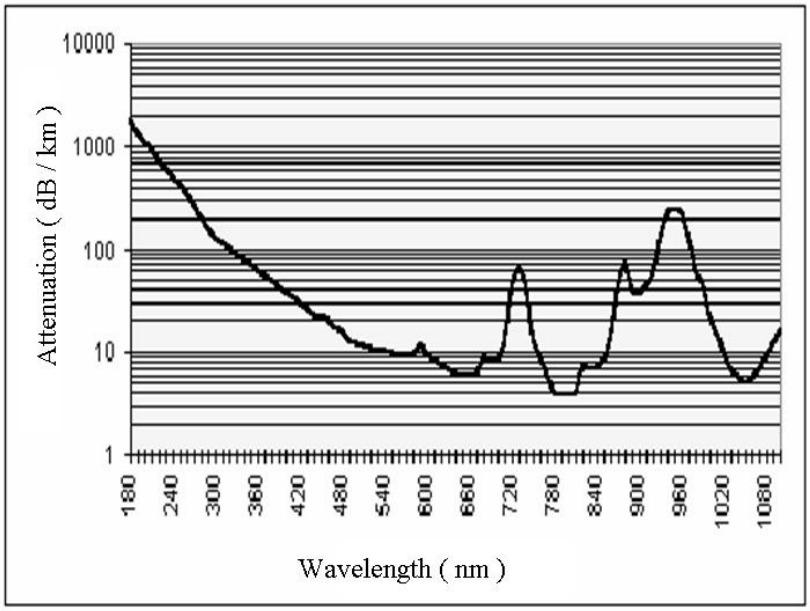

Figure 2.3: Spectral response of the fiber optic cable [*Dupuis*, Private Communication].

structure. In the UV region the attenuation increases and there is a large reduction in the transmission. The AS200 cable is a random bundle of 37 fibers and has a numerical aperture of .22, which translates to an acceptance cone half angle of 12.7°. Each fiber is 200 microns in diameter and the bundle is packed into a hexagonal shape. This results in an active area diameter of 1.54 mm. The fiber optic cable is

shown in Figure 2.4. It is held in place above the off axis parabolic mirror and has a standard SMA-905 connector at each end.

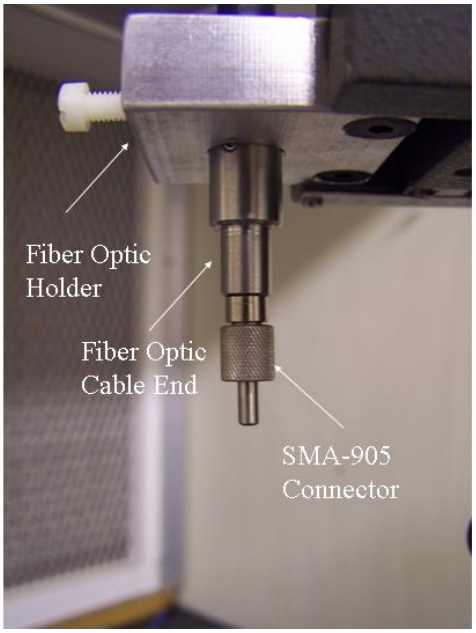

Figure 2.4: The end of the fiber optic cable, showing the SMA-905 connector, secured in place above the mirror.

For any optical system the flux of light through the system is proportional to the light collecting area, A, and the solid angle subtended, Ω. Ideally, a well matched system has identical values of $A \cdot \Omega$. The fiber optic cable was chosen in order to fill the field of view of the DM, which has an acceptance cone of ~ 4 arc minutes and a 2.5 cm square aperture. The $A \cdot \Omega$ value for the DM is given by,

$$A \cdot \Omega = (.025)^2 \left(\frac{2}{60} \cdot \frac{\pi}{180}\right)^2 = 2.115 \text{ x } 10^{-10} \left[m^2 \cdot ster\right], \tag{2.1}$$

while the fiber optic cable has an $A \cdot \Omega$ value of,

$$A \cdot \Omega = \pi \frac{.00154^2}{4} \left[12.7 \cdot \frac{\pi}{180}\right]^2 = 9.152 \text{ x } 10^{-8} \left[m^2 \cdot ster\right]. \tag{2.2}$$

Although these values are not ideally matched, the fiber optic cable transmits a considerably greater amount of light and readily fills the field of view of the instrument.

2.2.2 Shutter System

A shutter system was designed to calibrate unwanted signals such as dark current, DC offset imposed by the readout electronics, and ambient room light. *Wilcox* [2002] characterized the dark current response of the CCD with respect to temperature but concluded that it was also necessary to remove other unwanted signals and more accurately remove the dark current. A shutter system placed at the entrance to the fiber optic cable provides a convenient way of blocking the input signal and allowing measurement of the unwanted signal.

The DACO shutter, illustrated in Figure 2.5, is a small solenoid shutter system from DACO instruments that operates with an input voltage of 12V. It is designed specifically for the aviation industry and is used to activate control flags. Its small size and low power consumption are also appropriate for the present application.

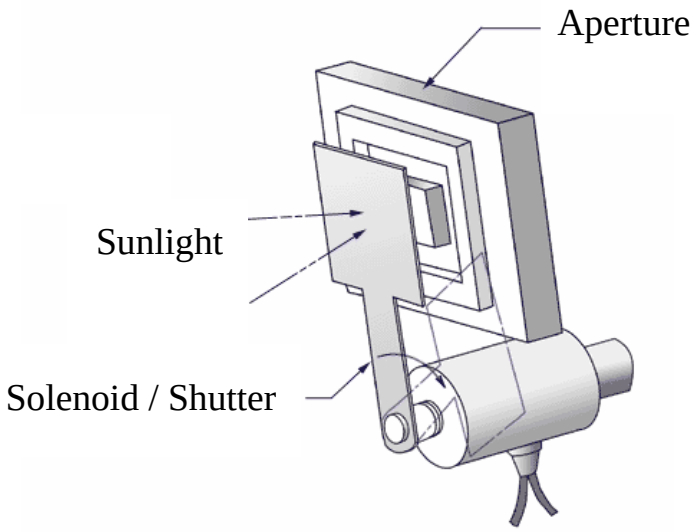

Figure 2.5: DACO shutter.

The shutter is controlled through the printer port on the computer in the clean room. Figure 2.6 shows the control circuitry designed to operate the shutter. If the port is held at +5V, the shutter receives no energy and remains in the open state. If the printer port is forced low the NAND gates change state allowing current to

flow through the shutter solenoid and the shutter is closed. The shutter reacts and changes state in approximately a tenth of a second. The circuitry allows the shutter to be controlled through the 5V printer port and no control of the 12V source is needed. The system is designed to fail open with no power input.

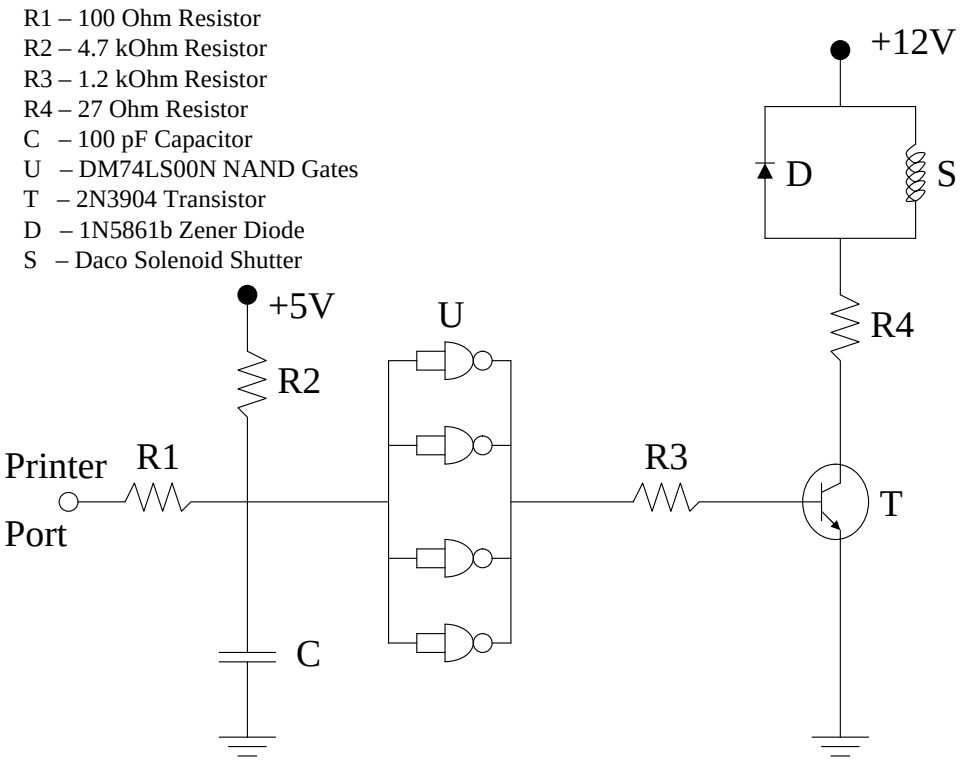

Figure 2.6: Control circuitry for the shutter system.

The shutter enclosure was designed with overlapping shells in order to reduce the amount of unwanted light that could enter the cable through reflections. Figure 2.7 shows a cross sectional view of the overlapping shell system. The cable is fitted into the base where the end fits snugly into the bottom shell, thus blocking any light from underneath. The shutter then slides between this shell and a top shell, providing maximum protection from unwanted light contamination. The entrance to the enclosure on the base was shaped so as to allow the fiber optic cable to be

accurately located each time. Figure 2.8 shows the designed electronics along with the shutter enclosure mounted on a bracket that is attached underneath a quartz window that allows in the zenith skylight. The fiber optic cable attaches through a hole in the bottom and fits snugly into the hole on top of the shutter enclosure. There is just enough clearance between the top of the fiber optic cable and the bottom of the enclosure to allow the shutter to open and close between the two.

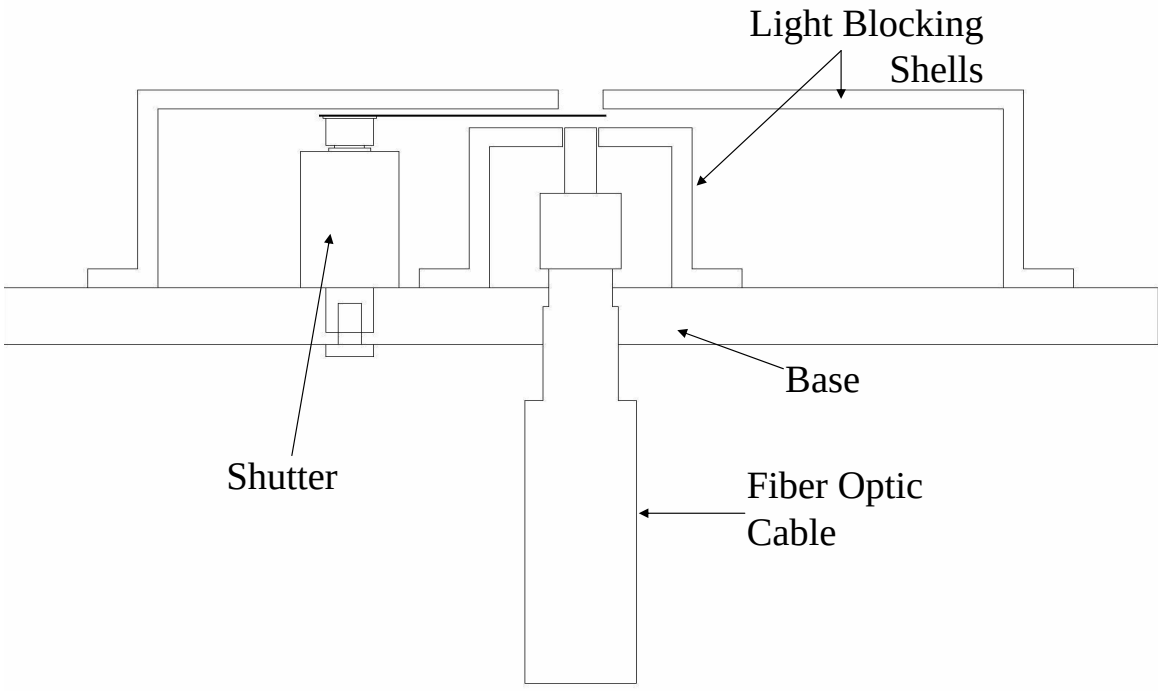

Figure 2.7: Shutter mounting system to block unwanted light.

The enclosure was mounted inside a hatch that opens on to the roof of the Physics Building. A top for the hatch was built to shelter the circuitry and close off the building from the environment. The top was tilted at an angle and holes drilled in the side of the hatch to provide a simple drainage system for rain. In the center of the hatch, a quartz window serves as the entrance point of light for the system and is maintained fog and ice free with a fan mounted on the inside. Figure 2.9 shows the light hatch on top of the Physics Building; the quartz window in the center and

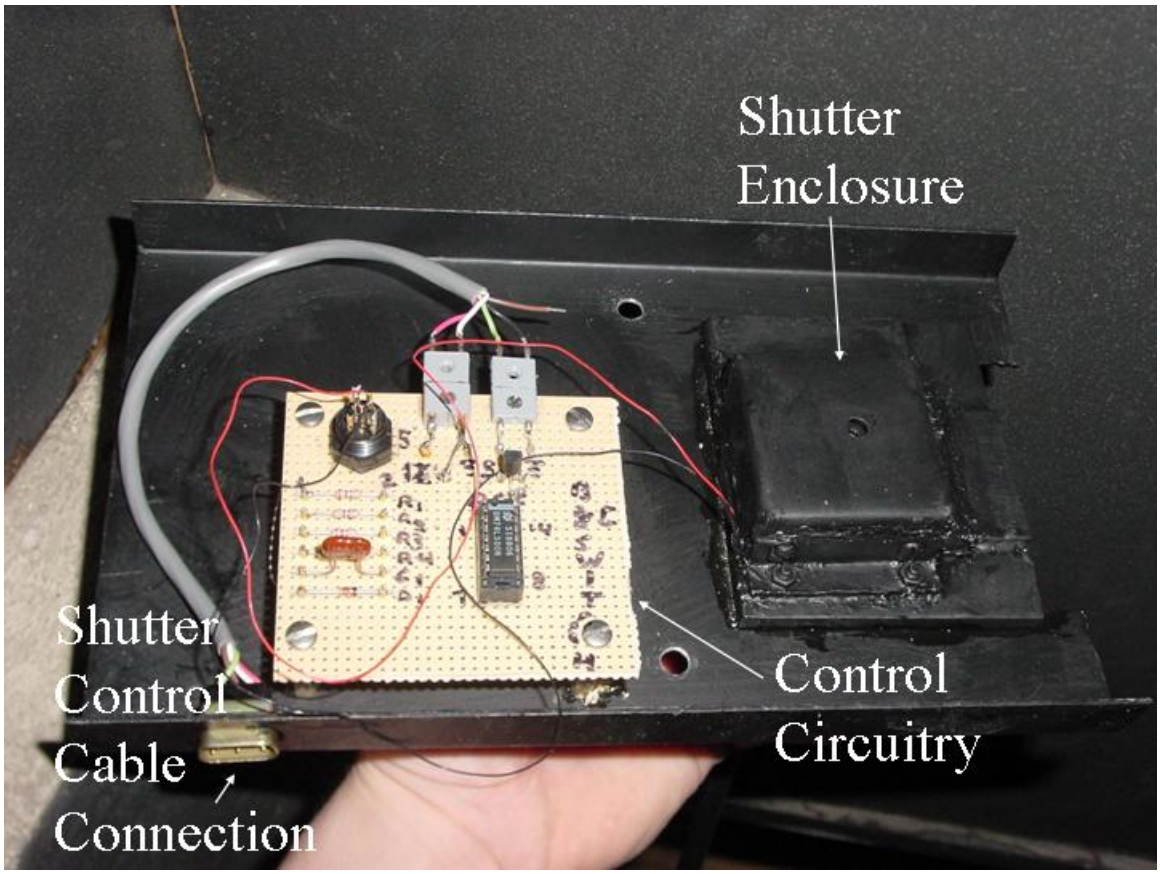

Figure 2.8: Mounted shutter system showing electronics, shutter, and the shutter control cable connection.

the slope down to the drainage holes are clearly apparent. Figure 2.10 shows the same light hatch from below. The fiber optic cable entering the shutter enclosure and the fan that is mounted on the wall and directed towards the quartz window are quite apparent. The shutter control cable is connected between the shutter and the computer so that the shutter may be remotely controlled.

2.2.3 Off-Axis Parabolic Mirror

The off-axis parabolic mirror is needed to produce a collimated light beam and provides the input to the DM. The output of the fiber optic cable is near the focal point of the mirror shown in Figure 2.11, which has a focal length of 152.4 mm. The mirror is mounted to a translational positioner on the optical bench and its orientation is further adjusted using the two additional devices also shown in Figure

Figure 2.9: Light hatch on top of the Physics Building. Note the downward slope and the drainage holes.

2.11.

As this mirror is intended to match the on-orbit light gathering properties of OSIRIS it must be positioned to maximize the signal entering the DM. With such a small acceptance angle ($\sim$ 1 arc min in the vertical direction and $\sim$ 4 arc min in the horizontal direction) the light reflecting off of the mirror must be carefully positioned in order for the fiber optic cable to deliver enough light for measurement.

To maximize the amount of light delivered by the fiber optic cable to the DM, the end of the fiber optic cable must be placed at or very near to the focal point of the mirror. The determination of the focal point was accomplished by using a vertical mirror to reflect light from the parabolic mirror back to the fiber optic cable. A paper was held around the end of the cable and as the distance between the end of the cable and the mirror was changed so as to approach the focal point,

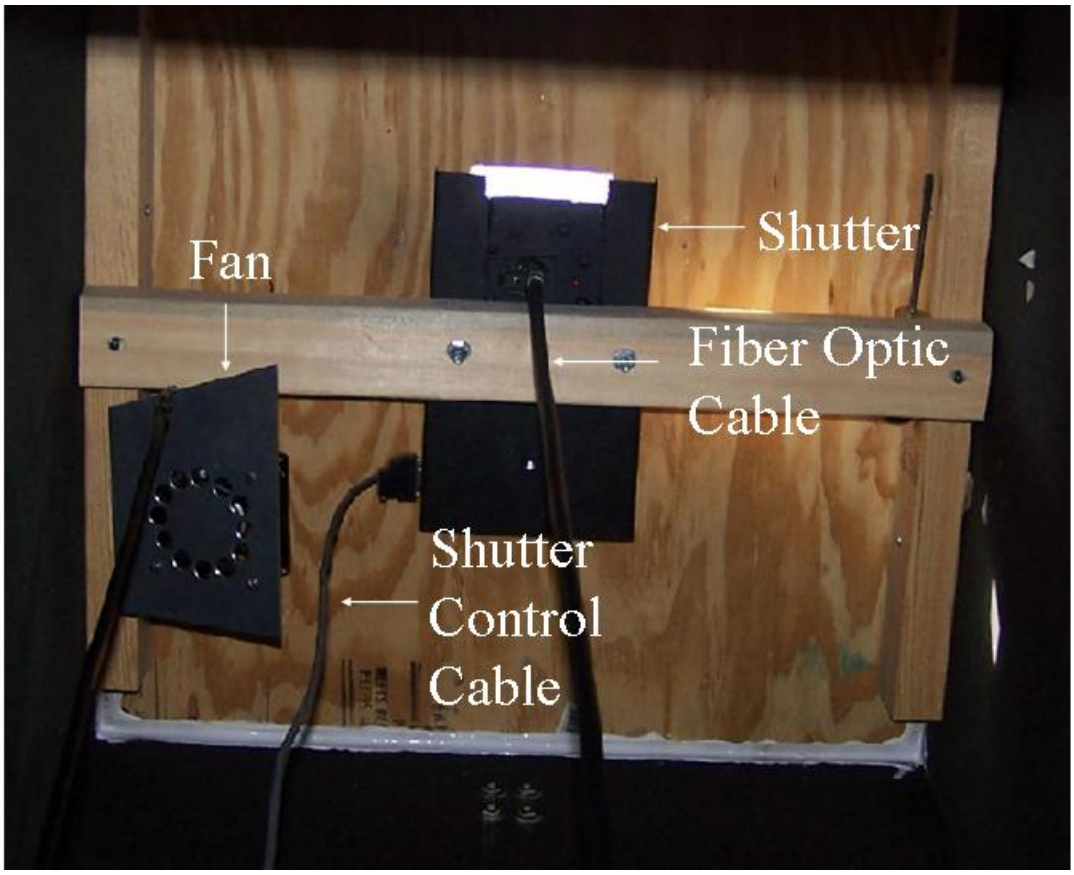

Figure 2.10: Bottom view of light hatch showing shutter system in the middle and fan on the left.

the resultant reflected circle on the paper reduced in size until it was at a minimum. At this point the fiber optic cable was considered to be sufficiently near the focal point. This procedure is shown in Figure 2.12. Any error in the positioning of the fiber optic cable will result in a small signal loss as the light exiting the cable is not perfectly collimated.

Once the focal point has been found, the parabolic mirror must be adjusted so the reflected light beam enters the DM. The fiber optic holder is fixed atop the mirror and as such any movement in the system will not affect the fiber optic placement. The beam of light from the parabolic collimator must be positioned with moderate accuracy in order to be within the acceptance angle of the DM. This alignment was achieved with two positioning devices that allowed small, measurable changes to be made in the position of the output beam. The rotational positioner rotates

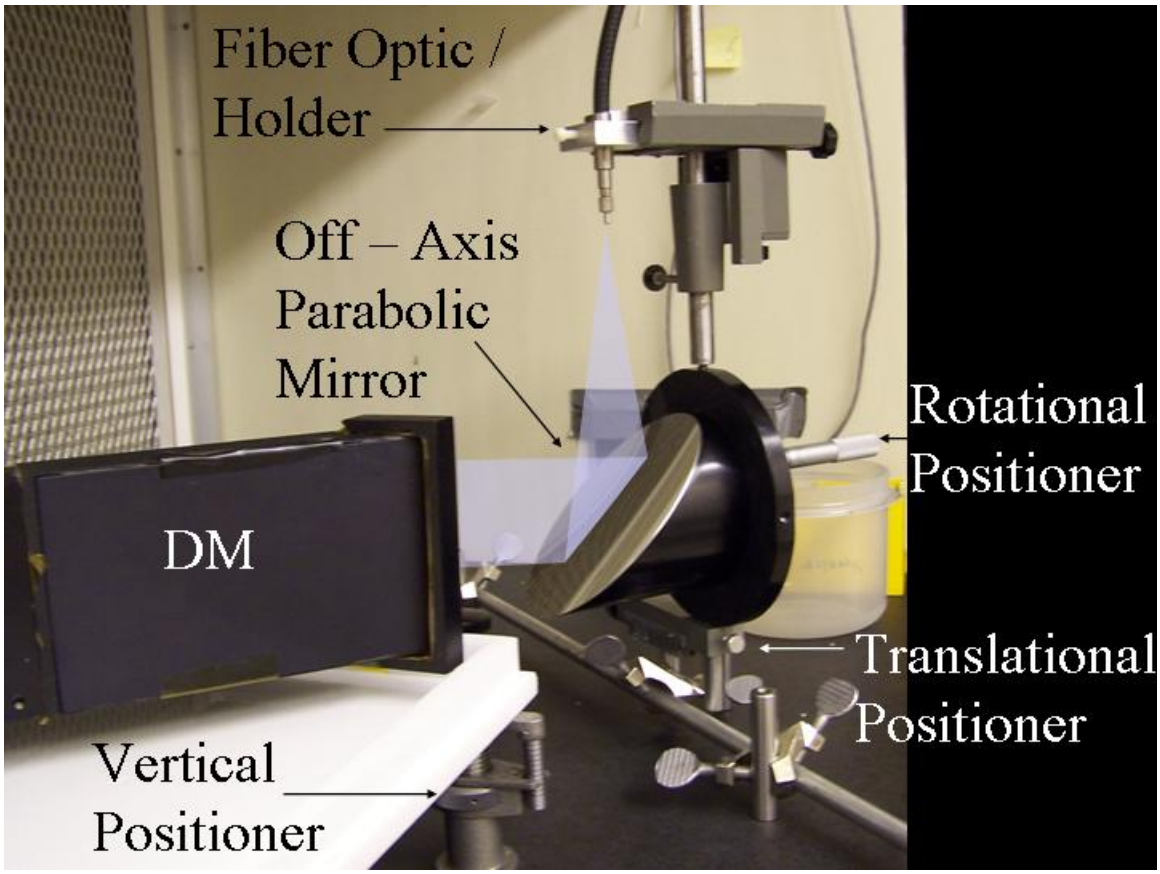

Figure 2.11: Off-axis parabolic mirror.

the parabolic mirror by pushing one side of the mirror. The translational positioner moves the mirror back and forth. There is also a vertical positioner that moves one edge of the DM up or down. Figure 2.11 shows the three positioning devices. In order to position the mirror correctly a computer program was written to continuously expose the CCD and plot the output in real-time. By sweeping the reflected light through the entrance aperture of the DM, using the three positioners, it was possible to watch the CCD go from background to a sky spectrum and back again. The mirror was secured in the position where the CCD signals were maximized.

2.3 The OSIRIS Developmental Model

A schematic diagram of the DM is shown in Figure 2.13. There are two parts to this instrument, an optical spectrograph and an infrared imager system. In the

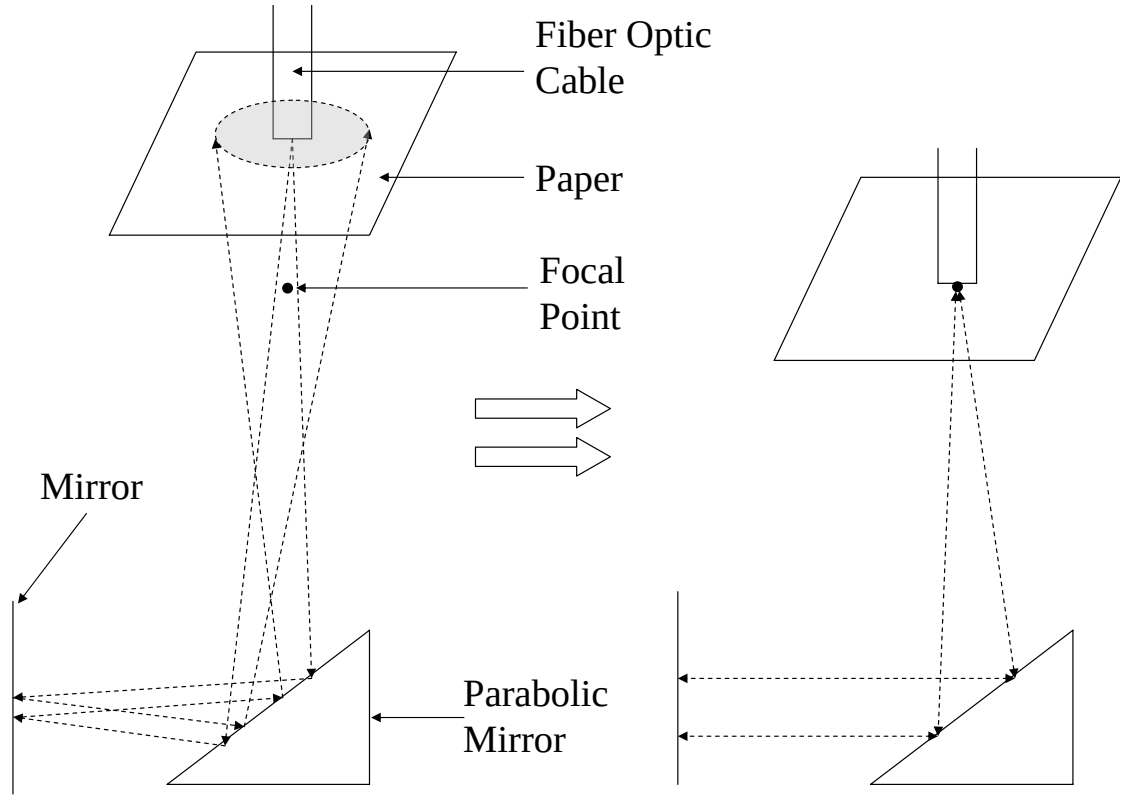

Figure 2.12: Setup for finding the focal point of the mirror by reflection of output light from the fiber optic cable.

present thesis work only the spectrograph is used and makes measurements over the wavelength range 280nm - 810nm. For a complete description of the OSIRIS instrument see *Llewellyn et al.* [2004].

2.3.1 Optical Spectrograph

As light enters the DM its path is controlled by the following optical components: 1) Telescope Mirror, 2) Fold Mirror, 3) Slit, 4) Collimating Mirror, 5) Diffraction Grating, 6) Camera Mirror, and 7) Field Flattener Optical Prism. The spectrally sorted radiation is then incident on a 8) CCD Detector. The accumulated photo-charge is then processed by the detector 9) ROE. The first four elements determine the field of view, the next three elements disperse the incident signal into its wavelength components and focus the radiation on to the CCD, while the final two elements

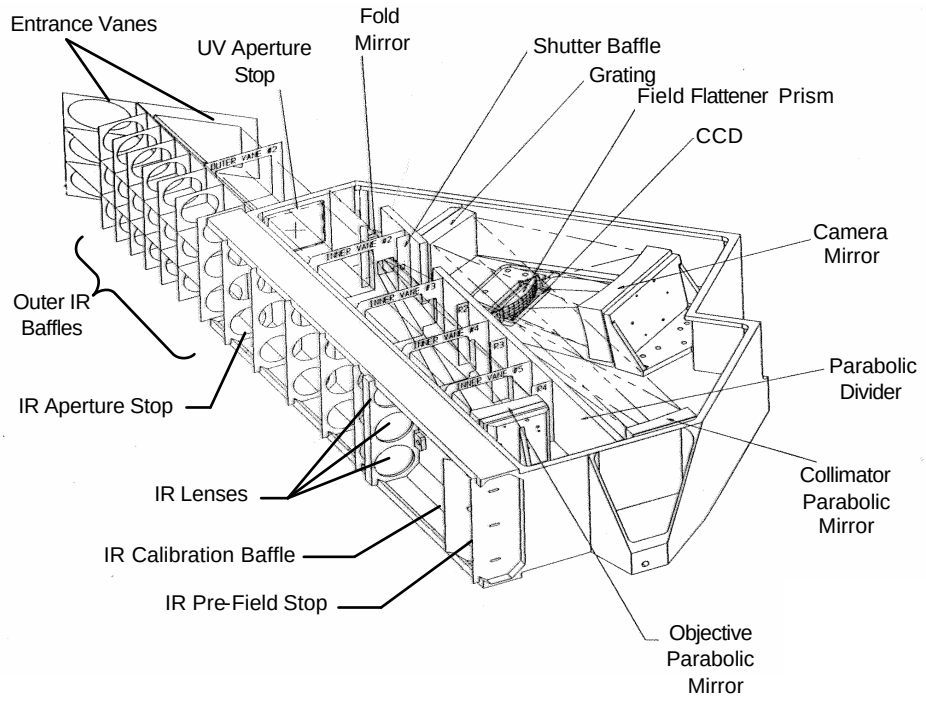

Figure 2.13: Schematic diagram of the OSIRIS instrument.

convert the light to a 14 bit digital number (DN) that can be stored in a computer.

Incident radiation enters the system through the telescope, the fold mirror, and the slit. This restricts the acceptance cone of the instrument by focusing out of field light away from the slit. After passing through the slit the light is incident on a collimator, which restores the original angular distribution. A grating (600 grooves / mm) spectrally separates the component wavelengths and the spectrum is focused by the camera mirror and reflected by the prism before it is imaged onto the CCD. The prism is used to reflect the light through 90° onto the CCD, which is below the optical bench, in order to minimize the amount of internal scattered light.

2.3.2 Charge Coupled Device

The CCD (Figure 2.14), Model CCD26, is a two dimensional array of 1353 pixels by 286 pixels and was designed and produced by E2V Technologies. Approximately 32 rows of the upper half of the CCD are continuously exposed to the incident light

while the bottom half is masked off and so never illuminated. The exposed rows are the image of the entrance slit. When light is incident on the CCD charge accumulates in each pixel in proportion to the number of incident photons. When there is no data acquisition the CCD is continuously flushed of accumulated charge with a clock pulse of approximately 30 μs. When an image is taken, the flushing stops for the exposure time and charge is allowed to build. At the end of the exposure the charge is rapidly clocked into the masked off region (frame shifted) where it is read out into the data storage system.

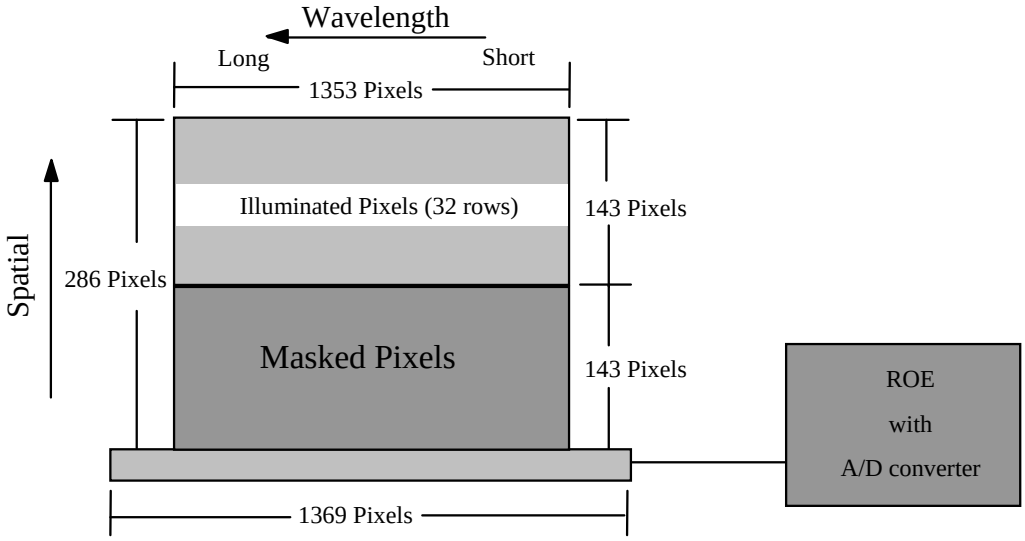

Figure 2.14: Developmental Model's CCD.

The CCD produces thermally generated charge whether it is illuminated or not. This charge production depends on the CCD temperature and is called the dark current. The CCD operates by the promotion of electrons into the conduction band. In order to be promoted the electrons must acquire energy from either incident photons or thermal processes. As the CCD temperature increases so does the average energy of the electrons, thereby promoting greater numbers of electrons into the conduction band even in the absence of incoming photons. The final signal is a digital number that includes a contribution from incident light, thermally generated charge and a DC offset. The incident light can be from either the wanted sky signal

or unwanted ambient room light. Ideally the CCD would be cooled to minimize the effect of dark current, but the inclusion of a shutter system negates the need for cooling.

There are different ROE modes that can be used for reading the CCD and on-chip binning of data. These different modes are used in order to improve the signal to noise ratio. By adding the 32 illuminated pixels on-chip the additional noise introduced by the readout electronics is only imposed upon the measurements once. The first readout mode involves no binning and sends the charge from each of the 32 illuminated rows out to the server computer. The second mode adds two adjacent rows of charge together to get an output of 16 total rows. The third mode combines the charge from 4 rows to get an output of 8 total rows. A final mode bins the charge from 8 rows to produce 4 output rows. This last mode is useful in low light conditions when the signal is small. Each of these binning modes combines charge from the same column of pixels (same wavelength). No matter which ROE mode is selected, all 32 rows of charge are used and sent to an analog to digital converter where a digital number is transmitted to the server computer. For this thesis project, as a demonstration of the facility, only ROE mode 0 has been used; reading all 32 rows with no on-chip binning. This mode can be used because the sky signal is large compared to the readout noise. A full CCD image using ROE mode 0 is shown in Figure 2.15 where the highlighted row is used in the data collection. The CCD has clearly been mounted at an angle with respect to the slit. If the incoming signal was low then an integration across the slit would be performed to increase the signal to noise ratio. However, as measurements were obtained during the day when there was sufficient signal, only row 16 was used as it greatly simplified the data collection without adding significant error to the measurements. This row was chosen as it produces the highest intensity sky signal and is highlighted in Figure 2.15. Its spectral cross section is shown in Figure 2.16 and clearly shows the O_2 A-band absorption as well as the Chappuis and Hartley ozone absorption bands. There is a spike in intensity at pixel 76 that is defined as a hot pixel. The dark current calibration removes this effect.

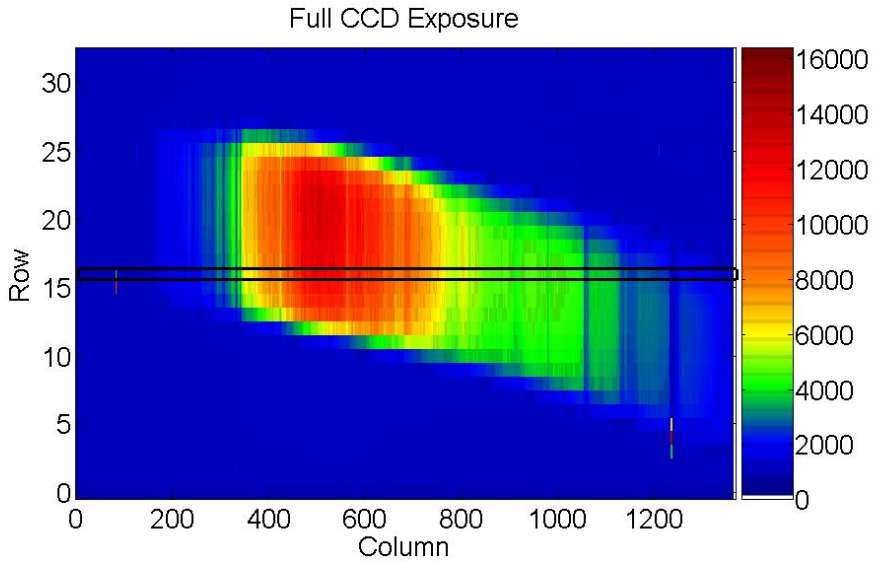

Figure 2.15: Full CCD exposure on March 17th, 2006 at 7:36 AM (SZA = 87°) with emphasis on the row used for data collection. The color scale is in digital number counts.

2.4 Software Design

It is desirable to obtain measurements during the twilight periods as the sun rises or sets. The angle the sun makes with the vertical is known as the Solar Zenith Angle (SZA). Software was designed such that a range of solar zenith angles could be specified and the observatory would automatically turn on with no human interaction. The software also contained a mode that allowed a user to collect images any time they were required.

2.4.1 Software Parameters

The software was designed to meet the requirements that there be minimal user interaction to provide a long term set of sunlight scattered measurements for a range of solar zenith angles daily. This ensured that a consistent, long term data set could be provided without the need for daily supervision of the DM, i.e. remote operation. The software used an ephemeris program to calculate the SZA for the local time and location and the calculated SZA was used to plan the DM operation. After each image is acquired a real-time analysis is made to automatically adjust the exposure

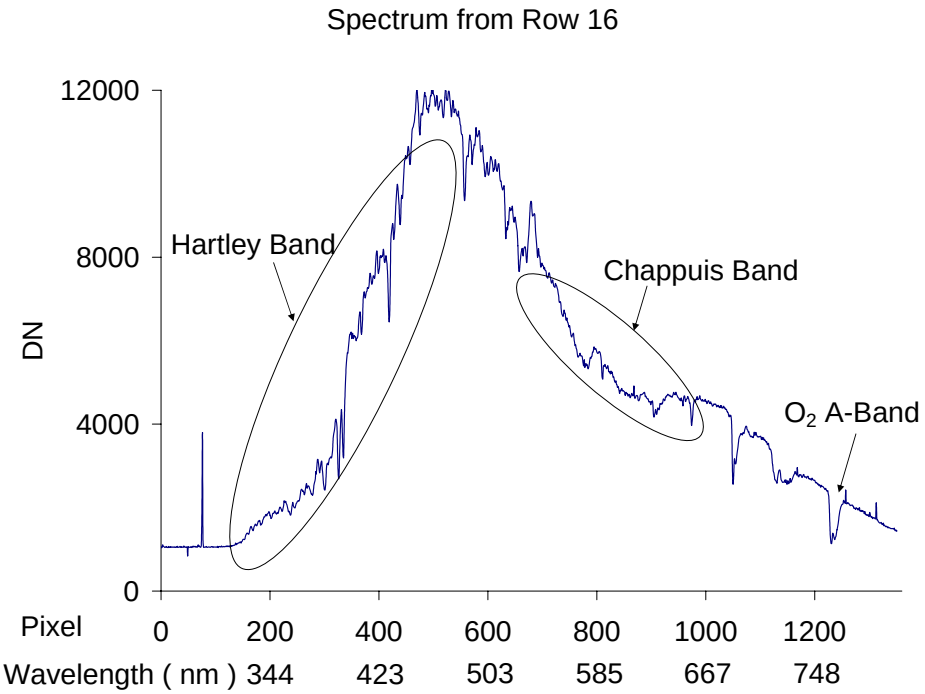

Figure 2.16: Spectrum obtained for row 16 on March 17th, 2006 at 7:36 AM.

time of the next image to provide maximum signal without over-exposing the CCD. At an SZA of approximately 83°, absorption in the Chappuis band is just detectable. Near 90° SZA, when the sun is just below the horizon, the signal intensity rapidly decreases to zero. Measurements were taken for each twilight period (morning and evening) between an SZA of 83° and 93° and the calibrated data set archived for each twilight period. The following sections describe the software designed to accomplish the task of data acquisition, analysis, and archiving. No minimum exposure time was specified, as the exposure times required for optimal data acquisition are not small enough to introduce significant timing errors. The maximum exposure time was set to be 10 s to prevent the automatic exposure calculation from setting abnormally large exposure times. Typical measurements for the data sets occur between 100 ms and 8 s with approximately 7 s between consecutive measurements. Each spectrum is approximately 354 kilo-bytes and each twilight data set contains approximately 300 measurements along with their dark current spectra and dark current calibrated spectra. This results in a twilight data set that uses approximately 300 mega-bytes

of space.

2.4.2 Control Software

Control of the DM is performed remotely through a server computer and a data acquisition program. The server computer is interfaced with the DM and commands the CCD exposure. The DM accepts the readout mode and exposure time and performs the required task for that exposure. The server computer is set up to passively await a connection and then respond to the received commands. A client program run on any computer connected to the internet will seek out and connect to the server. The client program has a graphical user interface (GUI), Figure 2.17. The box in the center of the GUI is used to plot the data from the CCD when a single image is taken. The user options for controlling the DM are described in Table 2.1 and entry fields for the DM are described in Table 2.2.

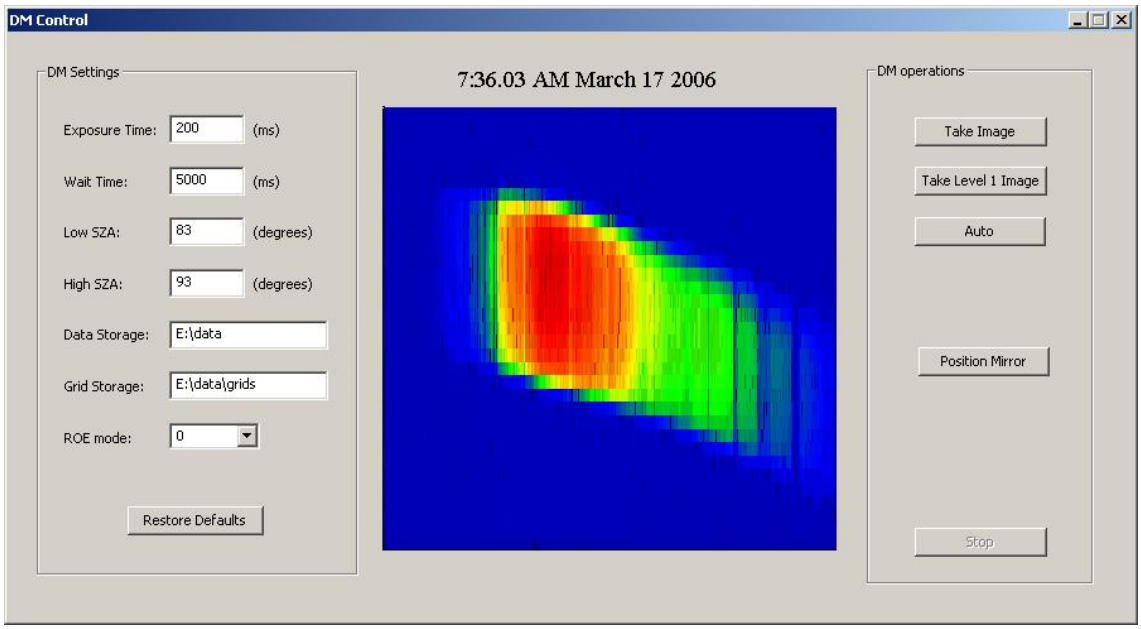

Figure 2.17: Graphical user interface for the Development Model.

Once the client program has connected to the server, it transmits the exposure information that is used to control the DM. The server program sends the DM the exposure parameters and receives the CCD image data. This information is returned to the client, which automatically names the exposure files and places them in di-

Table 2.1: GUI buttons used to control the DM data acquisition.

Button	Action
Take Image	Exposes DM for the amount of time specified in the Exposure Time box, at the mode specified in the ROE dropdown box, and stores the file in a directory specified by the Data Storage box. The image is then plotted in the empty box in the center of the program.
Take Level 1 Image	Follows the same instructions as the Take Image box then closes the shutter and repeats. The images are then subtracted to make a final image. The image is then plotted in the empty box in the center of the program.
Auto	Will take measurements based on the solar zenith angles specified in the Low SZA and High SZA boxes and then makes a plot of all the spectra over the range of SZA's. This plot is automatically labelled and placed in the grid storage directory specified.
Position Mirror	Acquires and plots images continuously so the mirror may be positioned for maximum light gathering.
Stop	Breaks out of the Automatic measurement loop
Restore Defaults	Restores the DM settings to their default values. These values are shown in Figure 2.17

rectories, before making a real-time dark current subtraction. When the connection is terminated the server program returns to its passive state. For the automatic exposure option, the programs are continuously connected and exposures for the defined range of solar zenith angles are taken. In the present work this is defined as a twilight measurement set as it is made during either a sunrise or sunset period. When the twilight measurement set is finished the client program automatically performs the calibrations on the data. All data are archived for subsequent further analysis.

Table 2.2: Entry field parameters for control software.

Entry Field	Property
Exposure Time	Defines the number of milliseconds for which a single exposure is to be taken. For the auto exposure setting it defines the exposure time of the first image.
Wait Time	Defines the amount of time to wait between successive measurements in the auto exposure mode.
Low SZA	Defines the lower solar zenith angle in the range for the auto exposure mode.
High SZA	Defines the higher solar zenith angle in the range for the auto exposure mode.
Data Storage	Defines the directory where collected data are to be stored.
Grid Storage	Defines the directory where the processed data in the GridStruct format are to be stored.
ROE Mode	Defines the ROE mode for the collection of data.

2.5 Conclusion

It has been shown in this chapter how the various components are combined to form the OSIRIS USASK Observatory. Scattered light passes through the light hatch and shutter system on top of the Physics Building and into the fiber optic cable. This radiation is transmitted through the fiber optic cable and collimated before it enters the DM. The light is imaged onto the CCD and read out using the control software of the server program. The raw data are archived for calibration and conversion to line of sight radiance measurements. The calibration procedure is described in the next chapter.

Chapter 3

Instrument Calibration

3.1 Introduction

The goal of the instrument calibration is to take the digital numbers, which are output from each pixel of the CCD, and convert them to line of sight radiances. A description of the processes used to remove instrument effects in the archived data are presented in this chapter. Figure 3.1 shows the processes and how they fit into the system. The first component, the DM, produces data that are archived as level zero data and then processed by the next three components of the system. After these three processes, the final data products are achieved and archived as level one data. The digital number output for each pixel includes a thermal signal that is removed through a dark current removal process to obtain a number proportional to the line of sight brightness. The next step is to determine the wavelength represented by each pixel; this requires a wavelength calibration. Even with a constant intensity signal at each wavelength, the digital number output will vary from pixel to pixel due to variations in the CCD quantum efficiency; these effects are removed through a relative calibration. The final characterization of the instrument is the determination of the point spread function. This function describes the brightness distribution of a simple monochromatic line on the CCD, i.e. the apparent wavelength spread of a monochromatic line. The point spread function is needed in the analysis of modelled data that are used to predict the image output from the DM.

The DM outputs 32 rows of data in ROE mode 0. In the present analysis the 16th row has been chosen because it is in the middle of the CCD and produces consistent

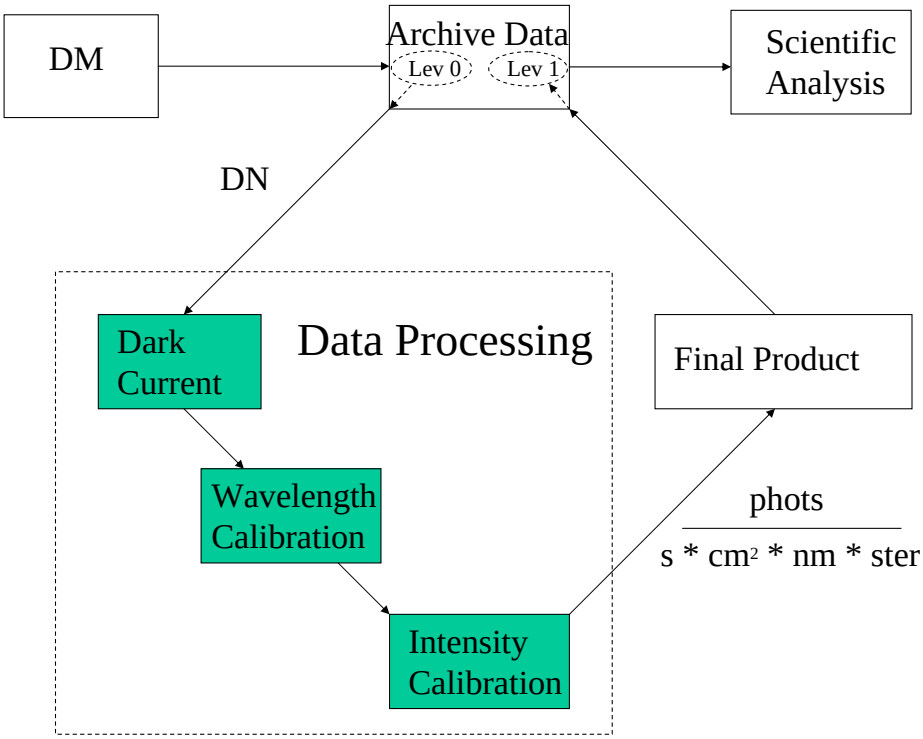

Figure 3.1: System block diagram.

data with a maximized signal. The goal of the instrument calibration is to take the digital number output for each pixel in this row and produce line of sight radiances in $\frac{phots}{s \cdot cm^2 \cdot nm \cdot ster}$. As there were no accurate absolute calibration sources available, only a relative calibration was produced along with a nominal absolute calibration using MODTRAN modelled data. The nominal absolute calibration is considered accurate to $\sim 50\%$ and was completed to give the measurements a greater physical meaning. For the analysis of data only a relative calibration is required as it is the ratios of intensities that are used. This is described in more detail in Chapters 4 and 5. Figure 3.2 shows the effect of the calibration procedure. The first graph is the original data from the DM and the second graph shows the same data after the calibration has been applied; the different units in the first and second graph should be noted.

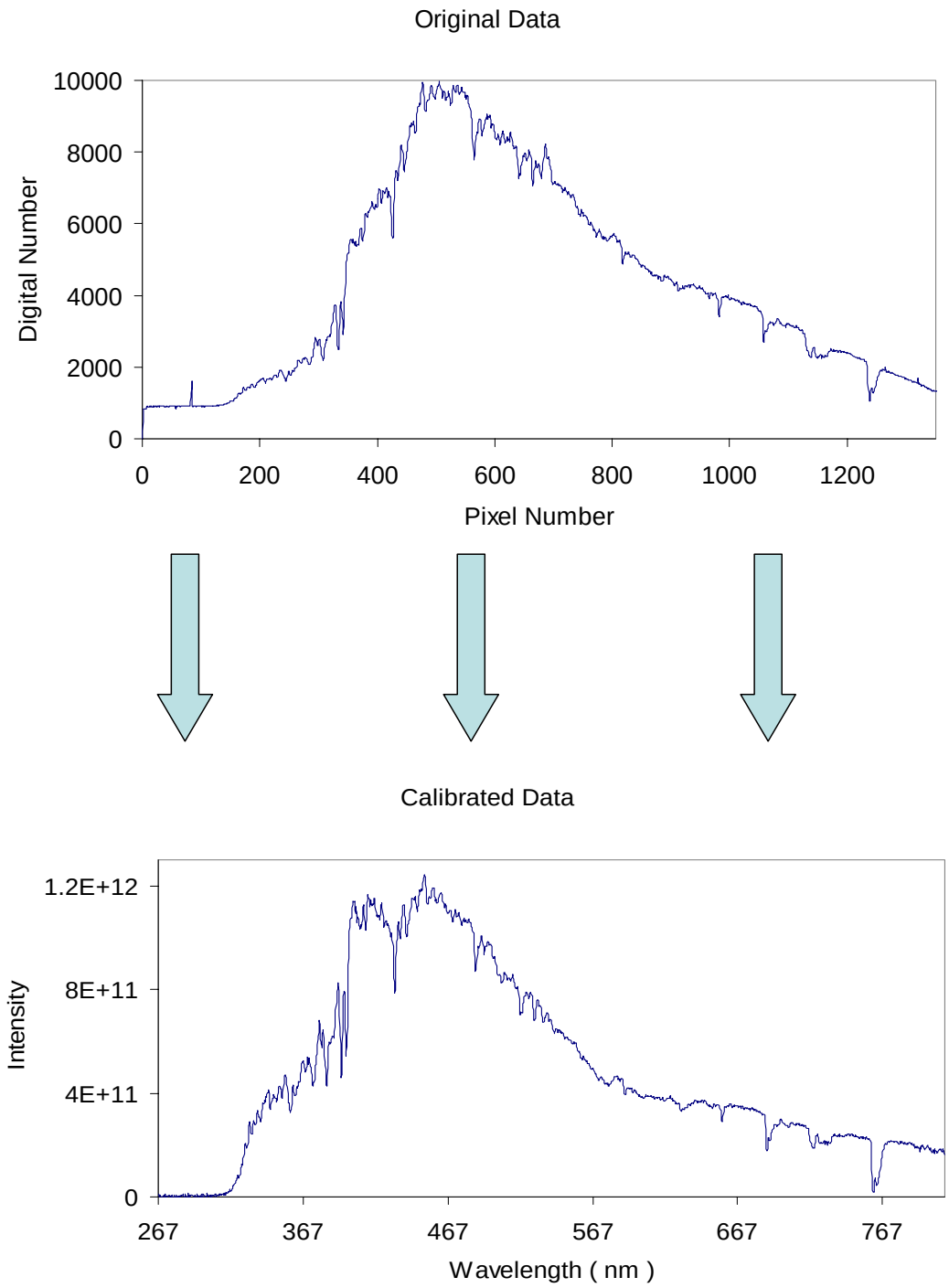

Figure 3.2: Purpose of the instrument calibration. The Intensity axis of the calibrated graph has units of $phots/s/cm^2/nm/ster$.

3.2 Dark Current, Stray Light, and DC Offset Removal

Dark current is a phenomenon that is present in all images taken with the DM. The DM is run at room temperature, which is considered hot for most CCD applications, and so generates a significant dark current signal that must be removed to obtain accurate measurements. The system is not cooled as the calibration method is reliable and introduces little error. Figure 3.3 shows an example of this random thermal signal for row 16 of the CCD, the row used for data collection. The signal starts off in the DC offset portion of the CCD at approximately 820 DN and then fluctuates randomly about approximately 855 DN counts for the UV portion of the spectrum and increases to fluctuate around 858 DN counts at longer wavelengths. This slope is due to the finite time taken to read out the image information. A row is read out one pixel at a time, shifting the remaining pixels during the readout. While the pixels are no longer in the illuminated portion of the CCD they continue to accumulate dark current. Thus by the time the last pixel in the row is read out there has been an increase in the registered dark current. The readout of a single row takes approximately 41 ms. This is seen in the slight slope to the dark current data.

The dark current was previously characterized by *Wilcox* [2002] who made a database of expected dark current, at given temperatures, for each pixel. In the present work it was initially proposed to use a thermistor in the DM to monitor the CCD temperature and query the database to determine the dark current. Unfortunately, this characterization was unreliable as the thermistor used for temperature measurement could not be located on the CCD, so the temperature measurement was unreliable. Thus, in order to remove dark current, the shutter system described in Section 2.2.2 was designed and implemented.

Immediately after each illuminated image is acquired, the shutter is closed and a dark current image is taken for the same exposure time. All skylight is blocked by the shutter but any other unwanted light present in the illuminated image is also present in the dark current image. A pixel by pixel subtraction of the illuminated image and the dark image is made; this procedure yields the signal from the incident light and removes any thermally generated signal as shown in Figure 3.4. As the

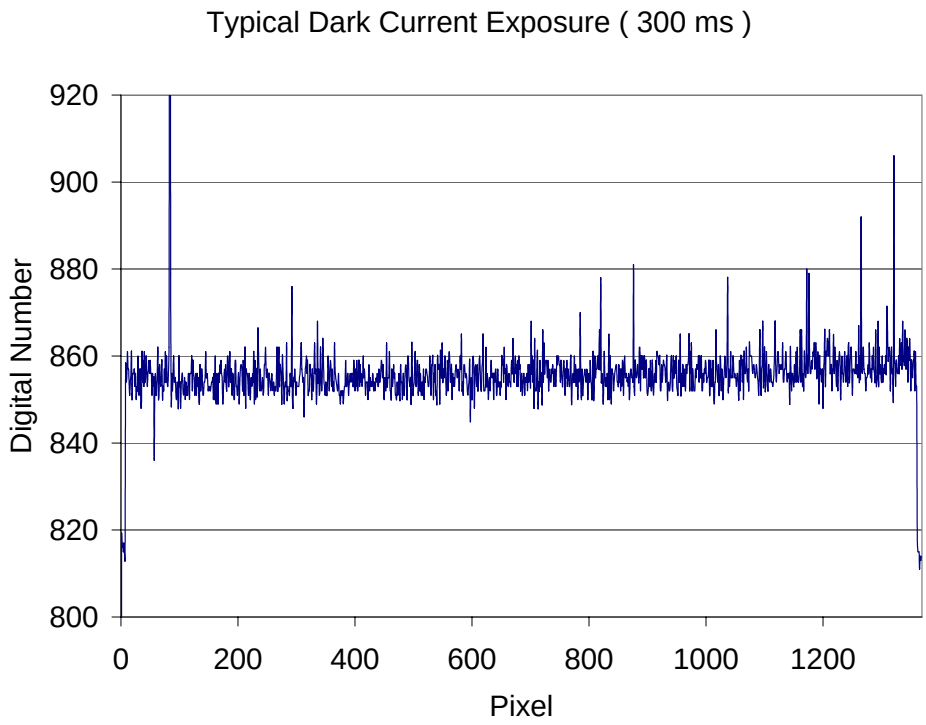

Figure 3.3: Typical dark current exposure for June 22, 2005 at 7:30 PM.

dark current measurement is made immediately after the data measurement (within 1 second) the temperature of the detector does not have time to change significantly. This results in an accurate dark current removal.

To estimate the error associated with the dark current removal one thousand pairs of background images were taken. The shutter was always closed so that the CCD was never illuminated. One of the measurement pairs was subtracted from the other and all data for a single pixel were binned according to the digital number difference. The ideal number is zero, which corresponds to both images being identical. However, a distribution about zero is expected with a standard deviation that corresponds to the error associated with dark current removal. Two pixels were chosen at random to demonstrate that the dark current statistics are similar for all pixels. The selected pixels were pixel 425 at 433.1 nm and pixel 652 at 524.4 nm. Figures 3.5 and 3.6 show the histograms for pixels 425 and 652 respectively. Analysis of these data revealed a standard deviation of 5.19 DN for pixel 425 and 4.97 DN for pixel 652. The standard deviation, σ, was calculated

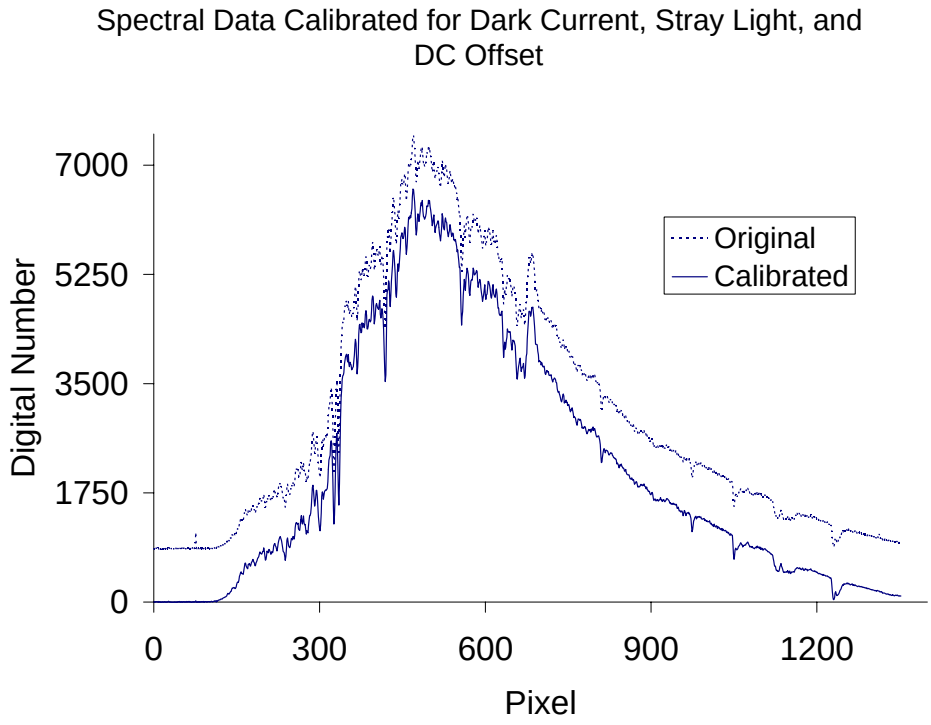

Figure 3.4: Dark current, stray light, and DC offset calibrated image for June 22, 2005 at 7:30 PM.

according to

$$\sigma = \sqrt{\frac{\sum (x - \overline{x})^2}{n - 1}}, \tag{3.1}$$

where x is digital number difference for a pair of images, $\overline{x}$ is the average digital number difference, and n is the total number of data points.

Figure 3.7 shows residuals for the entire CCD and has an associated standard deviation of 5.03. With the greater sampling size this histogram more closely resembles a Gaussian distribution than the single pixel histograms. The distribution appears symmetric about the zero difference point, and extends to $+/-20$ DN for the residuals.

As noted above, the dark current residual histograms all have standard deviations of approximately 5 digital number counts. This results in an error of $+/-5$ DN associated with any dark current removal. An illuminated image typically produces between 10,000 and 16,000 DN and the associated dark current image typically

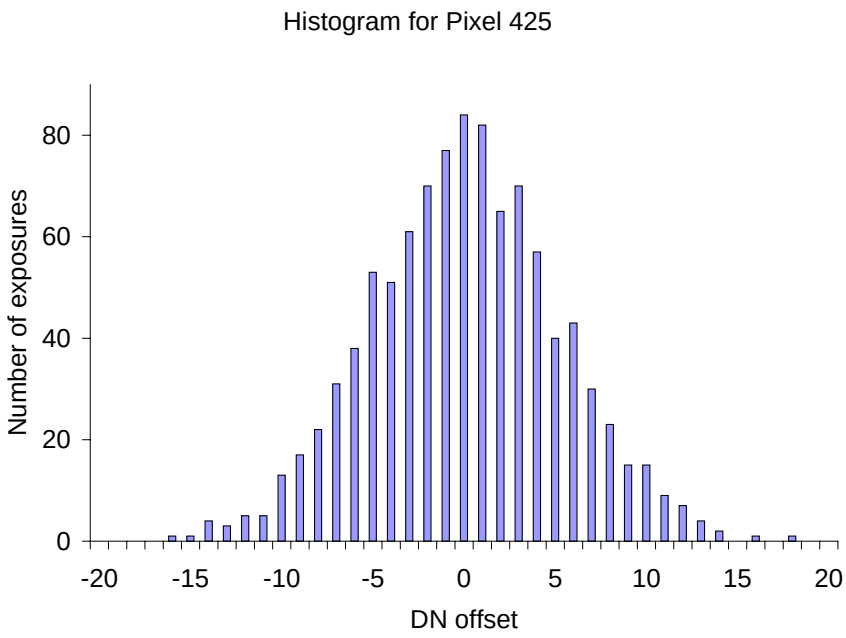

Figure 3.5: Dark current residuals for pixel 425.

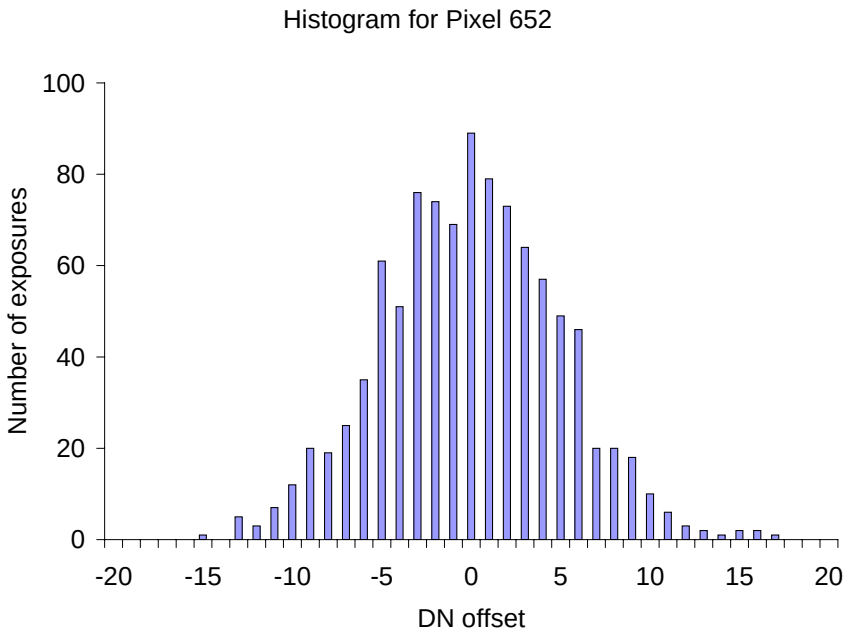

Figure 3.6: Dark current residuals for pixel 652.

produces between 800 and 900 DN. Any given final image should have at the least $10,000 - 1,000 = 9,000$ DN counts. Thus the error of 5 DN results in a maximum dark current calibration error of less than .06%. This error is considered insignificant, thus the dark current removal technique is accurate and any error in the dark current adds little uncertainty to the measurements. This is a significant advance beyond the work of *Wilcox* [2002].

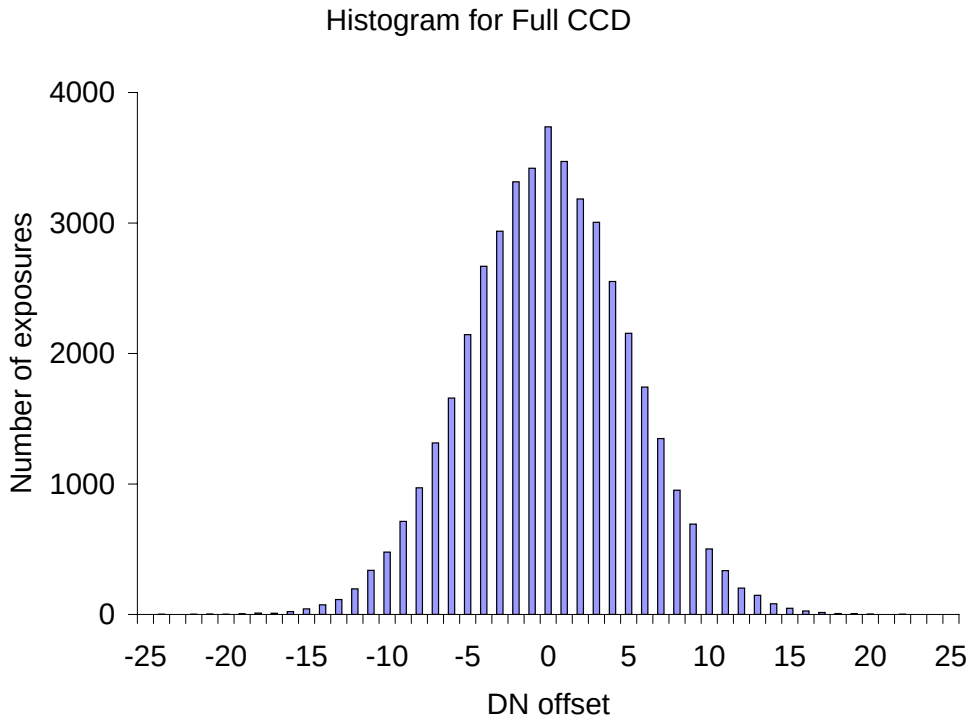

Figure 3.7: Dark current residuals for full CCD.

3.3 Wavelength Calibration

The optical chain in the DM includes a diffraction grating that spectrally sorts the wavelength components of the incident light. These wavelengths are spread across the CCD and, in order to determine the wavelength at the center of each pixel, a wavelength calibration must be completed. Mapping each pixel center to a specific wavelength allows conversion between pixel number and wavelength.

3.3.1 Gas Lamp Measurements

Several different gas discharge lamps were used in the wavelength calibration to determine the pixel to wavelength relationship of the DM. The light from various lamps was fed into the fiber optic cable and through the DM. The spectra from each of these lamps had prominent spectral features easily identified on the CCD. As each spectral line has a different intensity, the exposure time was changed in order to keep the peak values close to the CCD saturation point. This gave a good signal to noise ratio for each spectral feature. The gas lamp data are shown in Figure 3.8 with emphasis on the helium and neon spectral lines. The wavelength of the spectral lines used for calibration purposes are indicated on the figure.

By closely examining the images taken of these gas lamps, lines were chosen that were easily identifiable, symmetrical, and not too near other spectral features. The wavelengths of the selected spectral lines were determined from the CRC Handbook of Chemistry and Physics [*CRC*, 1974]. Any peaks that were skewed, or had another peak too close to it to be resolved, would result in a shift in the measured pixel number. Thus the rejection of these peaks ensured that the correct determination of the pixel number for the center of the spectral line.

The data points were used in a weighted average method to determine the correct pixel number for the given wavelength. The weighted average is calculated by

$$\bar{i} = \frac{\sum_i (i + .5) * D_i}{\sum_i D_i}, \tag{3.2}$$

where $\bar{i}$ is the weighted average pixel number, i is the pixel number and D_i is the digital number output at that pixel. As a single pixel measures the intensity incident on the entire pixel, it is assumed that the reported digital number corresponds to the midpoint of the pixel, $(i + .5)$. Figure 3.9 shows a peak from the helium spectrum used in the wavelength calibration. Each point is plotted and the calculated average pixel number of 459.5377 is shown as the vertical line in the center of the plot. As the data was fit using a weighted average, error in the calibration stems mainly from the asymmetry of the distribution of data points. This asymmetry is caused by coma from optical components and nearby spectral lines. The limits were chosen on either side of the spectral feature of interest so that the distribution appeared

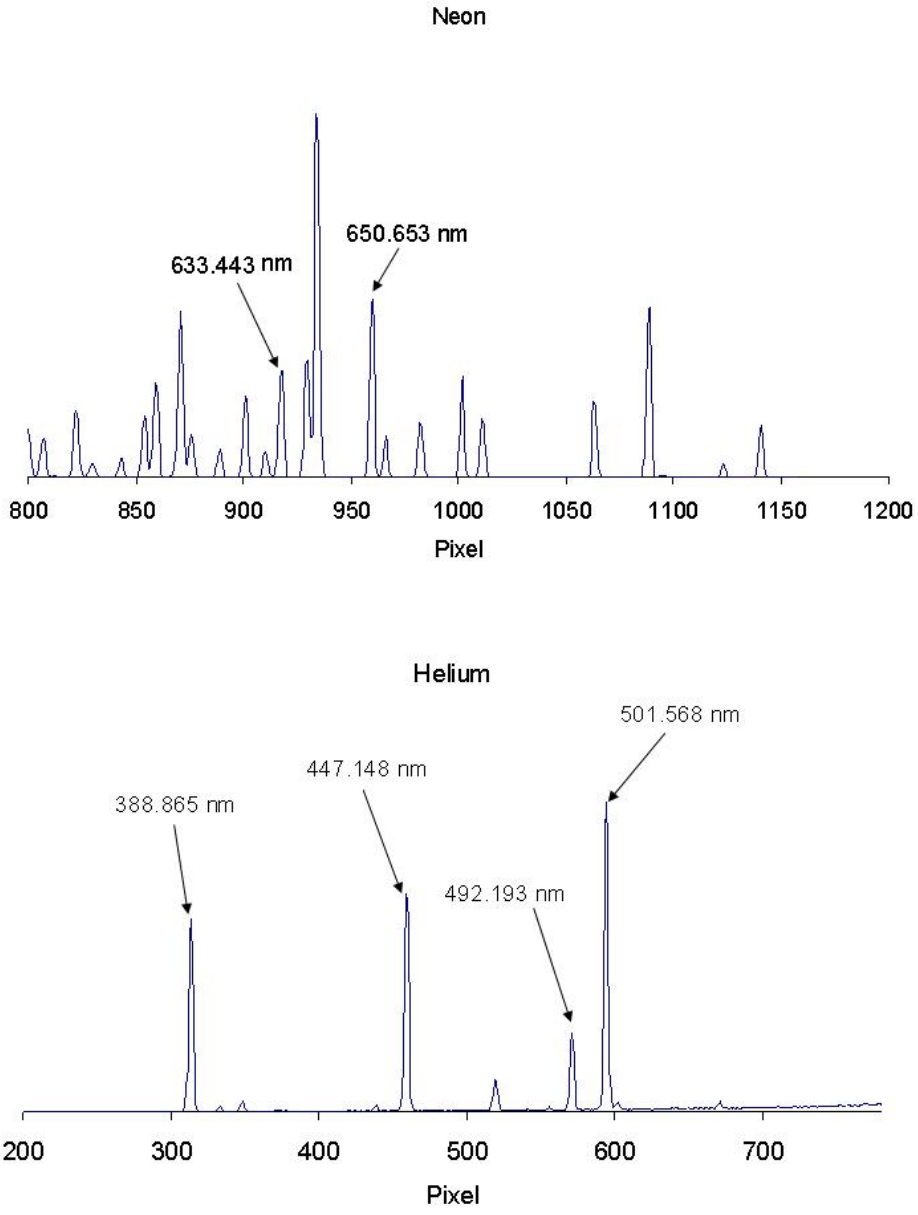

Figure 3.8: Gas lamp data with emphasis on the spectral lines used for the wavelength calibration.

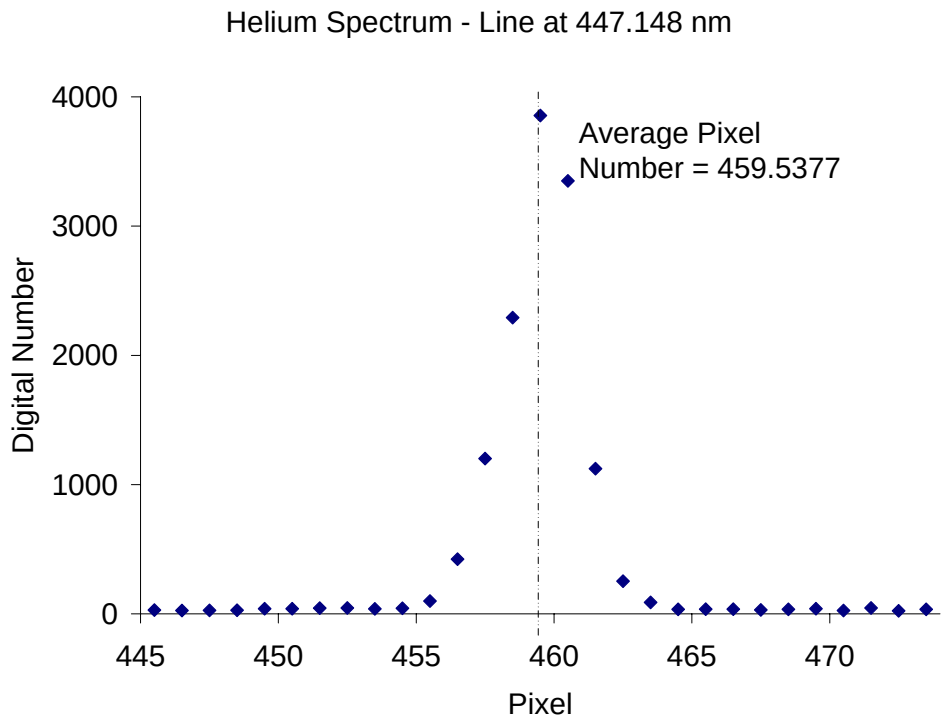

Figure 3.9: Sample gas lamp peak for hydrogen.

symmetric. Visual inspection of curves like the one in Figure 3.9 indicate this error is small.

3.3.2 Results

The wavelength calibration was completed for the CCD in two parts, where the two regions correspond to each side of an order sorter. The order sorter consists of two glass sections with the section covering the shorter wavelength region of the CCD having no filtering properties. The glass covering the long wavelength region of the CCD eliminates shorter wavelengths that are imaged in second order at the same angle or position as the longer wavelengths, ie. 300 nm goes to 600 nm. In the region where these two filters abut there is some anomalous behavior so that data in that area are unreliable. The join is at pixel 591, near 500 nm, so that two separate calibrations were made for the CCD; the first from pixel 0 to 591 and the second from pixel 591 to 1353. Polynomials were fitted on both sides of the CCD and combined

for a split polynomial fit calibration. This calibration is discontinuous at the order sorter (500 nm) so any data obtained within +/- 10 nm are not reliable and has been ignored. A mean pixel number was calculated for each spectral line with the weighted average method. These pixel numbers correspond to the wavelengths of the spectral features and are used to determine the best fit polynomial that relates a pixel to the wavelength. Second order least squared curves were fit to the data points to determine the second order polynomials for each half of the CCD. These coefficients are listed in Table 3.1.

Table 3.1: Pixel to wavelength calibration polynomials.

Pixel Range	Constant	Linear Term	Squared Term
0 - 591	266.84	.38175	2.2286E-05
591 - 1352	255.04	.41562	-3.8069E-06

The two part pixel to wavelength calibration is shown in Figure 3.10, which appears to be linear. The collected data points are indistinguishable from the polynomial fit when plotted so a plot of its variation from the linear terms is shown in Figure 3.11. Only the squared terms have been plotted to emphasize the difference between the polynomial fit and its linear component. It is apparent that there are two different polynomials for either side of the CCD, which validates the need for the split polynomial fit. A 2nd order polynomial was also fit for the entire range in order to compare with the split polynomial calibration. In order to estimate the accuracy of the polynomial fits a plot of the residuals is shown in Figure 3.12. The residual is calculated for each polynomial fit at each spectral position by subtracting the actual wavelength of the gas lamp spectrum from the wavelength given by the polynomial fit. It is readily apparent that the method of split polynomial fitting for the two sides of the order sorter gives a more accurate wavelength conversion.

3.3.3 Verification of Wavelength Calibration

Fraunhofer lines are absorption lines in the solar spectrum and were first characterized by Joseph Fraunhofer in 1814. These absorption features can be seen in the sky data collected by the DM and shown in Figure 3.13. Since these features have known wavelengths, a plot of the collected solar spectra against the calibrated wave-

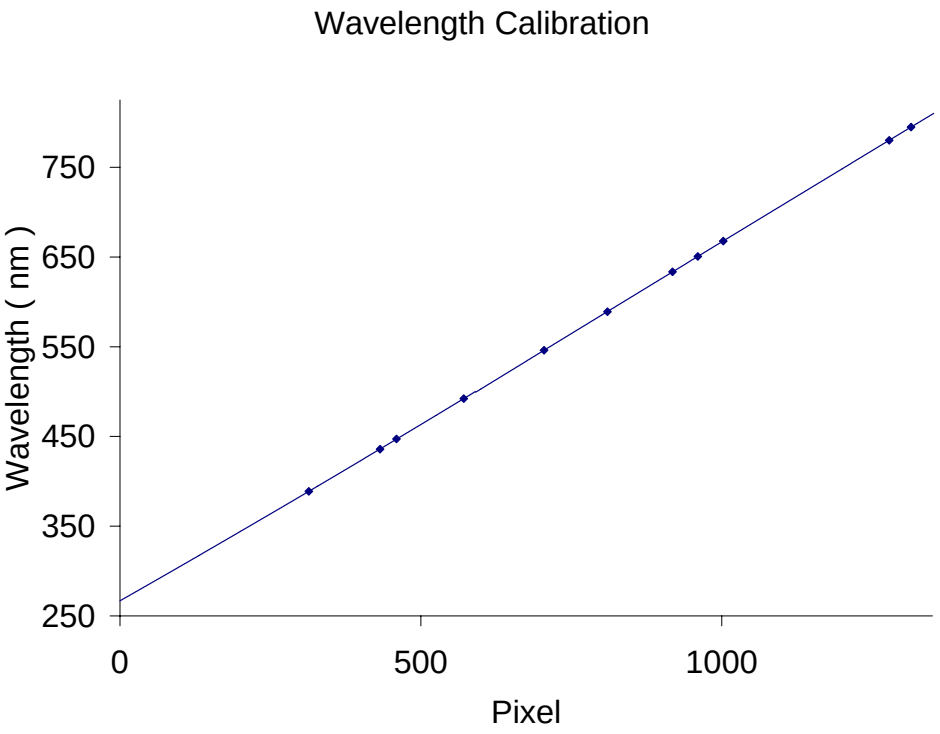

Figure 3.10: Wavelength calibration showing near linear relationship.

length will reveal any differences between the two. Figure 3.13 shows a measurement taken by the DM with all of the known Fraunhofer structures indicated. Using the second order polynomials, the pixel to wavelength ratio is mapped onto the x-axis and the measured wavelengths for the Fraunhofer lines determined. The measured wavelength of the Fraunhofer structure is determined locating the minima in the spectrum. The difference between calibration wavelength and the actual Fraunhofer value is the error in the wavelength calibration as shown in Figure 3.14. The difference from pixel to pixel is approximately 0.43 nm and Figure 3.14 shows all of the residuals within 0.4 nm. This error may be associated with the identification of the minima and so the DM wavelength calibration is probably better than this number.

3.4 Characterization of Point Spread Function

A point spread characterization is needed in order determine the range of wavelengths received by each pixel. A monochromatic spectral line entering the DM is

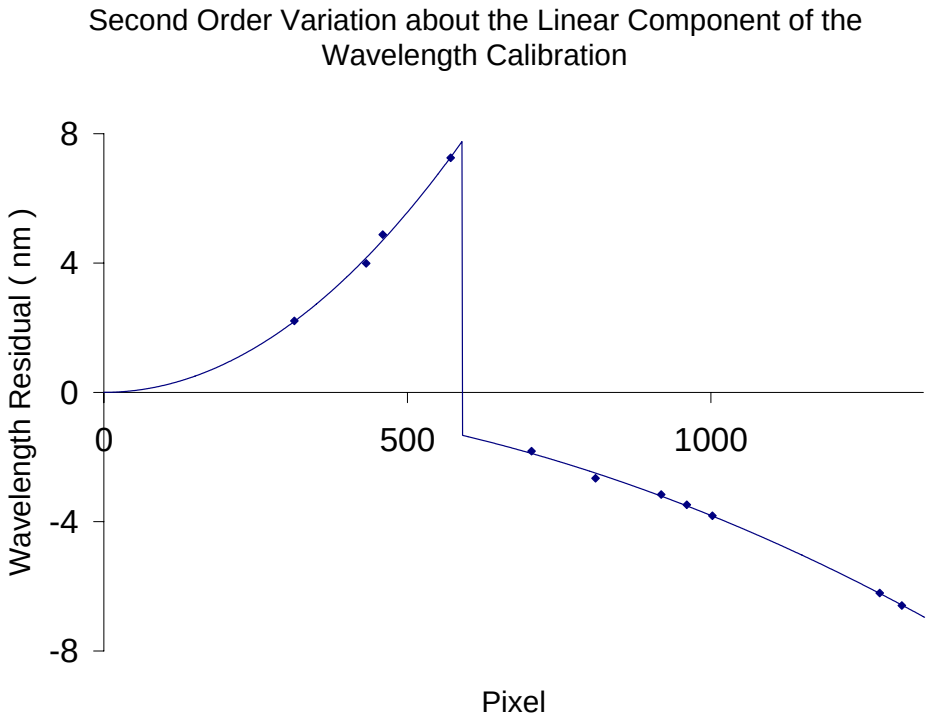

Figure 3.11: Deviation from the linear component of the second order polynomial fits.

not focused to a point on the CCD due to imperfect optics, a finite field of view, and a finite width of the lines on the grating. The optics and field of view result in a blurring in the spatial direction on the CCD, which is in the vertical, and therefore is not the major contributor as only one row is being used in the data analysis. However, the fringe pattern produced by a diffraction grating has a finite width and shape that causes a blurring in the wavelength direction. This is the spectral point spread function and defines the resolving power of the DM. For this reason a point spread calibration is needed to characterize the range of wavelengths received by each pixel.

3.4.1 Analysis

A monochromatic source of radiation entering the DM illuminates a rectangle on the CCD due to the finite width of the entrance slit. This rectangle is the image of the slit on the CCD. This imaging contributes to the broadening of the observed

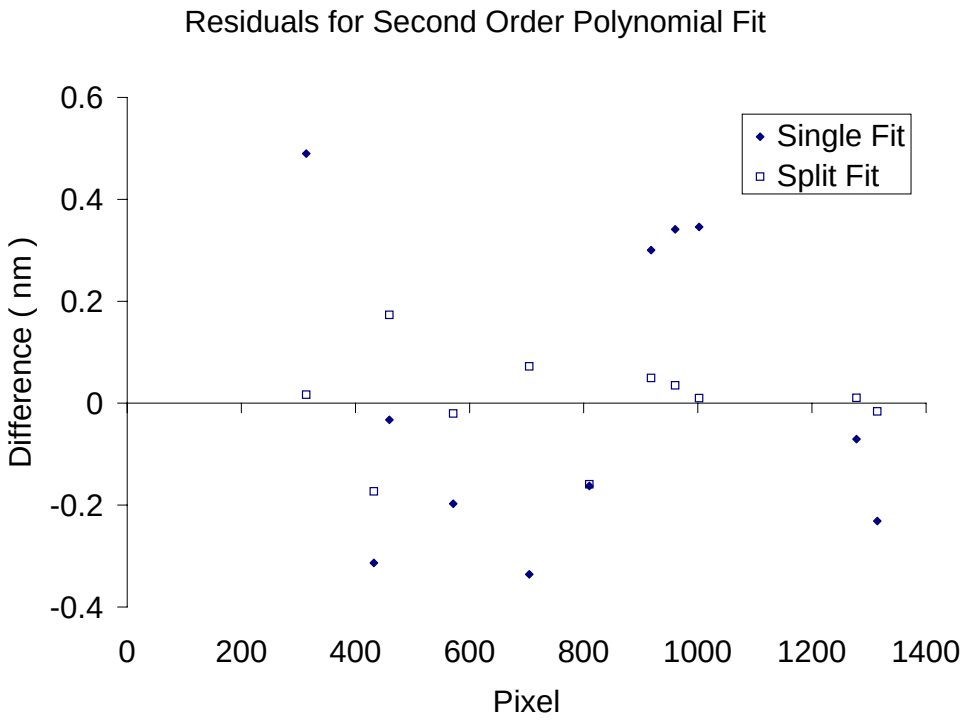

Figure 3.12: Residuals showing the difference between each polynomial fit and the actual data point.

spectral features and so identifies the need for a determination of the point spread function. In order to measure the point spread function, the same gas lamp data that provided the wavelength calibration were used. The width of the measured spectral line was calculated using

$$\sigma = \sqrt{\frac{\sum_i [((i+.5)-\bar{i})^2] * DN_i}{\frac{(n-1)*\sum_i DN_i}{n}}}, \tag{3.3}$$

where σ is the standard deviation, i is the pixel number, $\bar{i}$ is the average pixel number (shown in Figure 3.9), DN_i is the digital number output at pixel i, and n is the number of data points used. As with the calculation of the average pixel number in the wavelength calibration, $i+.5$ was used in order to place the pixel data at the center of the pixel.

If it is assumed that the point spread function is a Gaussian then the relative

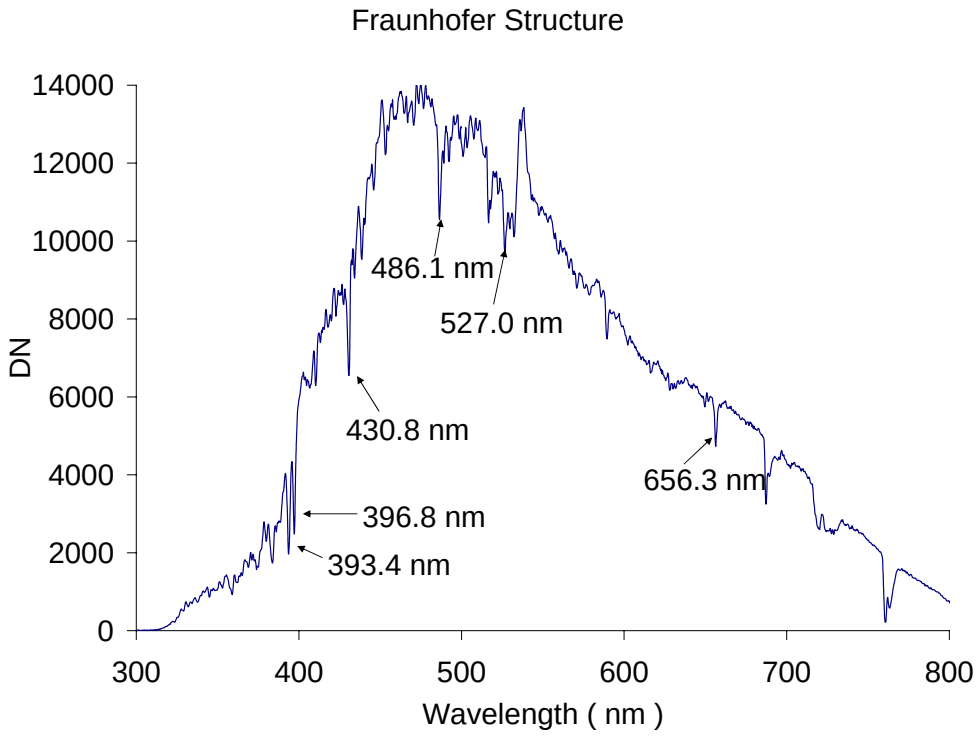

Figure 3.13: DM measurement showing Fraunhofer lines.

irradiance on each pixel is given by

$$f(i) = \frac{1}{\sigma\sqrt{2\pi}} \exp\left[\frac{-(i-\bar{i})^2}{2\sigma^2}\right], \tag{3.4}$$

where $f(i)$ is the Gaussian contribution from the average pixel, $\bar{i}$, at any other pixel, i. The point spread function varies slightly across the measured spectrum so the standard deviation, σ, was determined for all pixels. A linear interpolation was made between all experimentally determined points to obtain the σ vs. pixel relationship (see Table 3.2) and plotted in Figure 3.15.

These sigma values are used in an iterative computer program to calculate the contribution of all wavelengths at each pixel. This yields a database product for the instrument characterization. This allows for the prediction of the spectrum that the DM will return for a given input. Figure 3.16 shows the contributions from each wavelength to pixel 850. The intensity at each wavelength is multiplied by the contribution factor assigned to it and summed to get a total intensity for pixel 850.

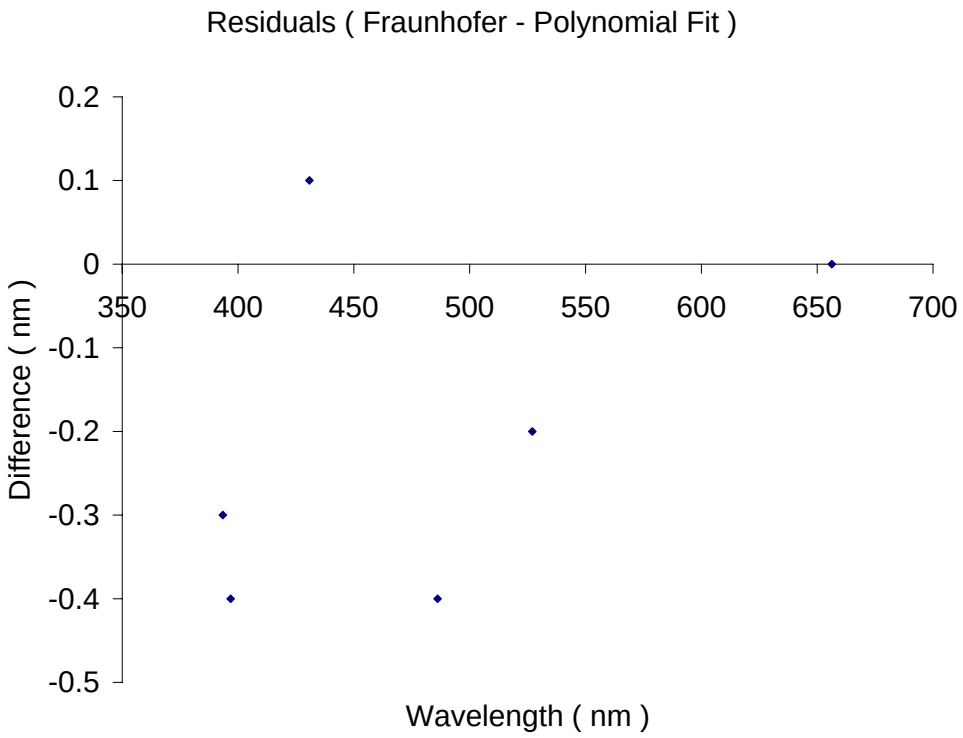

Figure 3.14: Fraunhofer residuals showing the difference between the Fraunhofer wavelengths and the calibrated wavelengths.

Table 3.2: Point spread function for the entire CCD.

Pixel Range	Equation
0 - 433	$\sigma = -0.0003115820 * i + 1.970908638$
433 - 460	$\sigma = -0.0051452780 * i + 4.060185197$
460 - 595	$\sigma = -0.0000255136 * i + 1.707460450$
595 - 705	$\sigma = -0.0018489160 * i + 2.791089378$
705 - 810	$\sigma = -0.0011993580 * i + 2.333401361$
810 - 919	$\sigma = -0.0021427830 * i + 3.097482900$
919 - 961	$\sigma = -0.0021364090 * i + 3.091631225$
961 - 1279	$\sigma = -0.0000604929 * i + 1.098287700$
1279 - 1361	$\sigma = \quad 0.0017037690 * i - 1.156578077$

The contributions from wavelengths away from the central one associated with the pixel quickly drop away to near zero values and this shape is typical of all the pixels on the CCD.

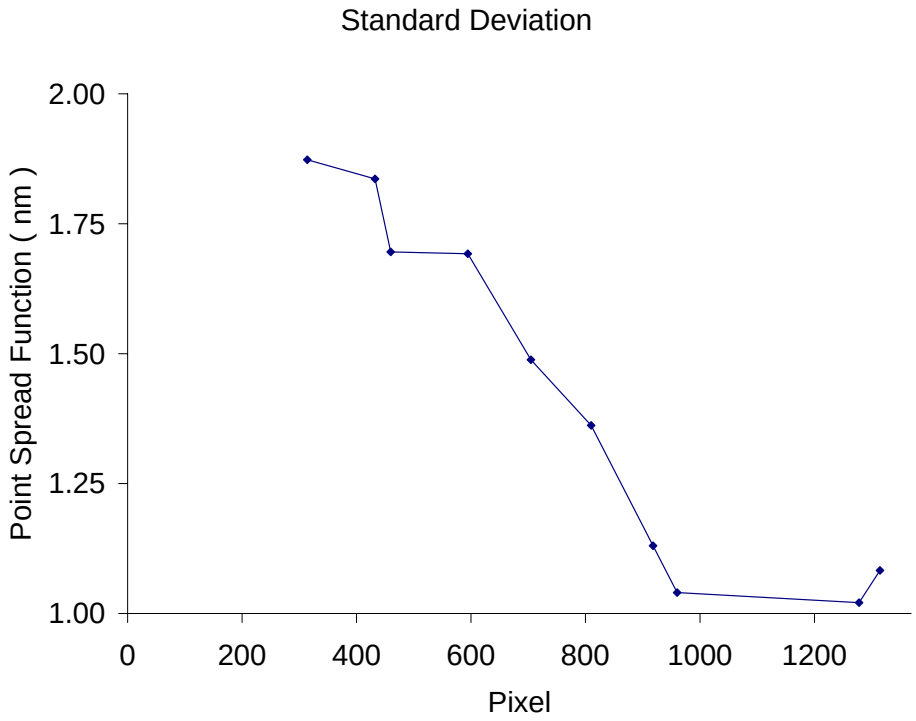

Figure 3.15: Standard deviation of the point spread function derived from the gas discharge lamps.

3.5 Relative Intensity Calibration

A relative intensity calibration was achieved by illuminating the DM with an Ocean Optics tungsten filament operating at approximately 3100 K. The procedure involved removing the end of the fiber optic cable from the shutter hatch and placing it in front of the tungsten source. The dark current determination was made with the tungsten source turned off and moved away from the cable end so that no radiation was present in the background measurement. This setup closely mimics the atmospheric measurements so the calibration is expected to be accurate. The emitted spectrum of the Ocean Optics source is defined by the Planck blackbody equation,

$$B = \frac{2\pi hc^2\epsilon}{\lambda^5(e^{\frac{hc}{\lambda kT}} - 1)}\left[\frac{W}{m^2 \cdot ster \cdot nm}\right], \tag{3.5}$$

where B is the intensity of the source, h is Planck's constant, c is the speed of light, ϵ is the emissivity of tungsten, λ is the wavelength, k is Boltzmann's constant, and

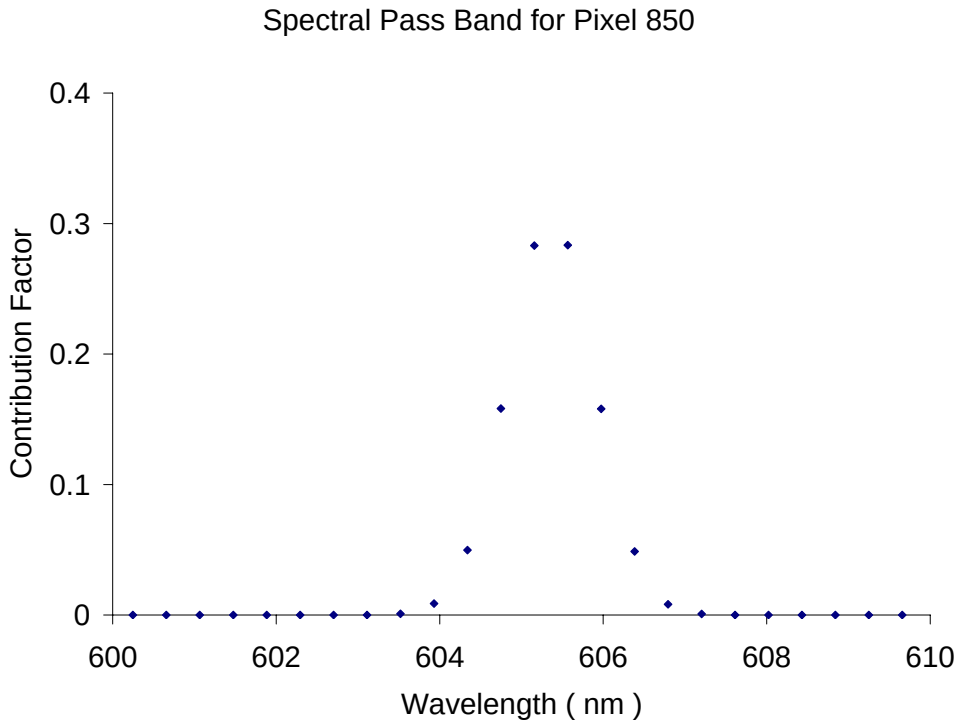

Figure 3.16: Contributions from all wavelengths to signal seen on pixel 850.

T is the temperature in Kelvin. B in Equation 3.5 is reported in $\frac{Watts}{m^2 \cdot ster \cdot nm}$ and can be readily converted to $\frac{phots}{s \cdot cm^2 \cdot nm \cdot ster}$ by division with the photon energy,

$$E = \frac{hc}{\lambda}[J], \tag{3.6}$$

which yields the final intensity,

$$B' = \frac{2\pi c\epsilon}{\lambda^4(e^{\frac{hc}{\lambda kT}} - 1)}\left[\frac{phots}{s \cdot cm^2 \cdot nm \cdot ster}\right]. \tag{3.7}$$

The absolute magnitude of the curve is not important, rather it is the shape of the curve that is of interest for the relative calibration. The modelled blackbody intensity must be corrected for the emissivity of tungsten. The emissivity of tungsten [*CRC*, 1974] is shown for various wavelengths and temperatures in Figure 3.17. There is no emissivity tabulated for 3100 K, but since there is little variation between shapes of the different temperature emissivity curves, at least beyond 400 nm, the

values of emissivity for 2800 K can be used with little error.

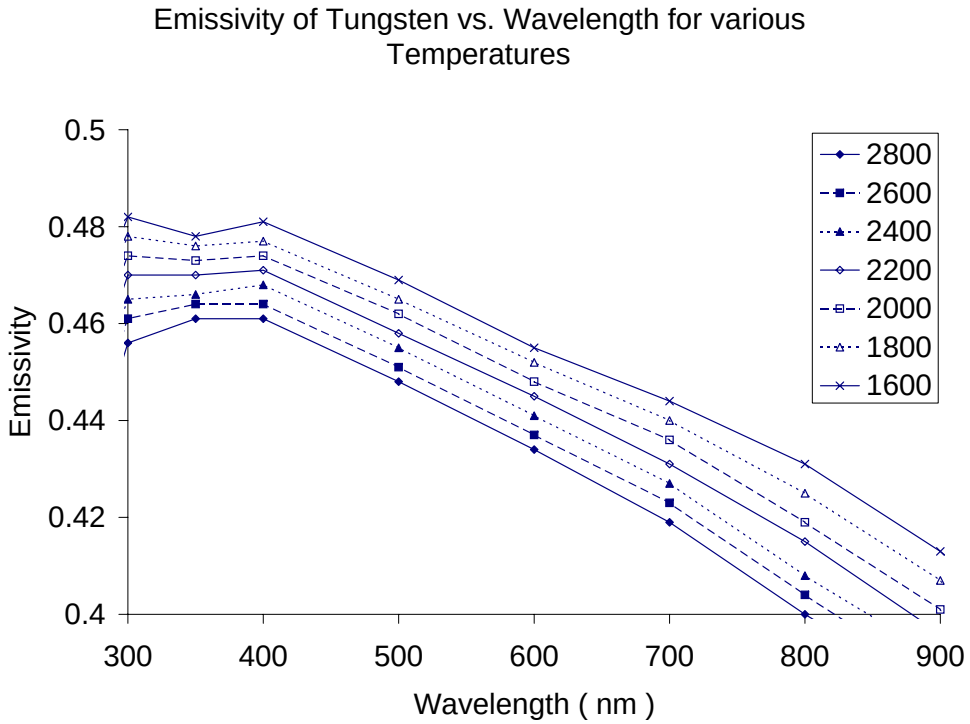

Figure 3.17: Plot of the emissivity of tungsten as a function of wavelength at different temperatures.

The input signal for the calibration is the blackbody curve at 3100 K multiplied by the emissivity of tungsten at each wavelength. This modelled input signal is shown in Figure 3.18 (a) and the measured signal is shown in Figure 3.18 (b). The structure in the measured curve near 510 nm is from the order sorter join while the other structure is from transmission features associated with the grating.

The quantum efficiency and the grating efficiency of the CCD detector decrease at wavelengths below 450 nm and beyond 700 nm. This results in the measured shape of the blackbody spectrum as seen in Figure 3.18 (b). The calibration curve shown in Figure 3.19 is the result of a pixel by pixel division in which the tungsten source spectrum has been divided by the measured spectrum, i.e. $\frac{Actual}{Measured}$, and then normalized. This curve can be used to remove the instrument effects from measured spectra. The calibration curve is more accurate in the higher wavelength portion of the CCD as there is greater signal available. There is also error associated with the

(a)

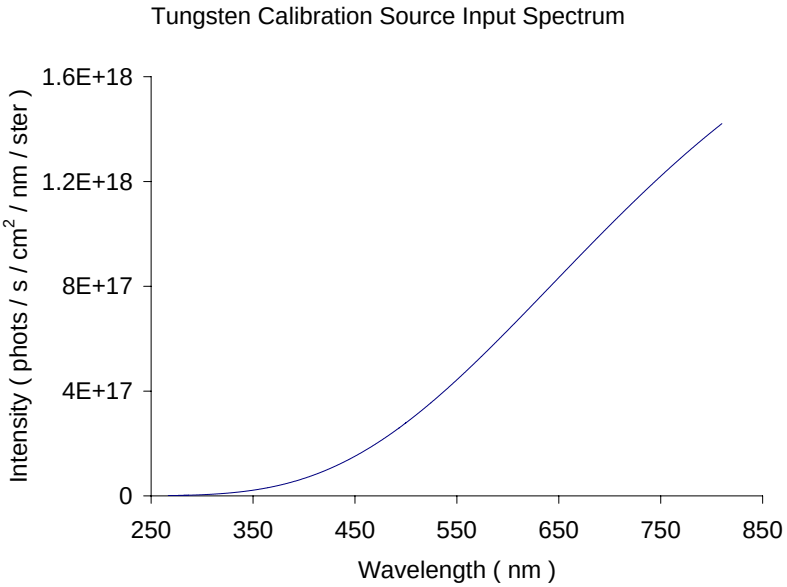

(b)

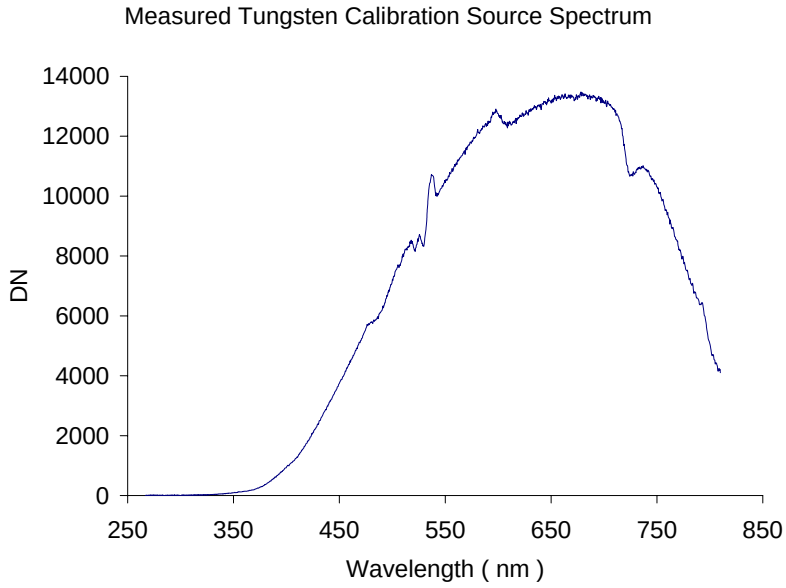

Figure 3.18: Tungsten source input spectrum at 3100 K, (a), and the measured tungsten spectrum, (b).

tungsten source as the temperature is known to be near, but not exactly, 3100 K.

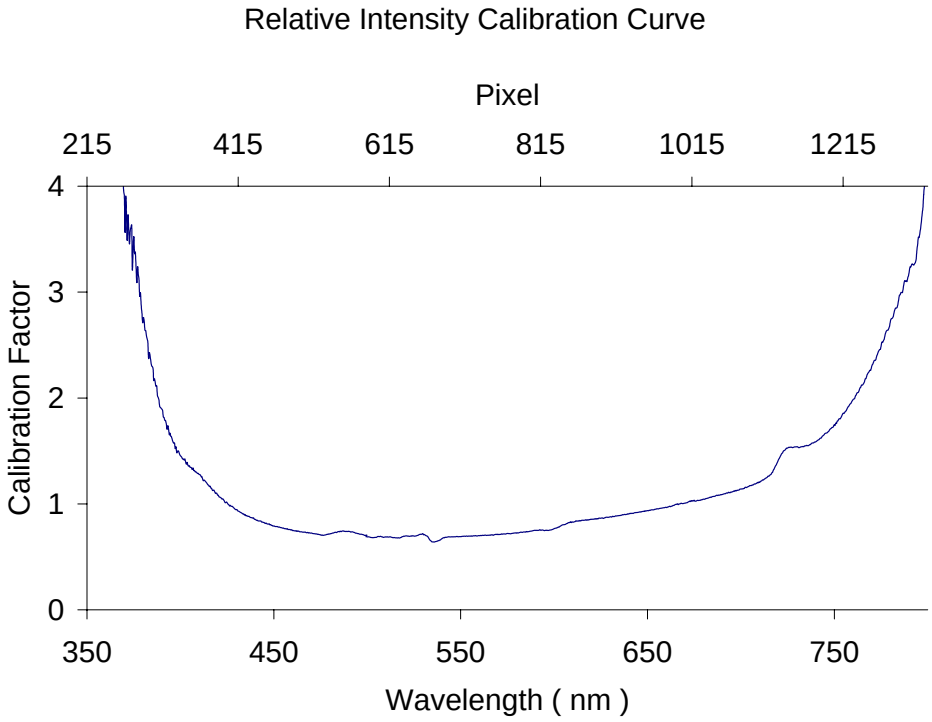

Figure 3.19: Calibration curve for tungsten source.

Figure 3.20 shows both the corrected and uncorrected sky spectra measured with the DM. The uncalibrated image is in units of digital number counts while the calibrated image is in units of $\frac{phots}{s \cdot cm^2 \cdot nm \cdot ster}$. The intensity has been converted from relative to absolute units using the nominal absolute calibration provided in the following section.

3.6 Nominal Absolute Calibration Using MODTRAN

MODTRAN (MODerate spectral resolution atmospheric TRANsmittance algorithm and computer model) is used to calculate atmospheric transmittance and radiance over a range of wavelengths at moderate resolution. The code was developed by the Air Force Research Lab and is available for personal use [*Berk et al.*, 1999]. A

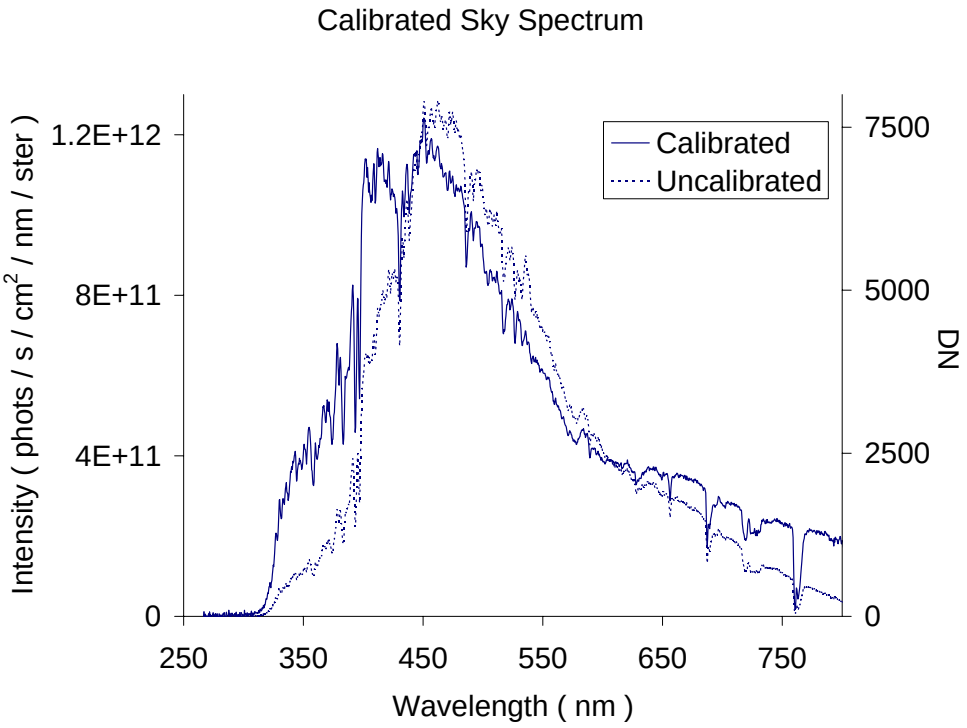

Figure 3.20: Calibrated spectrum for a sky image taken on the morning of September 21, 2005.

MODTRAN simulation was run for June 11, 2005 in the morning twilight using the date and Saskatoon co-ordinates as the input. This simulation was done to model the zenith brightness of the solar spectrum as seen by the DM at ground level. The simulated spectrum may be compared to a calibrated DM spectrum in order to determine a nominal absolute calibration, as the two should qualitatively agree. The date and location are needed as inputs because MODTRAN accesses temperature, pressure, and ozone profiles as part of its radiative transfer algorithm. Light incident upon the atmosphere is scattered towards the DM where it is then measured. The nominal absolute calibration completed is not wavelength dependent and yields one number that is used to scale the measured data.

3.6.1 Comparison with Modelled Data

Once the calibrations are applied to the data, a comparison with modelled data is required to determine how well the measured data fit with the accepted values.

A clear sky period where the sun was high in the sky was used to compare with MODTRAN modelled data. The day chosen was June 11, 2005 and the measured spectrum was obtained at 9:49 AM local time with the sun at a solar zenith angle of 47°. These values were used in the single scatter model of MODTRAN assuming no aerosols were present. The lower SZA was chosen for the input as MODTRAN becomes inaccurate for the longer path lengths through the atmosphere that are typical of high SZA measurements. Figure 3.21 shows the comparison between the spectrum obtained on the morning of June 11 with the complementary spectrum modelled by MODTRAN. The measured spectrum has been completely calibrated and all known instrument effects have been accounted for. The comparison shows that the measured data agree qualitatively with the modelled data. There is good agreement in the Chappuis band and a slightly higher peak in the measured data that may be due to aerosols in the atmosphere. The two graphs differ slightly near 300 nm, which may be due to the inaccuracy of the relative calibration at the lowest wavelengths registered by the CCD. This comparison also yields a nominal absolute intensity calibration. This is done only to assign a physical meaning to the product of the relative calibration provided and is only considered a nominal absolute calibration. After the relative calibration is applied, a multiplication by 2 x 10^8 yields the final spectrum in $\frac{phots}{s \cdot cm^2 \cdot nm \cdot ster}$.

3.7 Conclusion

The calibration and characterization of the DM was completed through the use of a variety of techniques and measurements. The dark current, stray light, and DC offset were determined by taking two closely spaced measurements with the same exposure time, where, in one of the measurements, the incident skylight was blocked by a closed shutter. This dark current image was subtracted from the scientific image. The resultant image is the incident signal that must be intensity calibrated. Each pixel on the CCD was calibrated to determine its central wavelength. A second order polynomial was fitted to the measured gas lamp data on either side of the order sorter to determine the wavelength to pixel calibration. A grey-body source with a continuous spectrum was used to determine the relative response of the DM and so convert measured sky spectra to the actual sky spectra. The point spread

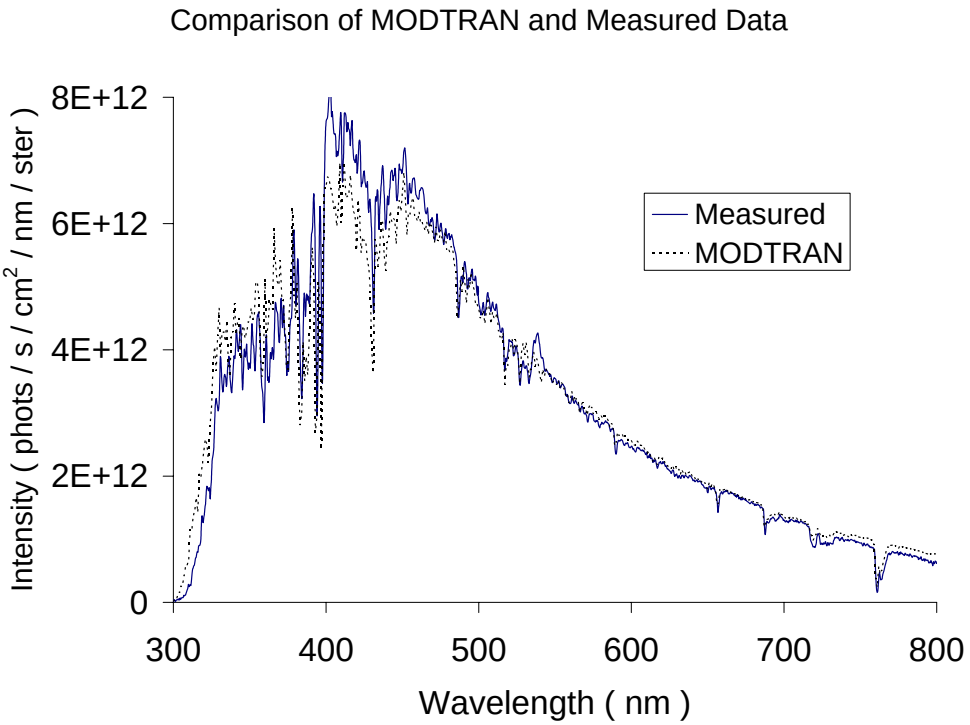

Figure 3.21: Comparison between a spectrum obtained on June 11, 2005 at 9:49 AM local time (SZA = 47°) and the MODTRAN modelled spectrum.

function was also measured in order to allow accurate modelling of the DM output measurements where high spectral resolution is required.

Chapter 4

Radiative Transfer

4.1 Introduction

This chapter will focus on the radiative transfer theory involved with making scattered sunlight measurements from the ground. The absorption and scattering of solar radiation occurs due to electro-magnetic field interactions and can be modelled to determine how the atmosphere alters the signal that reaches the ground. It is these scattering and absorption processes that lead to the characteristic intensity drop of radiation between 400 and 650 nm, known as the Chappuis band. A presentation of the details of the Chappuis band as well as a method for calculating its depth, known as the Chappuis Depth, is also presented in this Chapter. Since the Chappuis Depth is dependent upon the total ozone column, it was modelled for differing ozone amounts to determine the relationship between the two. This led to a conversion between measured Chappuis Depth and the total ozone column in Dobson Units.

4.2 Radiative Transfer Background

The DM measures light that originates at the sun, propagates through the atmosphere, is scattered by molecules and aerosols above Saskatoon, and further propagates downward towards the roof of the Physics Building at the University of Saskatchewan. The fundamental physical principles associated with absorption and scattering of light are addressed in this section along with their relevance in deter-

mining a total column ozone amount.

4.2.1 Absorption

Absorption of solar radiation can occur for a given molecule as long as the photon is energetic enough to change either the vibrational, rotational, or electronic state. With an even greater amount of energy, the molecule may even be photodissociated. For a given molecule each of these four absorption types have an absorption cross section that can be summed to determine the total absorption cross section. The cross section is the effective area presented to the incoming radiation and defines the probability of absorption.

The ozone cross section for photodissociation, σ_{O_3}, is plotted in Figure 4.1. The Chappuis band is labelled as the increase in cross section between 400 and 650 nm and the Hartley band is the increase in cross section between 300 and 380 nm. These two bands account for much of the absorption of visible and UV incoming solar radiation, with the Chappuis band being much smaller in strength than the Hartley band. A typical ozone profile is shown again in Figure 4.2. There is little

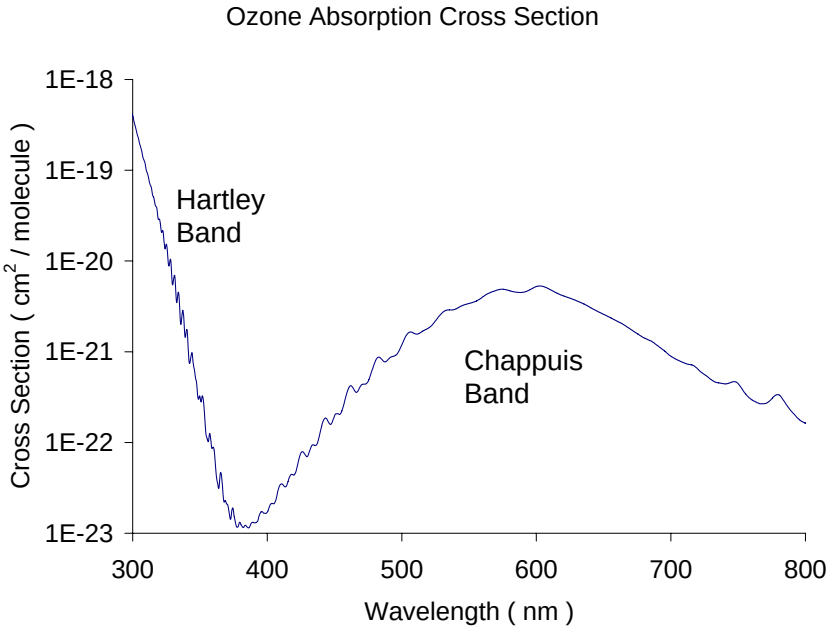

Figure 4.1: Ozone absorption cross section showing the Chappuis and Hartley bands.

ozone density at a height of 50 km, but it increases quickly as the height drops and reaches a maximum near 20 km where the density decreases with height until ground level. Therefore, maximum absorption by ozone occurs near the peak at around 20 km.

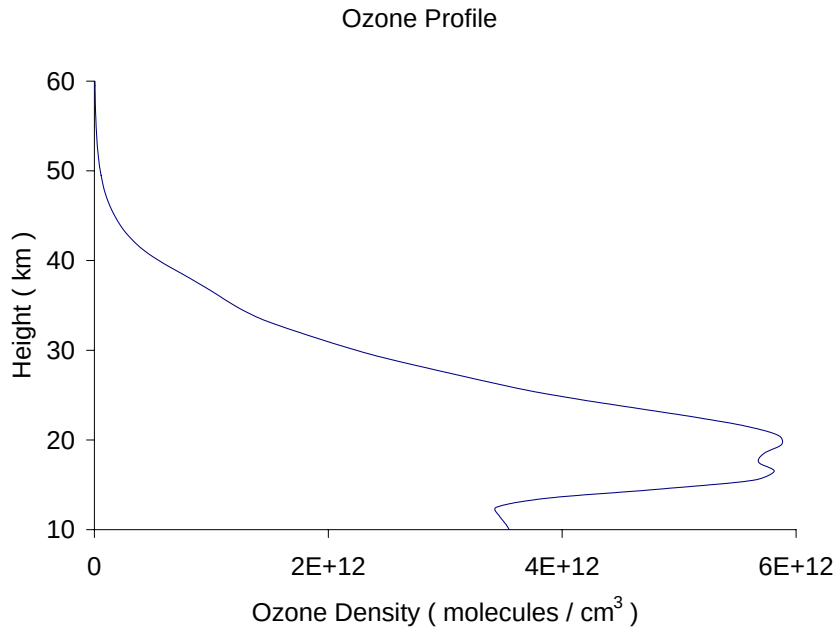

Figure 4.2: Typical mid-latitude ozone density profile measured by OSIRIS above Saskatoon [*Degenstein*, Private Communication].

4.2.2 Rayleigh and Mie Scattering

Rayleigh scattering is the scattering of light by the electro-magnetic field of a molecule. If the molecule is considered to be a spherical dipole scatterer with a radius much less than the wavelength of the signal then the resulting angular distribution of scattered photons is shown in Figure 4.3 and defined by *Liou* [2002] as

$$P(\theta) = \frac{3}{16\pi}(1 + cos^2\theta)\left[\frac{1}{ster}\right], \tag{4.1}$$

where θ is the deviation from the forward direction. This formula predicts the fraction of the signal per steradian that will be scattered in the direction, θ, and consists of two parts, the constant term and the cos^2 term. The constant term is the

scattering due to light polarized perpendicular to the scattering plane while the cos^2 term is the scattering due to light polarized parallel to the scattering plane. The plane of scattering in Figure 4.3 is defined as the plane of the page where parallel polarized light is also in the plane of the page and perpendicularly polarized light is pointing out of the page. This shows the effect of perpendicular polarized light (1), the effect of parallel polarized light ($\cos^2\theta$), and the effect of unpolarized light ($1 + \cos^2\theta$), which is merely the combination of the previous two. Light that is polarized in the perpendicular direction is independent of the scattering plane while parallel polarized light scatters strongly in the on-axis direction and not at all in the off-axis direction. The resultant combination of these two scattering polarizations gives the unpolarized result, which scatters strongly in the on-axis direction and weakly in the off-axis direction. The on-axis direction is, by definition, a scattering angle of 180° or straight ahead.

More rigorous analysis of the air molecules results in a corrected scattering probability. The difference is due to molecular oxygen and nitrogen not being perfect spherical dipole scatterers. This corrected scattering probability is defined by *Brasseur and Solomon* [1986] as

$$p(\theta) = \frac{.7629}{4\pi}(1 + 0.932cos^2\theta)\left[\frac{1}{ster}\right]. \tag{4.2}$$

This directional scattering probability, along with the Rayleigh scattering cross section, σ_R, is used in the equation of transfer to determine the amount of scattering radiation from each molecule. The general Rayleigh scattering cross section from *Liou* [2002],

$$\sigma_R(\lambda) = \frac{8\pi}{3}a^2\left(\frac{2\pi a}{\lambda}\right)^4\left(\frac{\varepsilon_r - 1}{\varepsilon_r + 2}\right)^2, \tag{4.3}$$

where ε_r is the relative permittivity and a is the molecular radius, is basically a $\frac{1}{\lambda^4}$ dependence. This Equation may also be modified for non-spherical molecules, resulting in the corrected Rayleigh scattering cross section from *Brasseur and Solomon* [1986],

$$\sigma_R(\lambda) = \frac{4 * 10^{-28}}{\lambda^{3.916+.074\lambda+.05/\lambda}}[cm^2], \tag{4.4}$$

where λ is the wavelength in microns. The Rayleigh scattering cross section multiplied by the directional scattering probability is defined as the total directional

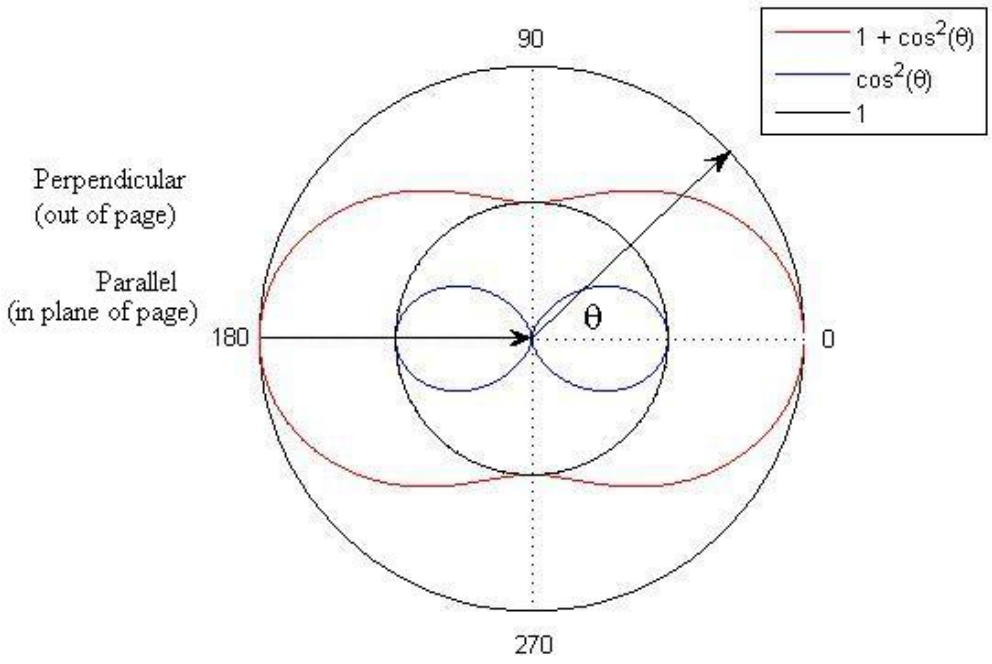

Figure 4.3: Distribution of Rayleigh scattering for incident light that is polarized perpendicular (1), parallel ($\cos^2\theta$), and randomly ($1 + \cos^2\theta^2$). Note the maximum scattering in the forward and backward directions and the minimum scattering perpendicular to the incident light ray.

scattering cross section,

$$\sigma_R p(\theta) \left[\frac{cm^2}{ster}\right]. \tag{4.5}$$

In order to determine the probability that a photon will be Rayleigh scattered in a given direction the total directional scattering cross section must be multiplied by the number density and path length through an atmospheric layer.

Figure 4.4 shows the modelled response for a solar input spectrum after it has been Rayleigh scattered. The solar spectrum starts off low and rises with a fairly constant slope to a maximum near 600 nm where the incoming radiation levels off. The amount of Rayleigh scattered light depends on the wavelength as it has a strong $\frac{1}{\lambda^4}$ dependence. Since short wavelength light is scattered much better than longer wavelengths, the scattered signal is more intense in the short wavelength end of the

spectrum.

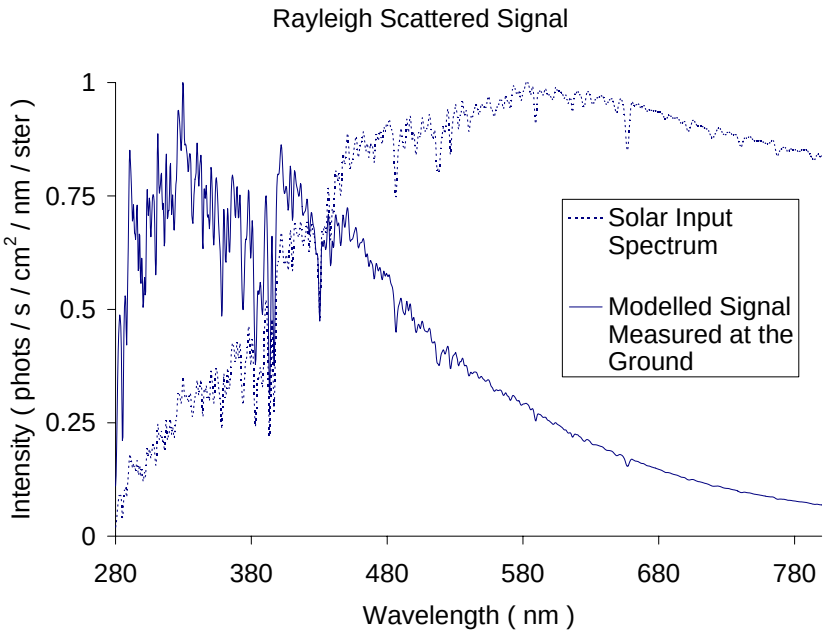

Figure 4.4: Modelled Rayleigh scattered spectrum for a solar input spectrum. The spectra have been normalized for ease of comparison.

Mie scattering theory is used when the wavelength of the incoming signal is comparable in size to the scattered particle. Mie scattering occurs with such particles as dust, water droplets, ice crystals, etc. The main differences between Mie and Rayleigh scatter are that Mie scattering tends to scatter predominantly in the forward direction and has a flatter spectral response ($\sim \frac{1}{\lambda^{1.5}}$). Rayleigh scattering is dominant so the Mie scattering will not be addressed further.

4.2.3 Extinction

A photon moving through the atmosphere may be either scattered or absorbed. Whether or not it interacts with a given species is dependent upon the cross section and number density of that species. Figure 4.5 shows an atmospheric layer of thickness, ds, with the variables responsible for the absorption of a photon, where σ_χ is the scattering or absorbing cross section of a molecule, χ, and n_χ is the number density of the molecule. For this small layer of atmosphere, the incoming intensity

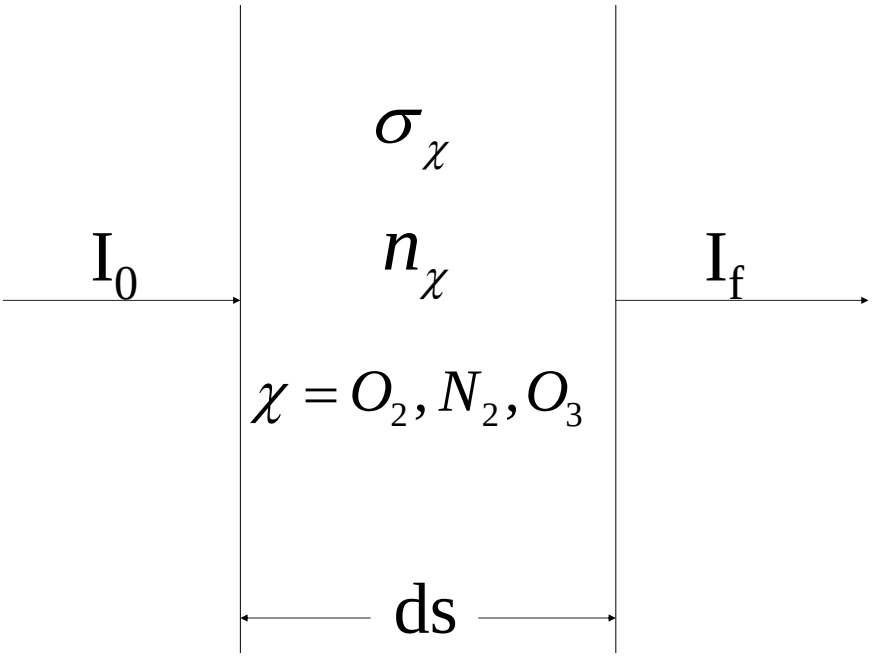

Figure 4.5: Schematic of absorption of solar radiation incident upon an atmospheric layer.

is I_0 and the outgoing intensity is $I_0 + dI$ where dI is the change in the intensity defined by,

$$dI = -I_0 \sigma n ds. \tag{4.6}$$

Note that only one species is considered here. This can be rearranged as

$$\frac{dI}{I_0} = -\sigma n ds, \tag{4.7}$$

then integrated over s to obtain

$$ln(I)\Big|_{s_0}^{s_f} = \int_s -\sigma n ds, \tag{4.8}$$

which simplifies to

$$I_f = I_0 e^{-\tau}, \tag{4.9}$$

where I_f is the final intensity at the output of the shell, I_0 is the incident intensity of the solar radiation and τ is the optical depth defined by

$$\tau = \int_s \sum_{\chi} \sigma_{\chi} n_{\chi} ds, \tag{4.10}$$

where all scattering and absorbing species are now considered.

Using the small layer model of Figure 4.5 with I_0, a flat input spectrum, σ_{O_3}, the ozone cross section, σ_R, the Rayleigh cross section, n_{O_3}, the ozone density at a specific height, n, the total density at a specific height, and ds, the path length through the atmosphere, an output spectrum, I_f, can be determined. Figure 4.6 shows plots of output spectra with σ_{O_3}, σ_R, n_{O_3}, and n at heights of 10, 23, and 36 km, and a path length of 110 km, corresponding to the maximum path length through a 1 km layer of the atmosphere at a solar zenith angle of 90°. The plot shows the normalized intensity proportional to $\frac{phots}{s \cdot cm^2 \cdot nm \cdot ster}$. The Chappuis band absorption is evident as the dip between 400 and 650 nm and the Hartley band absorption is evident as the sharp drop in intensity around 325 nm. In the plot of the 10 km output spectrum the dominant term is the Rayleigh scattering, which is evident by the $\frac{1}{\lambda^4}$ dependence of the curve that is seen at all wavelengths. The Rayleigh scattering term becomes more dominant due to the sharp drop in the ozone number density and the increase in the overall number density of the atmosphere.

4.2.4 The Equation of Transfer for the DM Measurements

The DM measures Rayleigh scattered light in the zenith above Saskatoon in order to determine the total ozone column concentrations. Figure 4.7 shows how light that enters the atmosphere consisting of N homogenous (constant temperature and pressure) shells is scattered. An incoming light ray at solar zenith angle, θ, traverses the path, Δl, through each shell above the scattering height. It is attenuated through each layer before it is scattered downward towards the detector; after scattering it is again absorbed as it passes through each shell of thickness, Δz. The monochromatic intensity of radiation reaching the ground after the absorption through each layer is

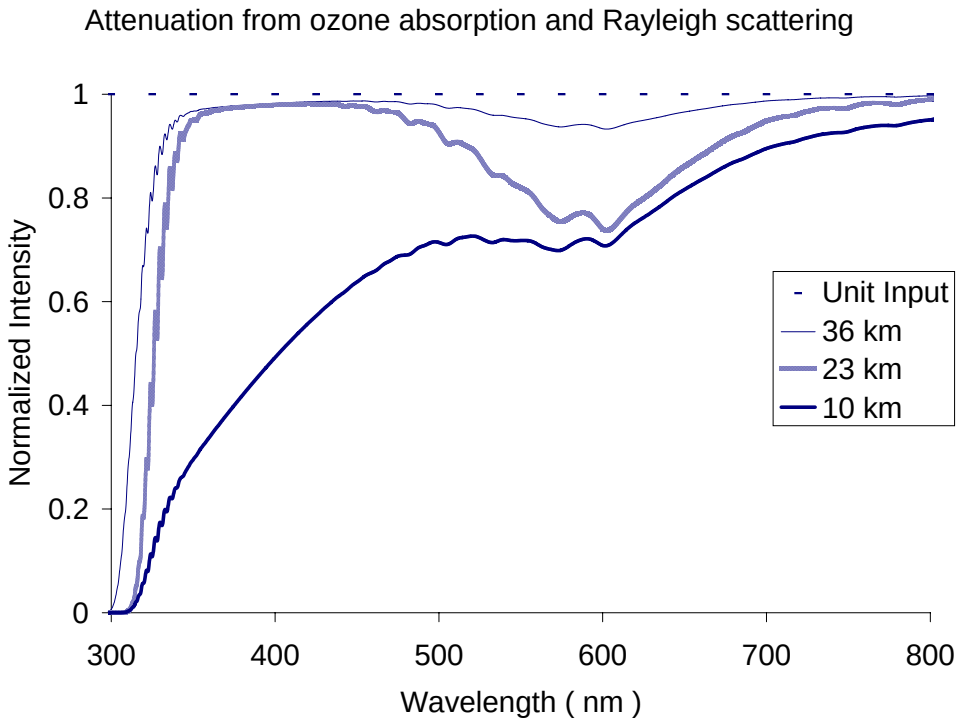

Figure 4.6: Modelled output spectra based on ozone absorption and Rayleigh scattering for a unity input spectrum.

determined by the following:

$$I(z=0,\theta) = I_0 \sum_{i=1}^{N} \left[\sum_{\chi} \sigma_{i,\chi} n_{i,\chi} p_{\chi}(\theta) \Delta z_i \right] exp \left[- \sum_{j=i+l}^{N} \Delta\beta_j \right] exp \left[- \sum_{k=1}^{i} \Delta\tau_k \right], \tag{4.11}$$

where

$$\Delta\beta = \left[\sum_{\chi} \sigma_{j,\chi} n_{j,\chi} \right] \Delta l_j \tag{4.12}$$

and

$$\Delta\tau = \left[\sum_{\chi} \sigma_{k,\chi} n_{k,\chi} \right] \Delta z_k. \tag{4.13}$$

In the above equations I_0 is the intensity of light above the atmosphere, σ is the cross section (defined in Equation 4.3), n is the number density, and $p_{\chi}(\theta)$ is the directional scattering probability given in Equation 4.1. $\Delta\beta$ and $\Delta\tau$ are both optical depths and are given by Equations 4.12 and 4.13 respectively. $\Delta\beta$ is the optical depth for

the path through a shell above the scattering height while $\Delta\tau$ is the optical depth for the path through a shell below the scattering height and both use cross sections for scattering and absorption. The subscript, i, in the equations denotes the values for the i^{th} layer and the subscript, χ, denotes the species involved. It is important to note that the first summation in Equation 4.11 ($\sum_\chi \sigma_{i,\chi} n_{i,\chi} p_\chi(\theta) \Delta z_i$) denotes the scattering at height, h, and uses the cross section for both Rayleigh and Mie scattering.

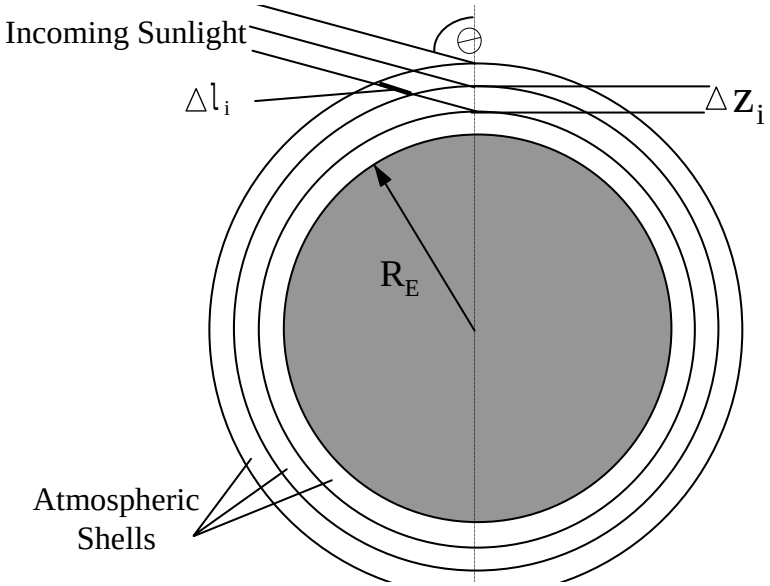

Figure 4.7: Atmospheric shells used in the radiative transfer model.

4.3 The Chappuis Depth

The Chappuis Depth as an indicator of ozone will be presented in this section. This band of ozone absorption has a clear signature in the measured solar spectrum at the ground and can be used as an indicator of ozone amounts in the total column. Details of the calculation of this indicator will be described in the following section using modelled MODTRAN spectra as a visual tool for the explanation of the Chappuis Depth.

4.3.1 The Chappuis Band

The Chappuis band is a region in the solar spectrum between 400 and 650 nm that is sensitive to absorption by ozone and was first characterized by *Chappuis* [1880]. The Chappuis band is a result of the ozone molecule absorbing a photon and dissociating down to atomic and molecular oxygen and consists of an irregular series of vibrational bands that have a maximum absorption cross section at 602.5 nm [*Bacis et al.*, 1998]. The Chappuis band has also been found to have very little dependence on temperature as shown by *Brion et al.* [1998], which results in greater accuracy in modelled data. Figure 4.8 shows the MODTRAN modelled zenith brightness where the absorption in the Chappuis band is clearly indicated.

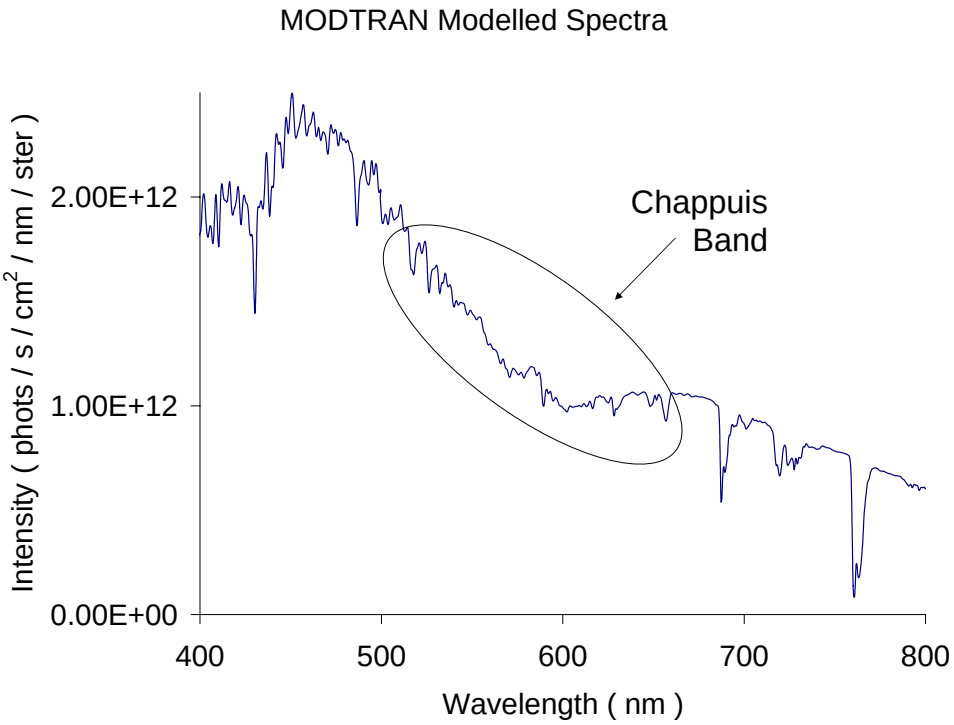

Figure 4.8: MODTRAN modelled spectra showing the Chappuis band absorption.

4.3.2 The Chappuis Depth

Definition

The Chappuis Depth is calculated through a method similar to that used by *Flittner et al.* [2000] and is defined as

$$ChappuisDepth = ln\left(\frac{\sqrt{I'_1 \cdot I'_3}}{I'_2}\right), \tag{4.14}$$

where

$$I'_x = \frac{I_x(SZA)}{I_x(SZA_{ref})} \tag{4.15}$$

is the intensity measured at wavelength x for any solar zenith angle divided by the intensity measured at the same wavelength at some reference solar zenith angle. By definition the calculated Chappuis Depth determines a spectral deviation from a straight line normalized to the deviation for the reference SZA, SZA_{ref}. For this work an SZA_{ref} of 83° is used. Equation 4.14 can be rewritten as

$$ChappuisDepth = \frac{1}{2}ln(I'_1) + \frac{1}{2}ln(I'_3) - ln(I'_2), \tag{4.16}$$

and in this form it is obvious that the Chappuis Depth is the difference between $ln(I'_2)$ and the average value of $ln(I'_1)$ and $ln(I'_3)$. Note the Chappuis Depth at the reference solar zenith angle of 83° is always zero. Figures 4.9, 4.10, and 4.11 better demonstrate the process used to calculate the Chappuis Depth. Figure 4.9 shows the MODTRAN modelled spectra for solar zenith angles of 83°, 85°, 87°, and 89°. Only wavelengths relevant to the Chappuis band absorption are shown in the figure, where the wavelengths used in the Chappuis Depth comparison are 528 nm, 596 nm, and 664 nm. The middle wavelength absorbs ozone more strongly than the other two, resulting in a comparison that yields information about the ozone density. The lower solar zenith angles are more intense because the sun is higher in the sky and more light reaches the DM.

Figure 4.10 shows the effect of the normalization on the spectra in Figure 4.9. The intensities at each SZA are divided by the intensity at 83° on a pixel by pixel basis. Figure 4.11 shows the effect of the natural logarithm on the normalized MODTRAN spectra. The wavelengths used in the Chappuis Depth calculation are

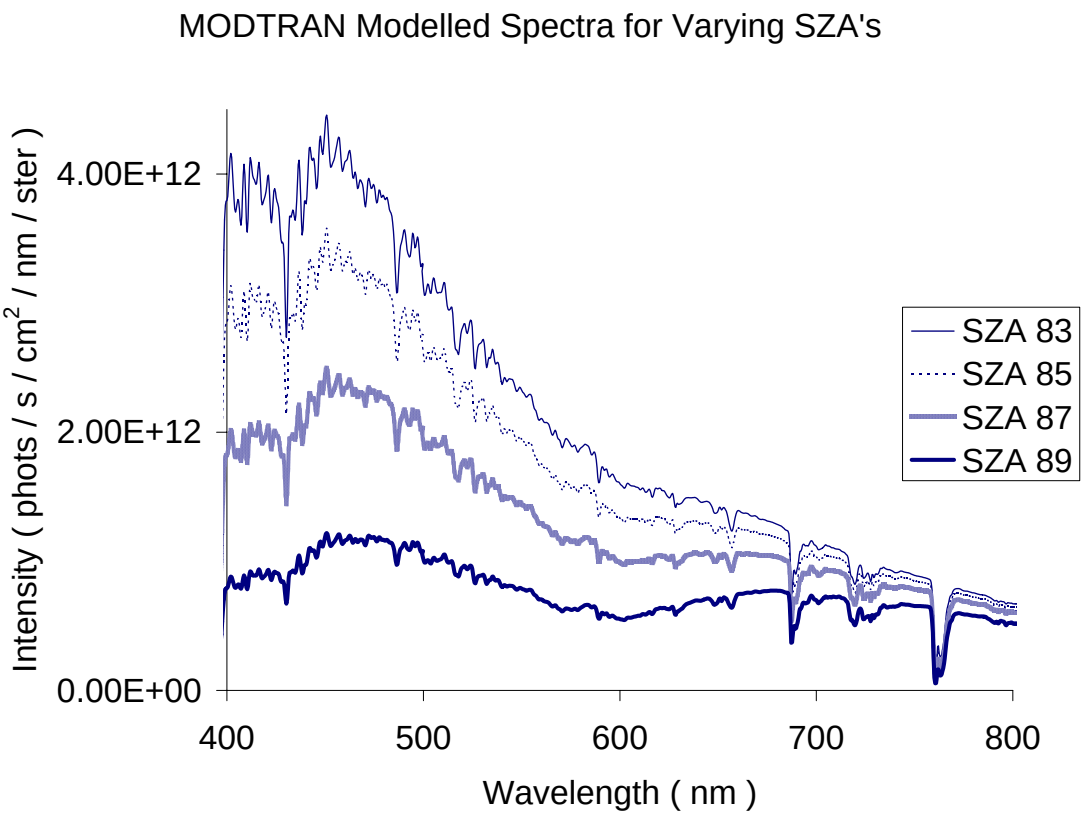

Figure 4.9: MODTRAN modelled spectra for varying solar zenith angles. Note the increase in the depth of the Chappuis band.

shown as well as the physical representation of the Chappuis Depth. If only Rayleigh scattering was present, the natural logarithm of the $\frac{1}{\lambda^4}$ dependence would result in something close to a constant slope. The deviation from a straight line graph is due to ozone absorption and results in the Chappuis Depth measurement. Figure 4.11 shows a small Chappuis Depth for a solar zenith angle of 85°, which increases to higher and higher values as the solar zenith angle increases.

The normalization of the Chappuis Depth to its value at a solar zenith angle of 83° is done in order to allow for comparison of the values obtained on different days. Mie scattering has the effect of reddening the spectrum and will change the calculated Chappuis Depth by a constant offset value. By performing the normalization, the constant offset is eliminated resulting in a data set that may be better compared on a day to day basis. Of course, the signal contains absorption by ozone

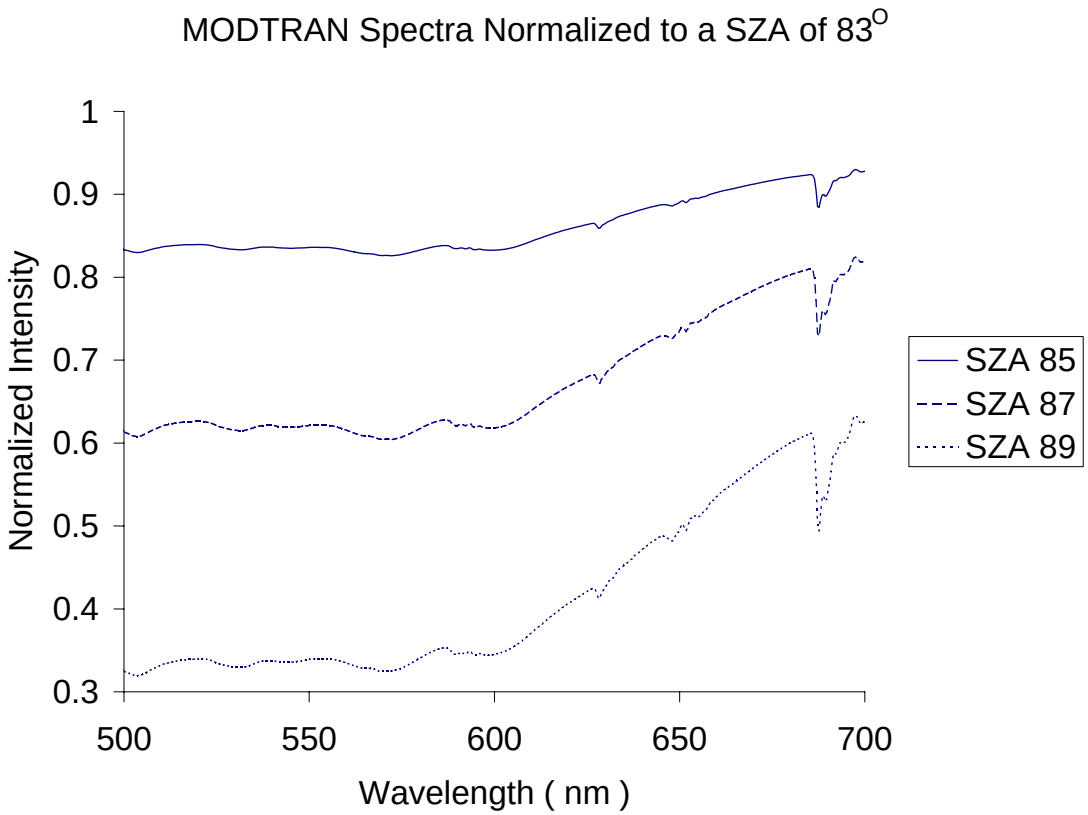

Figure 4.10: MODTRAN modelled spectra normalized to an SZA of 83° at all other SZA's.

at all altitudes and the previous explanation is not entirely valid. However, the exact interpretation of the Chappuis Depth is very similar to this approximation.

Calculation

A simple radiative transfer model was made that assumed single scattering and an ozone profile typical to Saskatoon. This model was run for varying total column ozone amounts, by scaling the ozone profile, and the Chappuis Depths at an SZA of 88° were calculated for each case. Figure 4.12 shows the Chappuis Depth calculation for differing ozone amounts and Figure 4.13 shows the Chappuis Depths for these cases at 88°. The Chappuis Depth increases more quickly for higher ozone amounts resulting in the linear relationship between the Chappuis Depth at 88° and the total ozone column in Dobson Units. This conversion factor is called the Dobson Unit

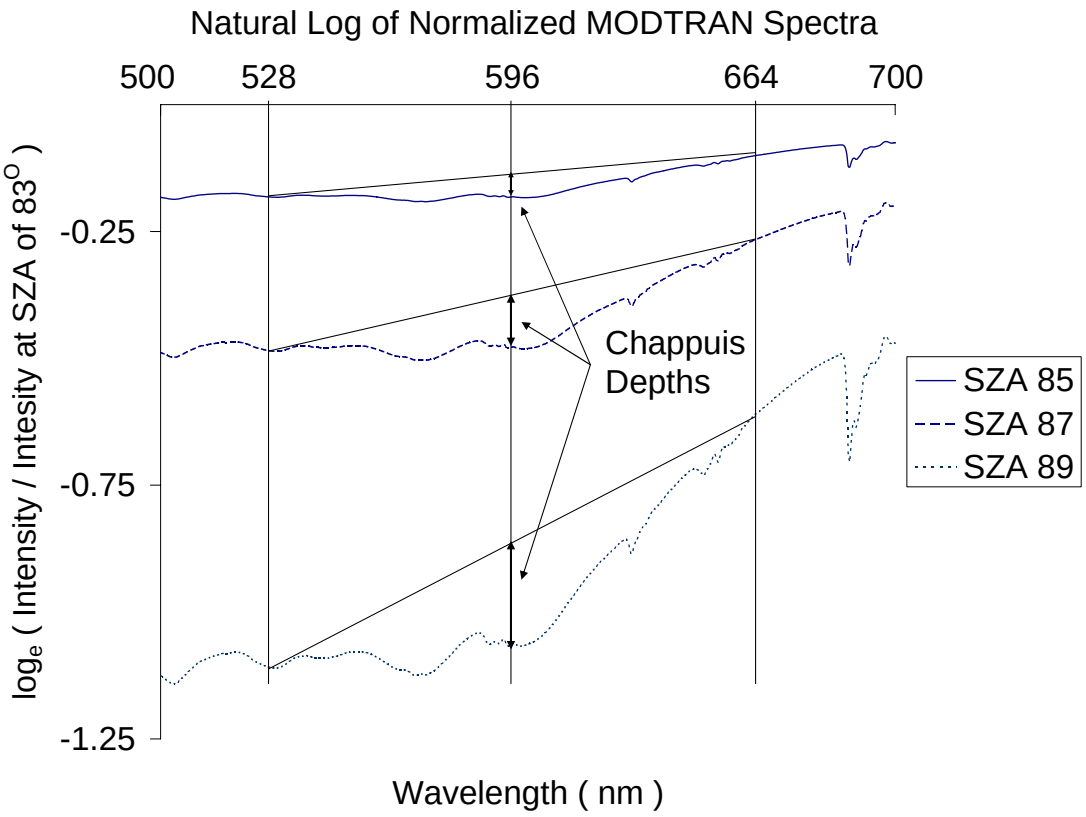

Figure 4.11: Natural log of the normalized MODTRAN spectra with emphasis on the wavelengths used in the Chappuis Depth calculation.

conversion polynomial.

4.4 Conclusion

The processes that govern absorption and scattering in the atmosphere were presented in this chapter. It was shown how extinction of species occurs in the atmosphere and how to calculate the theoretical signal that reaches the ground. The Chappuis Depth was defined and its determining calculations outlined. Radiative transfer calculations were then made using a simple single scatter model in order to determine the relationship between the Chappuis Depth and the total ozone column. This allows the data from a twilight measurement to be converted to a total ozone column in Dobson Units.

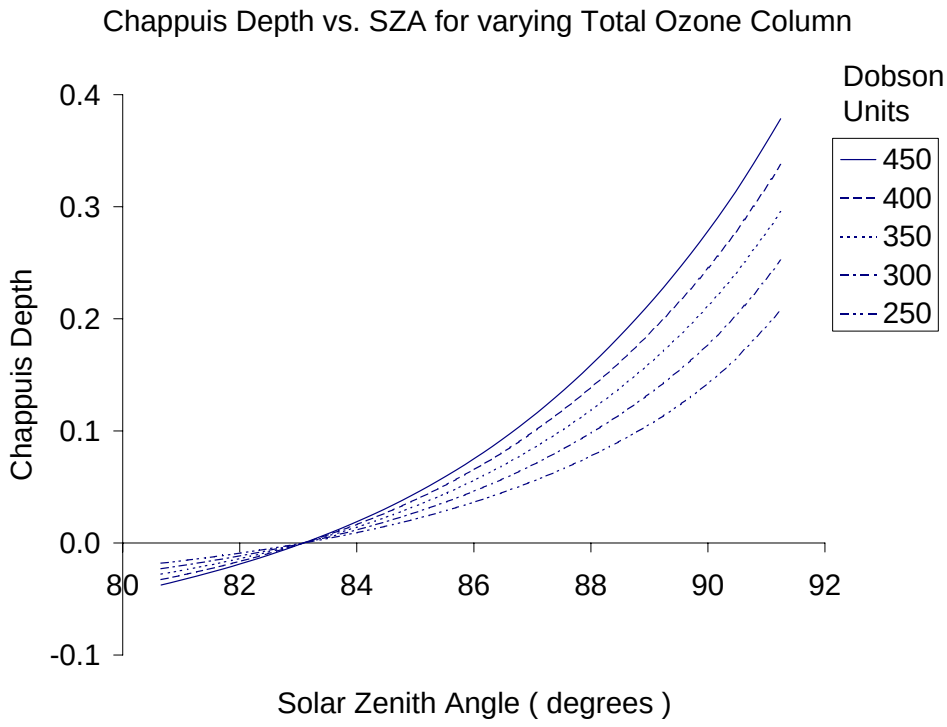

Figure 4.12: Modelled Chappuis Depths for various total ozone columns.

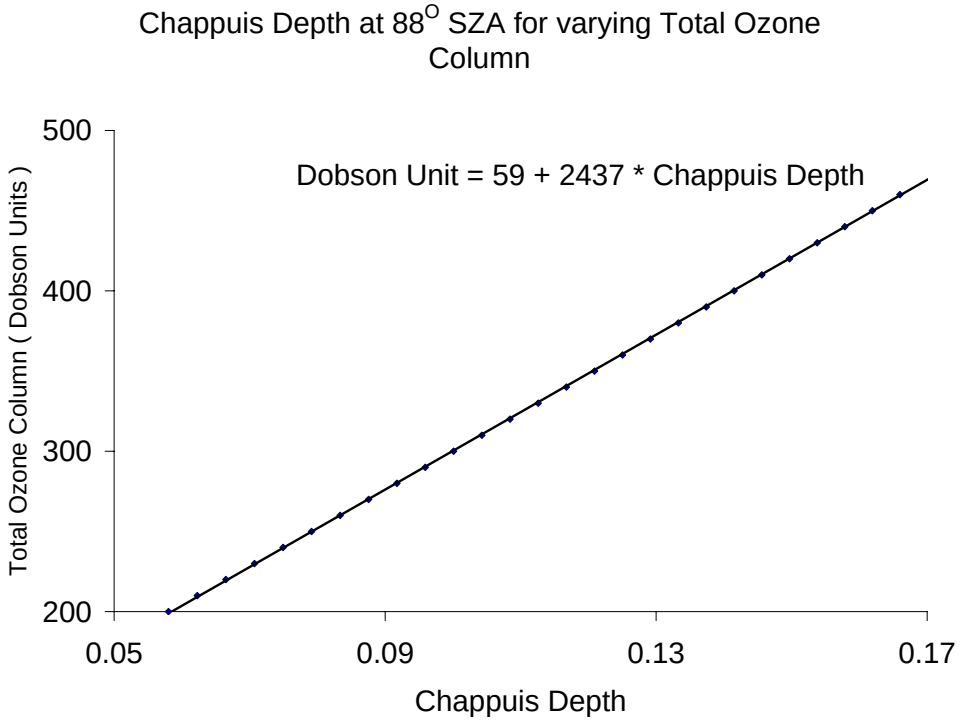

Figure 4.13: Chappuis Depths at an SZA of 88° for various total ozone columns.

Chapter 5

Results

5.1 Introduction

This chapter will focus on the data set collected for the duration of this thesis project and its analysis. The collection of data started at the end of February, 2005, and continues until the present. Spectra were stored individually for each twilight measurement set then archived in a proprietary binary format. These data sets were analyzed over the year to determine the Chappuis Depths, defined in Section 4.3.2, at varying solar zenith angles. The Dobson Unit conversion polynomial was used to determine an approximate total ozone column in Dobson Units and then plotted for analysis. The results are shown in the following chapter.

5.2 Data Collection

A computer was placed in the clean room with the DM to act as a host and run the client program for the data collection process. For a twilight measurement set the DM would take exposures based upon the user-entered variables in the GUI. When the SZA was between the high and low values set in the GUI, an exposure would be taken at the exposure time determined by the previous image. The shutter would then close and another exposure was taken at the same exposure time. These images were then subtracted to remove the dark current, stray light, and DC offset and all were stored on the client computer in a directory for that twilight set. This was done in both morning and evening so that for any given day there are two twilight

data sets. When the data collection completed for a twilight set, the client program would take all the data in the directory, apply the intensity calibration, and make a plot of the spectra over time. A typical measurement set is shown in Figure 5.1 for the morning twilight of September 1, 2005. The data collection started at the top of

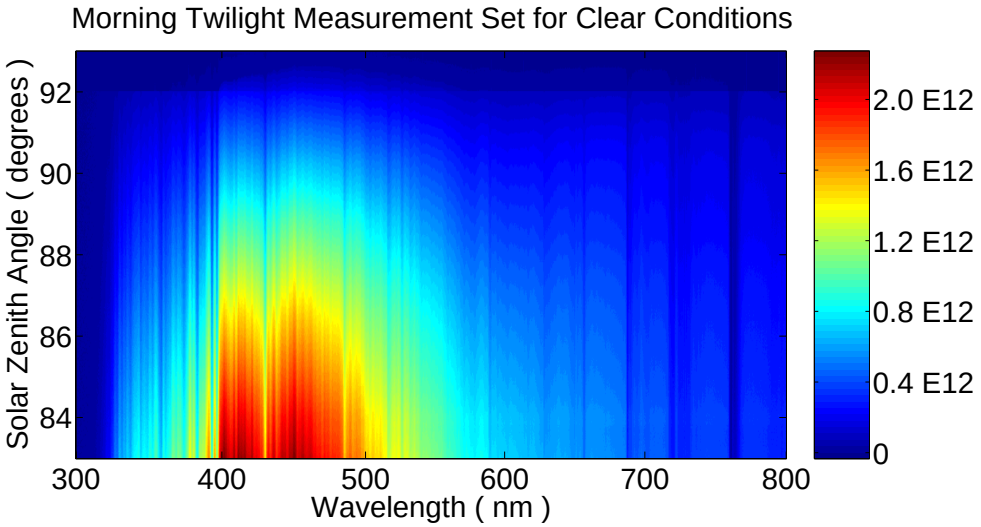

Figure 5.1: Morning twilight data set for September 1, 2005. The color scale on the right is the calibrated intensity in $\frac{phots}{s \cdot cm^2 \cdot nm \cdot ster}$.

the plot at an SZA of 93° and, as the sun rises, data are collected and row after row is added until an SZA of 83° is reached. For this particular twilight measurement set there were 346 spectra obtained and plotted. Figure 5.2 shows cross sections of differing SZA's from the twilight data set in Figure 5.1. The cross sections were taken at solar zenith angles of 83°, 86°, and 89°. As the SZA gets larger the spectra shift to become relatively more intense in the red end, resulting in the deepened Chappuis Depth characteristic of higher SZA's.

The computer code used to control the data collection process was continually being edited and improved and because of this there are some days where there were no collected data. Minor technical issues also contribute to periodic loss of data.

5.3 Cloudy Data Analysis

One problem in taking atmospheric measurements is that there is no constant atmosphere to work with. It is constantly changing from day to day and minute

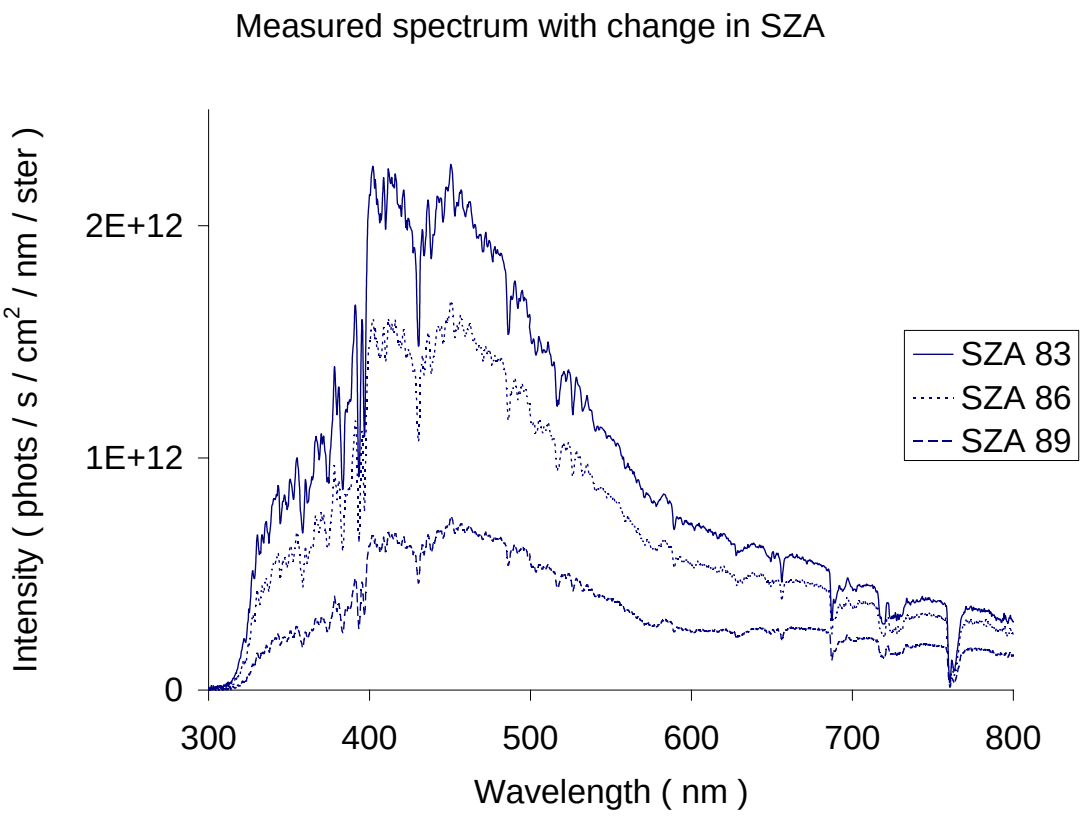

Figure 5.2: Spectra for morning of September 1, 2005, for SZA of 83°, 86°, and 89°.

to minute. A noticeable consequence of the changing atmosphere is the change in brightness due to clouds. Periodic clouds that do not cover the entire sky increase the intensity of the spectrum as measured by the DM while a blanket of clouds will serve to dim the signal. This is because a single cloud will reflect much more light down towards the earth than Rayleigh scattering alone while a cloud blanket is too optically thick for much light to penetrate, leaving the atmosphere darker. For this thesis, three different types of twilight measurement sets have been identified. The first is a clear set, which shows no sign of clouds throughout the entire set of data. The second is partly cloudy, which show no more than 3 obvious clouds and the last type is referred to as overcast as there are many clouds in the field of view. The overcast criterion applies to the majority of days and is the most frequent of the three types of twilight data sets. This section shows the effect of differing amounts

of cloud cover on the obtained data.

5.3.1 Collected Data

Figure 5.3 shows three different twilight data sets comparing the resultant spectra with differing amounts of cloud cover. The first twilight set shown in Figure 5.3 (a) is void of any clouds and is referred to as the clear day. A smooth change in intensity is evident as the solar zenith angle changes. In Figure 5.3 (b), referred to as the partly cloudy day, two clouds drift overhead and then drift out of the field of view one after the other. The first cloud is present at an SZA of 86.6° and the second at an SZA of 88.5°. The data show a characteristic spike in intensity at the solar zenith angles where the clouds pass over. To use as another comparison, Figure 5.3 (c), known as the overcast day, is a twilight data set where the whole sky was clouded over. This data set shows little smooth change and the intensity jumps around noisily.

5.3.2 Cloudy Data Comparison

Cross sections of all three plots in Figure 5.3 are compared in Figure 5.4. These plots show how the changing solar zenith angle affects the measured intensity. The cross sections were plotted for all three twilight measurement sets and for two different pixels. The pixels used were pixel 700 (540 nm) and pixel 350 (403 nm). As discussed previously the shorter wavelength measurement suffers more attenuation from scattering and therefore varies more with SZA than the long wavelength measurement. In both plots the data for the clear day produce a straight line whereas the data for the overcast day show nearly no structure and appears to randomly fluctuate in intensity. The data for the partly cloudy day show the characteristic jump in intensity at both wavelengths, however, the jump is more pronounced in Figure 5.4 (b).

This assumption of a greater intensity increase at higher wavelengths from Figures 5.4 (a) and (b) is confirmed in Figure 5.4 (c). A ratio was taken of the intensity at pixel 700 to the intensity at pixel 350. This division left the clear data as a featureless line and the partly cloudy data showing obvious structure in the vicinity of the cloud. The resultant structure shows that a cloud entering the field of view

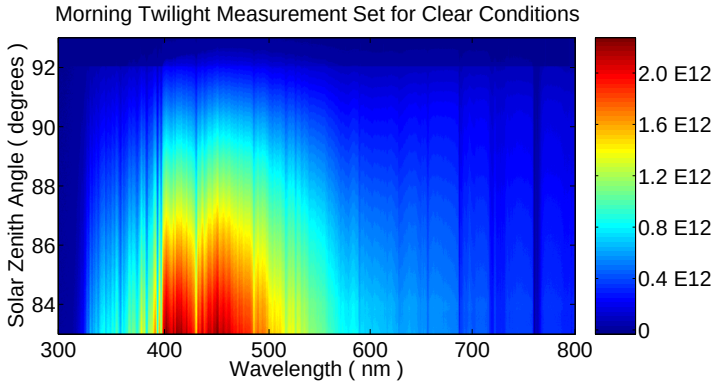

(a) September 1, 2005 morning twilight data set: Clear

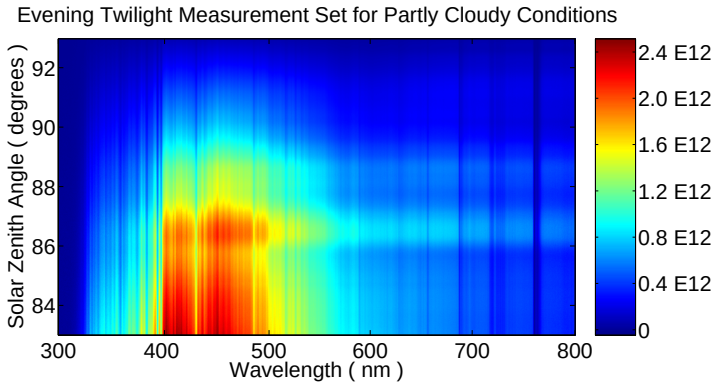

(b) August 21, 2005 evening twilight data set: Partly Cloudy

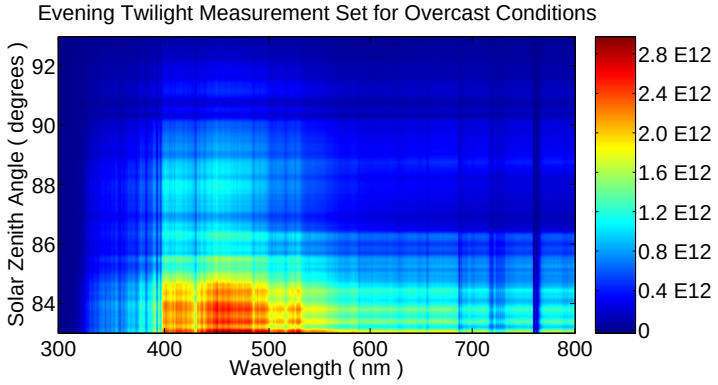

(c) August 9, 2005 evening twilight data set: Overcast

Figure 5.3: Twilight measurement sets for clear, partly cloudy, and overcast conditions. The color scale on the right is the intensity in $\frac{phots}{s \cdot cm^2 \cdot nm \cdot ster}$.

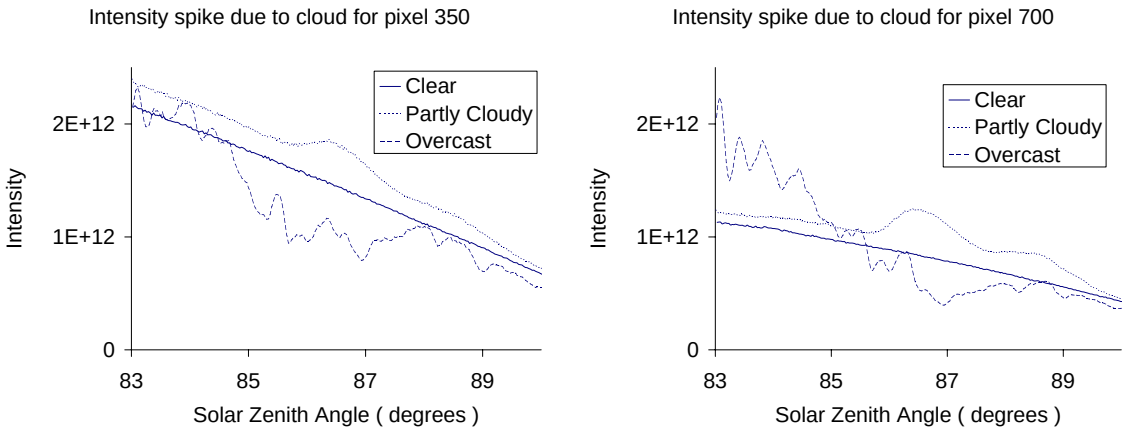

(a) Pixel 350 intensity cross section.

(b) Pixel 700 intensity cross section.

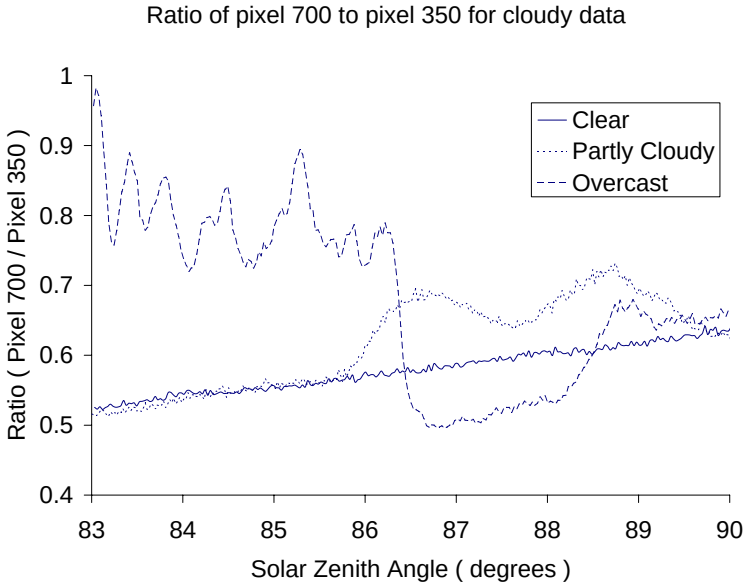

(c) Ratio of pixel intensities.

Figure 5.4: Intensity cross section as a function of solar zenith angle for clear, partly cloudy, and overcast conditions for: (a) pixel 350, (b) pixel 700, and (c) the ratio of the two. The intensities are in units of $phots/s/cm^2/nm/ster$

will shift the intensity higher in the red end of the spectrum. As a comparison tool, the overcast data were also plotted and, as in Figures 5.4 (a) and (b), the intensity is seemingly random. Although not done for this work, this feature could be used for automatic cloud detection.

These three data sets were also compared using their spectral cross section at 83° SZA. Figure 5.5 shows the three days with their spectra at 83°. The clear and partly cloudy spectra both show a spectrum that is free from an overhead cloud while the overcast spectrum shows a spectrum with a cloud in the field of view. The partly cloudy and clear data are very close, with only a slight difference in the measured intensity on the two different days, while the overcast spectrum shows a large red shift along with an overall increase in the intensity. The increase in intensity has the effect of flattening out the spectrum and making it "whiter". This is what one would expect to see on an overcast day as the sky appears to be white or grey when filled with clouds. Note that the cloud cover on the overcast day resulted in an increased signal instead of the decrease expected with a thick blanket. Therefore, it is evident that data taken under overcast conditions are very difficult to analyze.

Figure 5.6 shows how the spectrum changes as the solar zenith angle increases for clear data, Figure 5.6 (a), and for the partly cloudy data where a cloud drifts in and out of the field of view, Figure 5.6 (b). The partly cloudy data show spectra at 85.5°, just before the cloud appears overhead, 86.6°, when the cloud is directly overhead, and 87.8°, just after the cloud has passed over. For comparison, spectra from the same solar zenith angles are plotted from the clear data. The spectrum taken at 86.6° should fall between the other two as in the Figure 5.6 (a), however, the presence of a cloud at this SZA results in the increase in intensity seen in Figure 5.6 (b).

5.3.3 Effect of Clouds on the Chappuis Depth Analysis

Each spectrum taken during a twilight data set was analyzed to determine the Chappuis Depth and then the data was plotted versus the solar zenith angle. This was done using the ratio described in Section 4.3.2 and the result for a typical data set is shown in Figure 5.7. As the sun rises, the solar zenith angle moves from 90° (top of plot) down to 83° (bottom of plot) and the depth of the Chappuis band steadily decreases as a result of the shorter path length through the atmosphere.

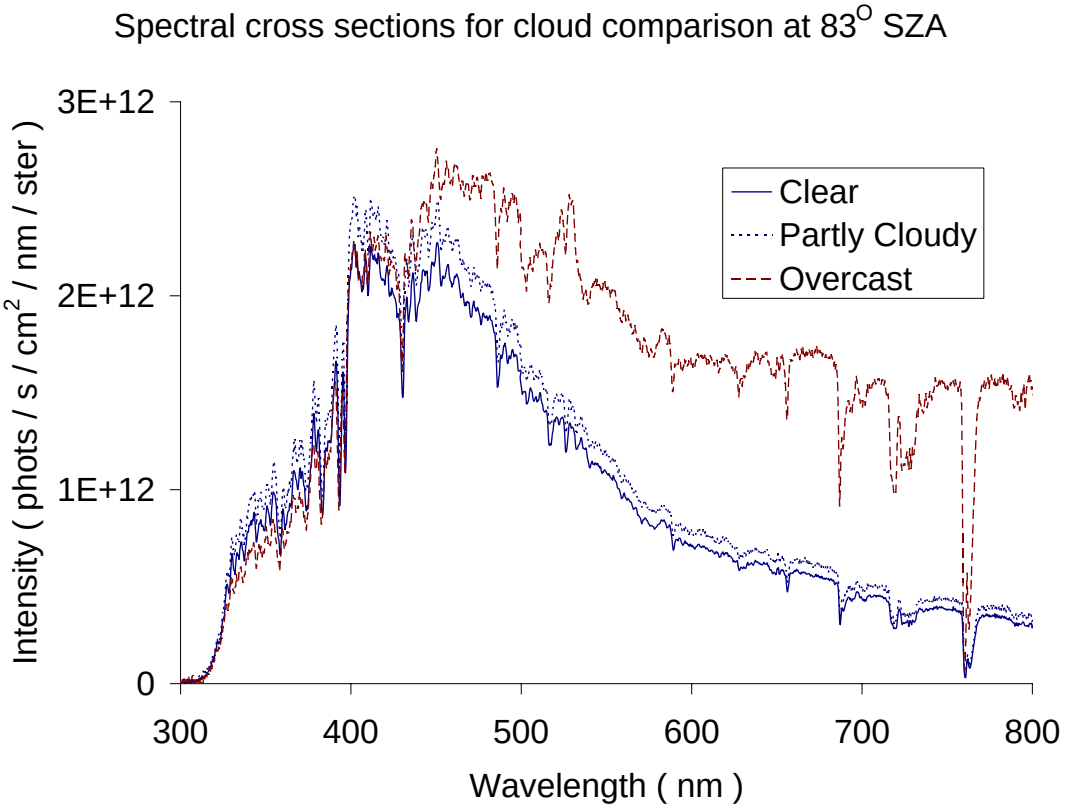

Figure 5.5: Spectral cross section at 83° showing the difference between spectra with and without a cloud in the field of view.

As mentioned in Section 5.3.2, the measured intensity is extremely dependent on the amount of cloud cover, thus a comparison of the days with and without clouds must be made with respect to the Chappuis Depth. How the clouds affect the depth of the Chappuis band is integral to how the data should be processed. Figure 5.8 shows the Chappuis Depth comparison between the clear, partly cloudy, and overcast days. The clear and partly cloudy data appear to follow each other extremely well. Though the trends all appear to be the same, the clear data seem to be slightly higher than the partly cloudy data with the overcast data even higher still. The slight highness of the clear data may be because the data were taken in the morning as opposed to the partly cloudy data taken in the evening. This is a result of this thesis paper and will be discussed in Section 5.5. The overcast data are higher because of the thick optical depth of the cloud cover. When the sun is

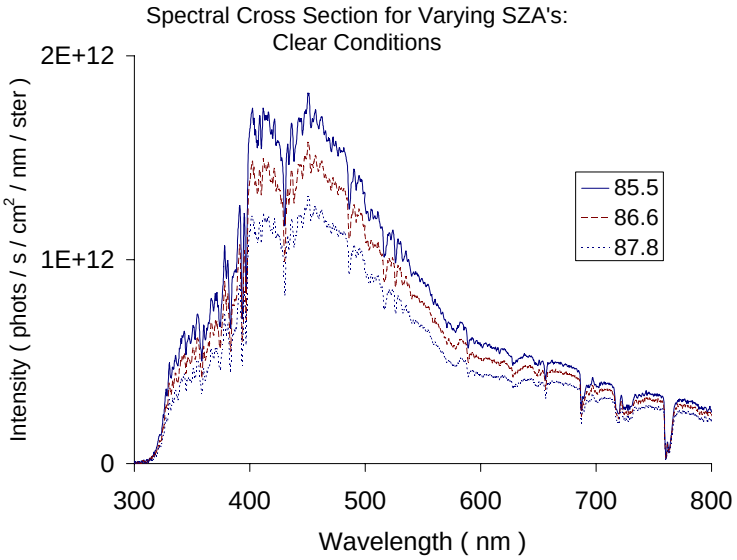

(a) Typical spectral cross sections for clear conditions.

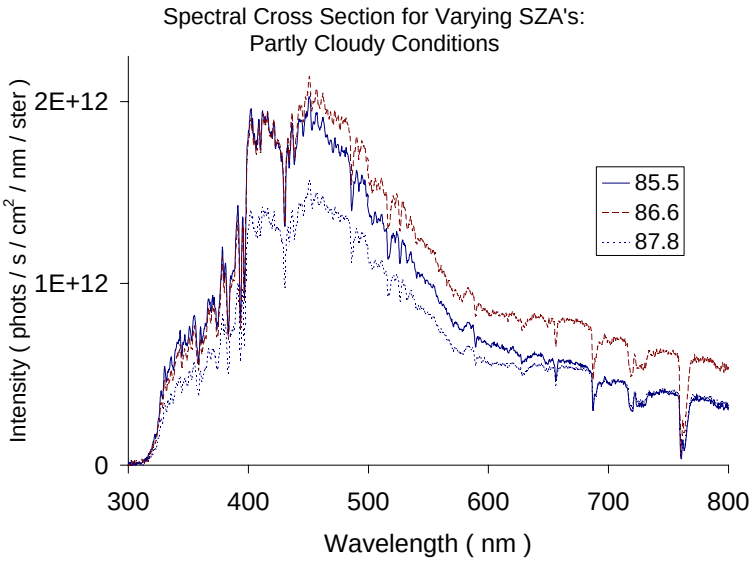

(b) Spectral cross sections showing cloud overhead at 86.6°.

Figure 5.6: The effect of a cloud on measured spectra.

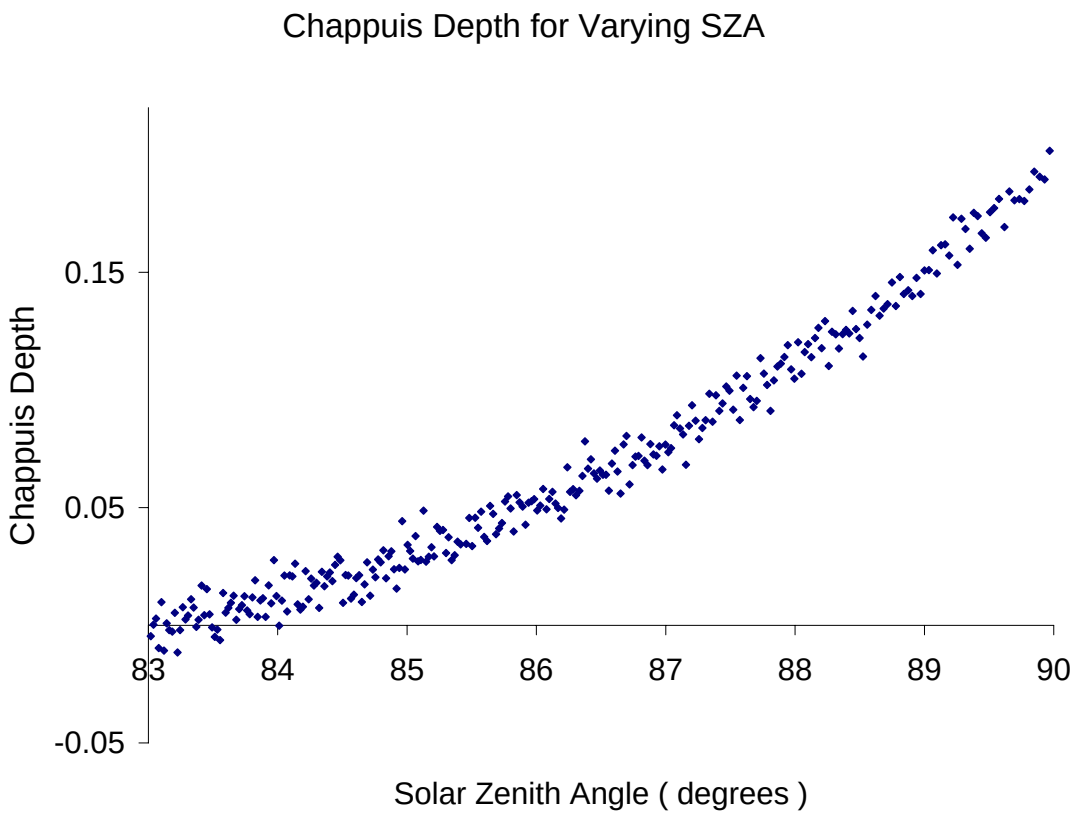

Figure 5.7: Variation of the Chappuis Depth with increasing SZA for the September 21, 2005 morning twilight data set.

high at the start of the measurement set the intensity is comparable to that of the clear day. As the sun lowers, the path length through the clouds becomes too great and the intensity of the light reaching the DM is greatly reduced. This results in the quickened change in the Chappuis Depth depicted in Figure 5.8. Because of the difference in the Chappuis Depth for varying amounts of cloud cover, it was decided that only clear data would be used to study the total ozone column. Any inclusion of cloudy data in the analysis would require a deeper study of the effects of clouds on the measured data sets and is beyond the scope of this thesis.

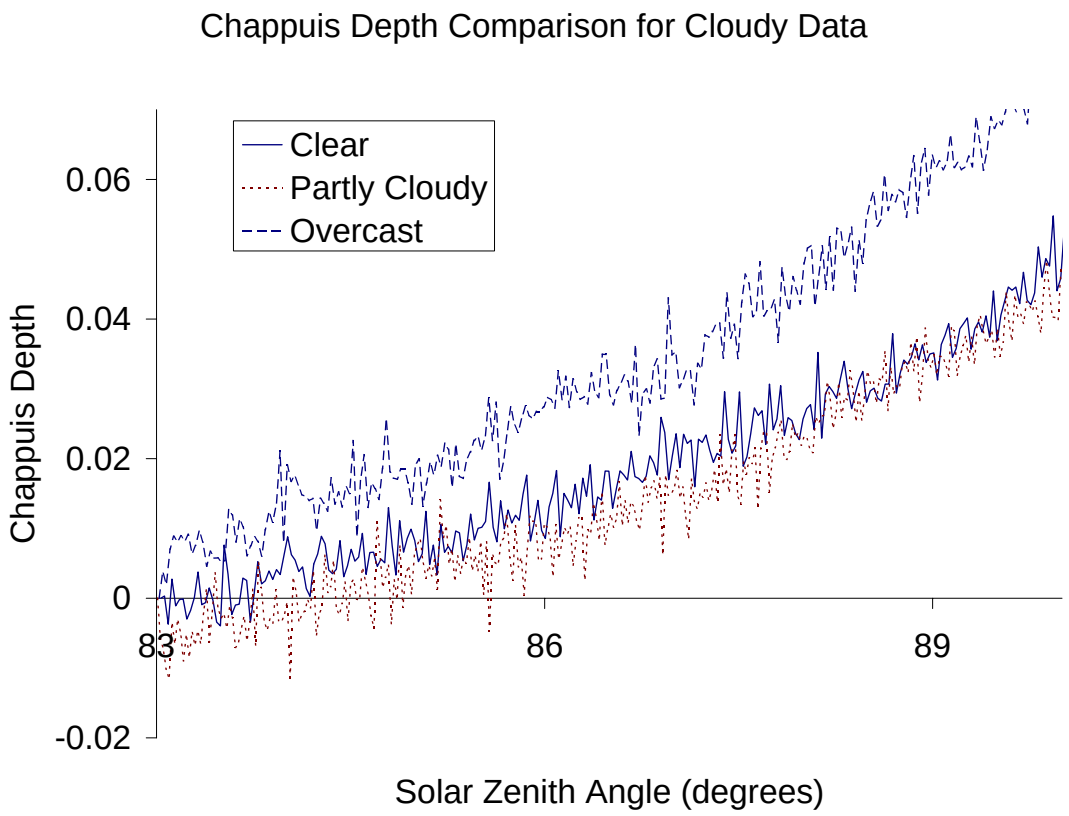

Figure 5.8: Variation of the Chappuis Depth as a function of SZA for clear, partly cloudy, and overcast data.

5.4 Error in the Calculated Chappuis Depth

The Chappuis Depth was calculated for all collected spectra through the use of Equation 4.14, previously defined in Chapter 4 as

$$ChappuisDepth = ln\left(\frac{\sqrt{I_1' \cdot I_3'}}{I_2'}\right), \tag{5.1}$$

where I' is the calibrated intensity at a given SZA divided by the calibrated intensity at a reference SZA. This normalization allows the error analysis to be performed on the DN that results after the removal of dark current and DC offset (see Figure 3.4). Any absolute or relative calibration factor divides out during the normalization and

the Chappuis Depth reduces to

$$ChappuisDepth = \frac{1}{2}\ln(DN_1) + \frac{1}{2}\ln(DN_3) - \ln(DN_2) - \ln\left(\frac{DN_{1_{ref}} \cdot DN_{3_{ref}}}{DN_{2_{ref}}}\right), \tag{5.2}$$

where the DN are those measured at the given wavelengths and the last term in the sum corresponds to the DN at the reference SZA and is a constant throughout a given twilight measurement set. The error in the Chappuis Depth is calculated through error propagation as

$$\delta CD = \sqrt{\frac{\delta DN_1^2}{4 \cdot DN_1^2} + \frac{\delta DN_3^2}{4 \cdot DN_3^2} + \frac{\delta DN_2^2}{DN_2^2}}. \tag{5.3}$$

The error in the DN has two sources, the Poisson noise associated with the number of electron produced by the CCD and the error in the dark current. The readout electronics were designed to give one DN for every 13 electrons and a dark current error of 5 DN was found in Section 3.2. Therefore the error, δDN_x, is

$$\delta DN_x = \sqrt{\frac{DN_x}{13} + 5^2}. \tag{5.4}$$

Substituting Equation 5.4 into Equation 5.3 yields the total error in the Chappuis Depth, which is dependent only upon the digital number read from the DM after the dark current and DC offset subtraction, but before the relative calibration. Figure 5.9 shows a plot of the varying Chappuis Depth with its corresponding error.

A 2nd order polynomial is fit to the Chappuis Depth data over a twilight set to determine the best approximation to the Chappuis Depth at any point. To determine the error in the polynomial at 88° SZA the errors for each individual Chappuis Depth were used. The error in the Chappuis Depths at SZA's between 87.8° and 88.2°, corresponding to approximately 20 data points, were used to determine a weighted average, which is the error in the polynomial at 88°. This error is approximately one-third that of each individual error.

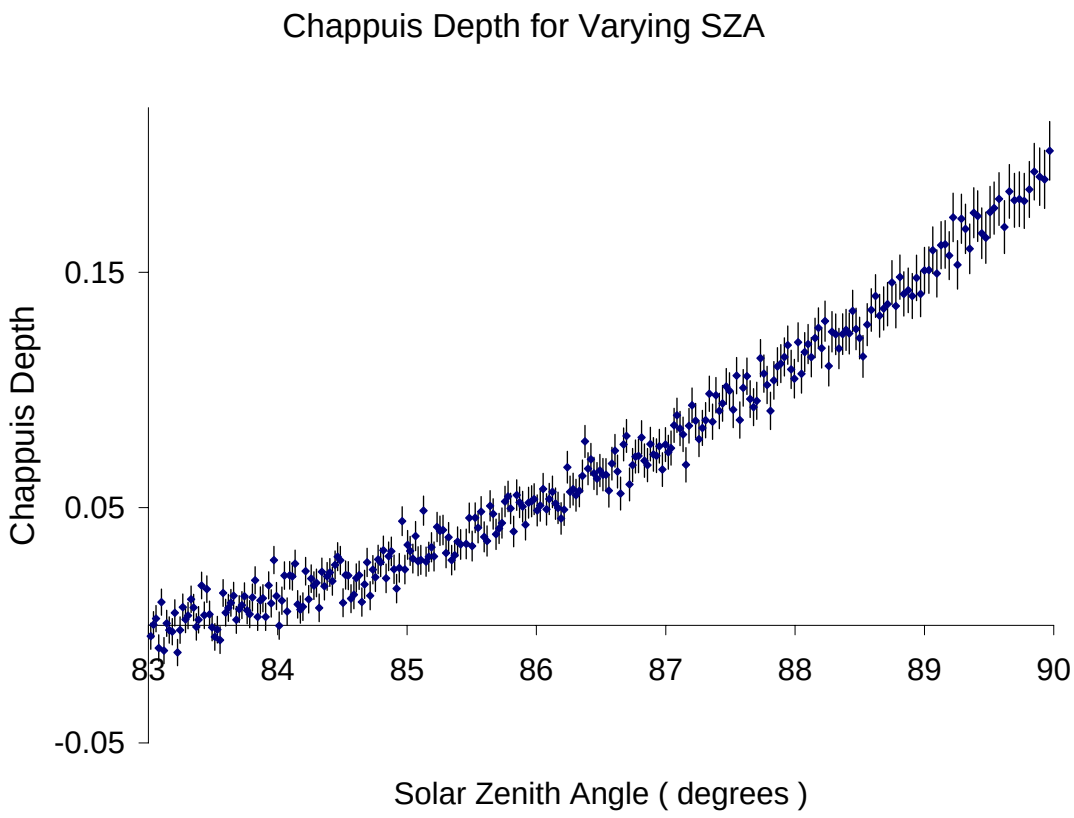

Figure 5.9: Variation of the Chappuis Depth with increasing SZA and corresponding error for the September 21, 2005 morning twilight data set.

5.5 Results

The analyzed data will be presented in the results section. The method used in determining the total column ozone in Dobson Units is described and applied to the collected data. The total ozone column is then compared with that of TOMS in order to determine the accuracy of the measurements.

5.5.1 Dobson Unit Calculation

The calculation to convert data from a twilight measurement set to a total ozone column in Dobson Units was outlined in Chapter 4. The process involves determining the second order polynomial fit of the Chappuis Depth and then using the value

at an SZA of 88° in the conversion equation determined in Chapter 4 and shown on Figure 4.13. Figure 5.10 shows the polynomial fit to the collected data along with the calculated Chappuis Depth for a total ozone column of 270 Dobson Units. The amount of ozone for this day, as determined by the Dobson Unit conversion polynomial, is 270.0711 Dobson Units. Notice that the two curves do not line up exactly at low SZA's but line up well at higher SZA's. Further investigation requires an analysis of systematic errors contained in the radiative transfer model and is beyond the scope of this work.

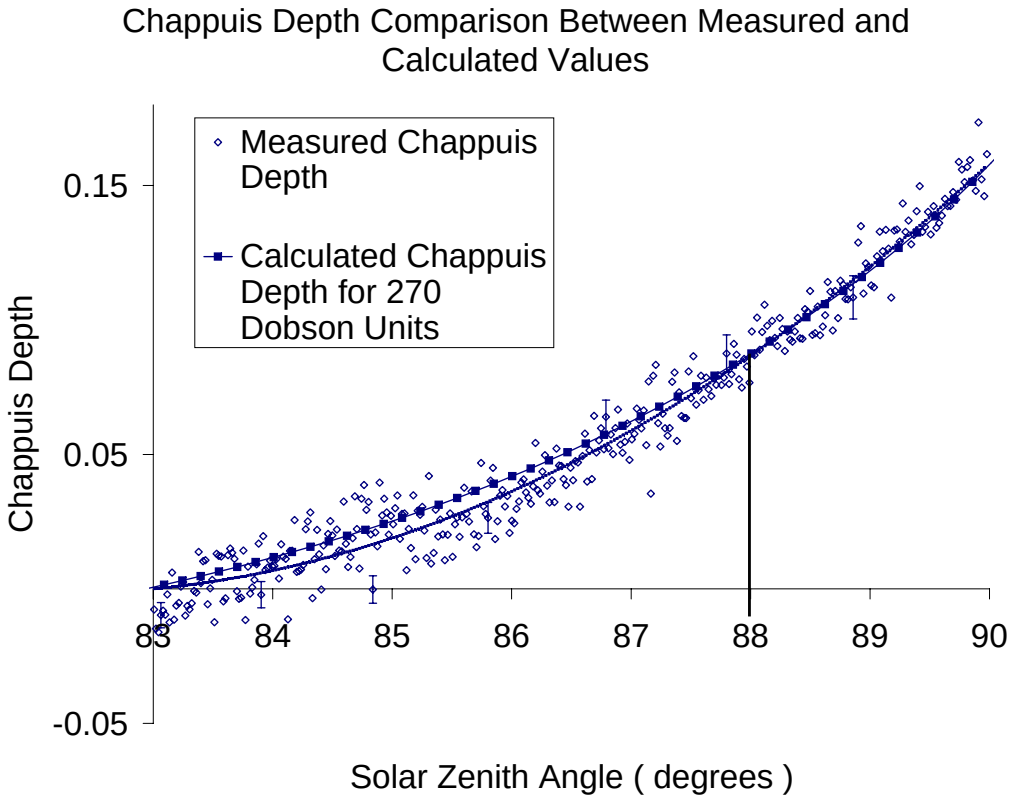

Figure 5.10: Chappuis Depth for the September 2, 2005 evening twilight data set showing the calculated Chappuis Depth using a total ozone column of 270 Dobson Units.

5.5.2 Presentation of Results

The Dobson Unit conversion was carried out for all data in order to analyze and compare with TOMS data. Figure 5.11 shows only clear twilight data sets along with data collected from TOMS for the same days. The analyzed data appear to correlate decently with the TOMS data with a small uncertainty in the calculated total ozone column. The error bars do not include uncertainty in the modelled spectra used to determine the Dobson Unit conversion polynomial.

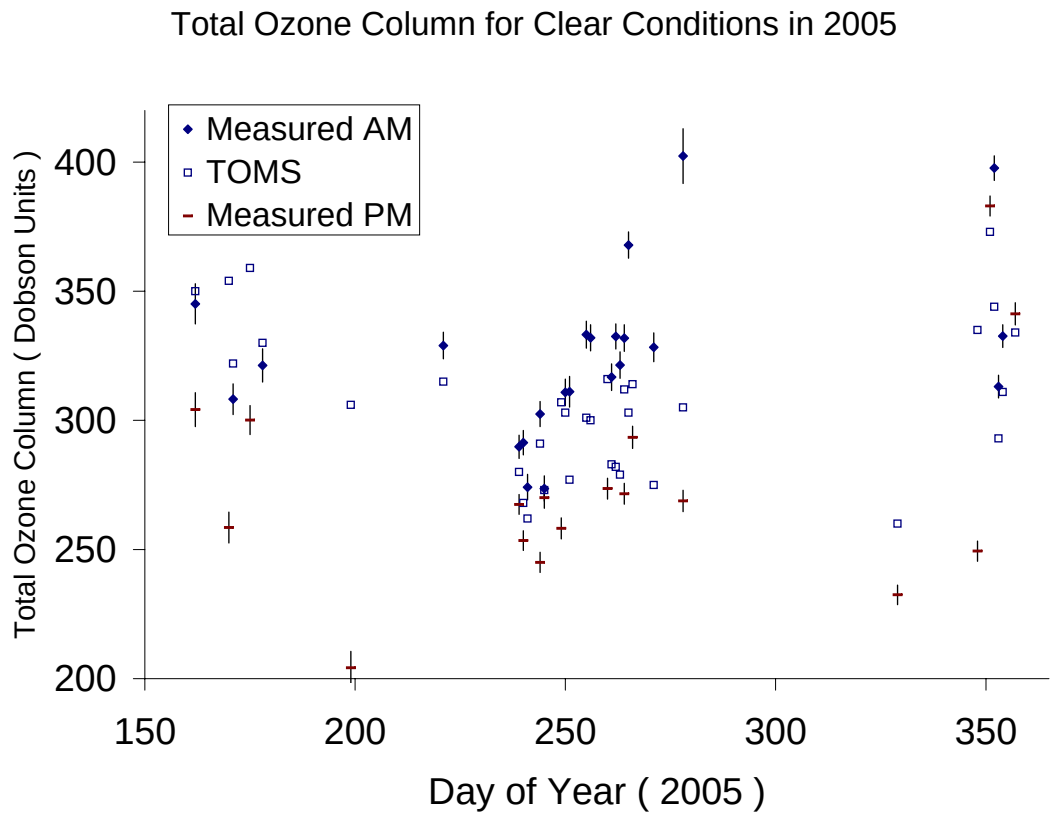

Figure 5.11: Comparison between the total ozone column determined from the DM (including error) and TOMS.

It should be noted that there is a considerable difference between the calculated total ozone column in the morning and in the evening. The morning ozone column is consistently greater than that determined in the evening. This is shown in Figure 5.12 for all days where there is a clear data set in both twilight periods. It is apparent that the morning ozone amounts are generally higher than those measured by TOMS

while the evening ozone amounts are generally lower than those measured by TOMS. TOMS data are taken at local noon, thus it makes sense that the measured total ozone column lies between those determined by the DM measurements.

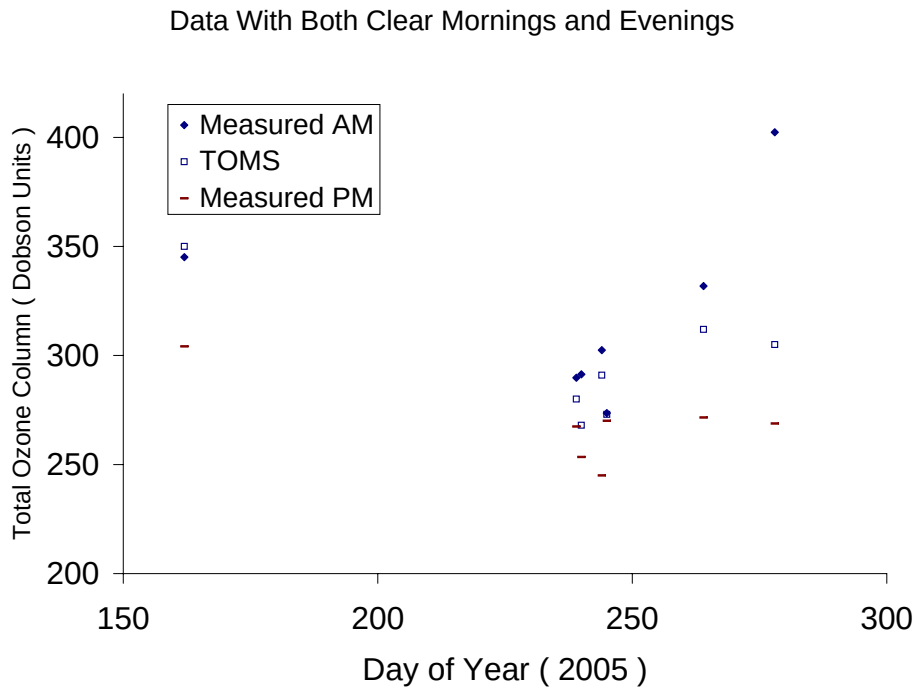

Figure 5.12: Total ozone column for days with both clear morning and evening data sets.

Comparisons of all data, regardless of the type of cloud cover, are shown in Figure 5.13 and Figure 5.14. In Figure 5.13 every twilight data set obtained thus far have been included. It is quite apparent from this data that the total column ozone is regularly greater in the morning. Figure 5.14 shows only the data collected for 2006 and from this graph it is again apparent that there is a greater ozone amount in the morning.

Photochemical theory predicts a diurnal variation opposite to that measured. In the troposphere ozone is produced by factories as a pollutant and builds up throughout the day, resulting in a diurnal variation opposite to the one measured. In the mesosphere, where the density of ozone is extremely small, all the ozone is photodissociated during the day and built up during the night. This predicts a diurnal effect as measured but is a minor contributor as the ozone density is so small

at these heights. This means that the diurnal ozone variation should come from the stratosphere where the majority of the ozone column is but theory says that there is no such variation. Figure 5.15 better shows the diurnal variation. The scatter plot shows nearly all morning measurements above the 45° line and nearly all evening measurements below the 45° line, indicating a diurnal variation of ozone.

5.6 Conclusion

The analysis chapter has shown the data set collected over the past year. An analysis of cloudy data showed an increase in overall intensity and a general red shift in the data due to clouds in the field of view. It was also determined that the effect of clouds on measured data required the dismissal of cloudy data. The data were analyzed to show the calculated total ozone column in Dobson Units and its comparison with data obtained from TOMS. A trend in daily ozone was observed with consistently higher ozone values in the morning as compared to the evening.

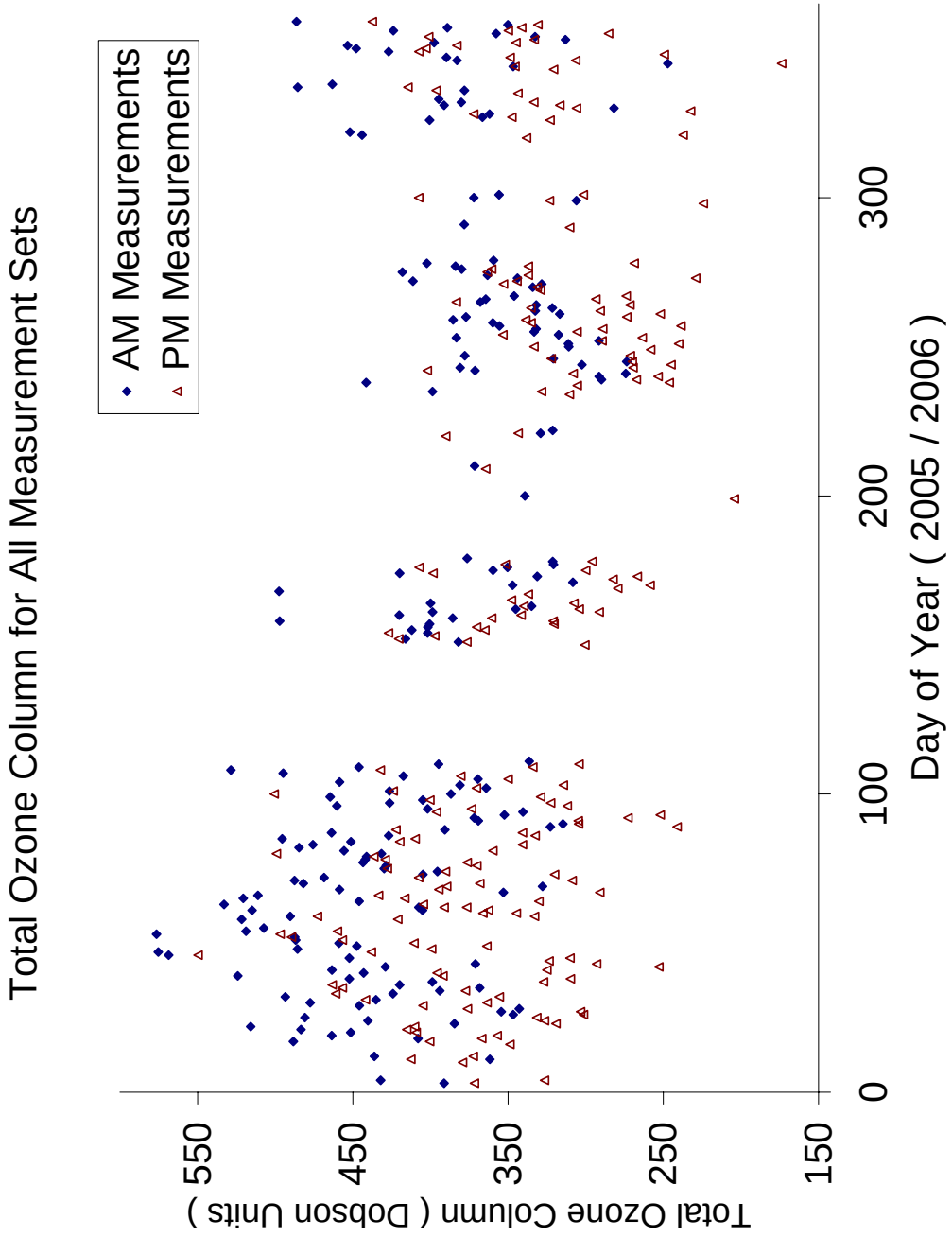

Figure 5.13: All twilight measurement sets obtained including all cloudy data.

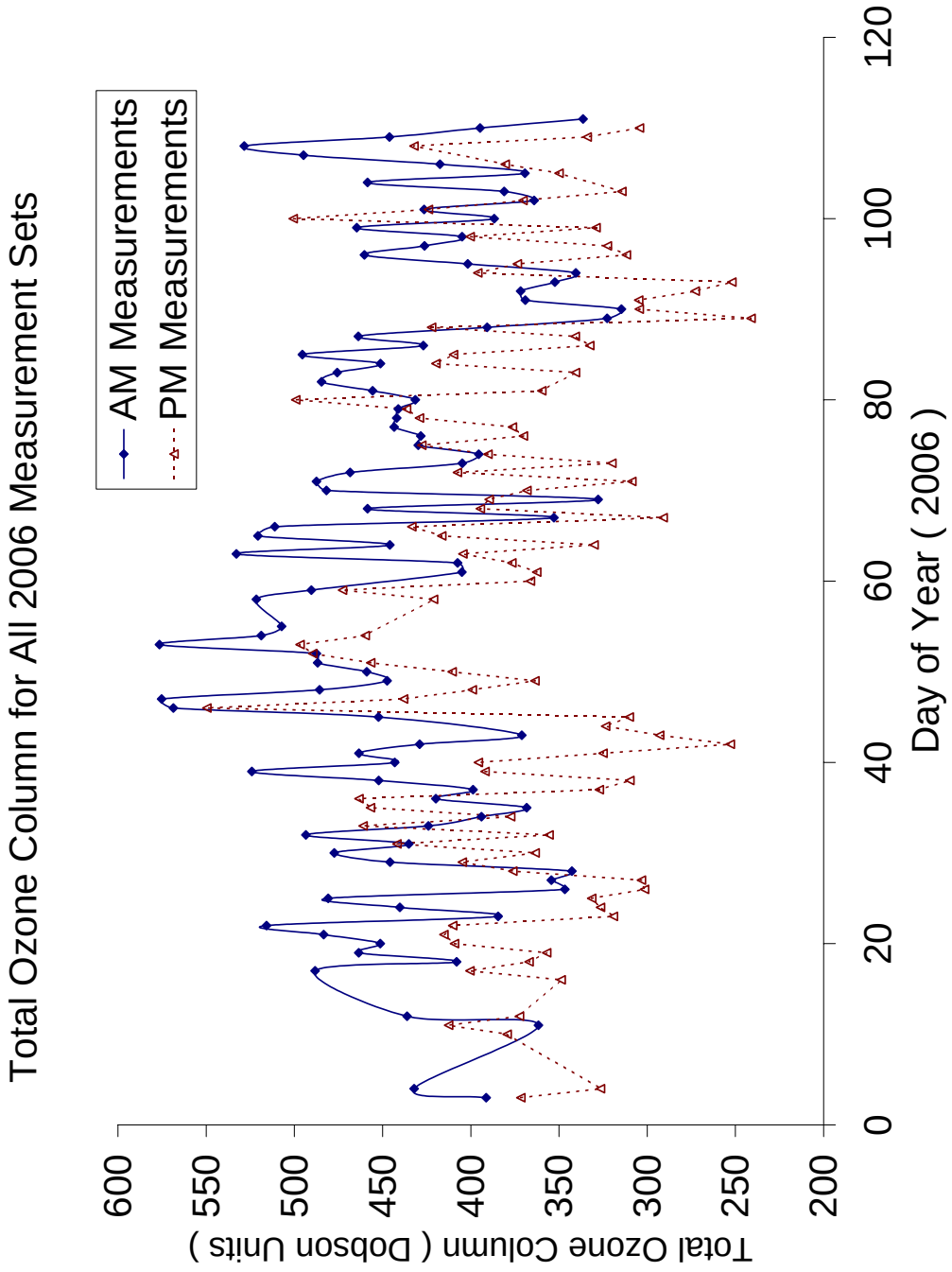

Figure 5.14: Twilight measurement sets including all cloudy data for 2006.

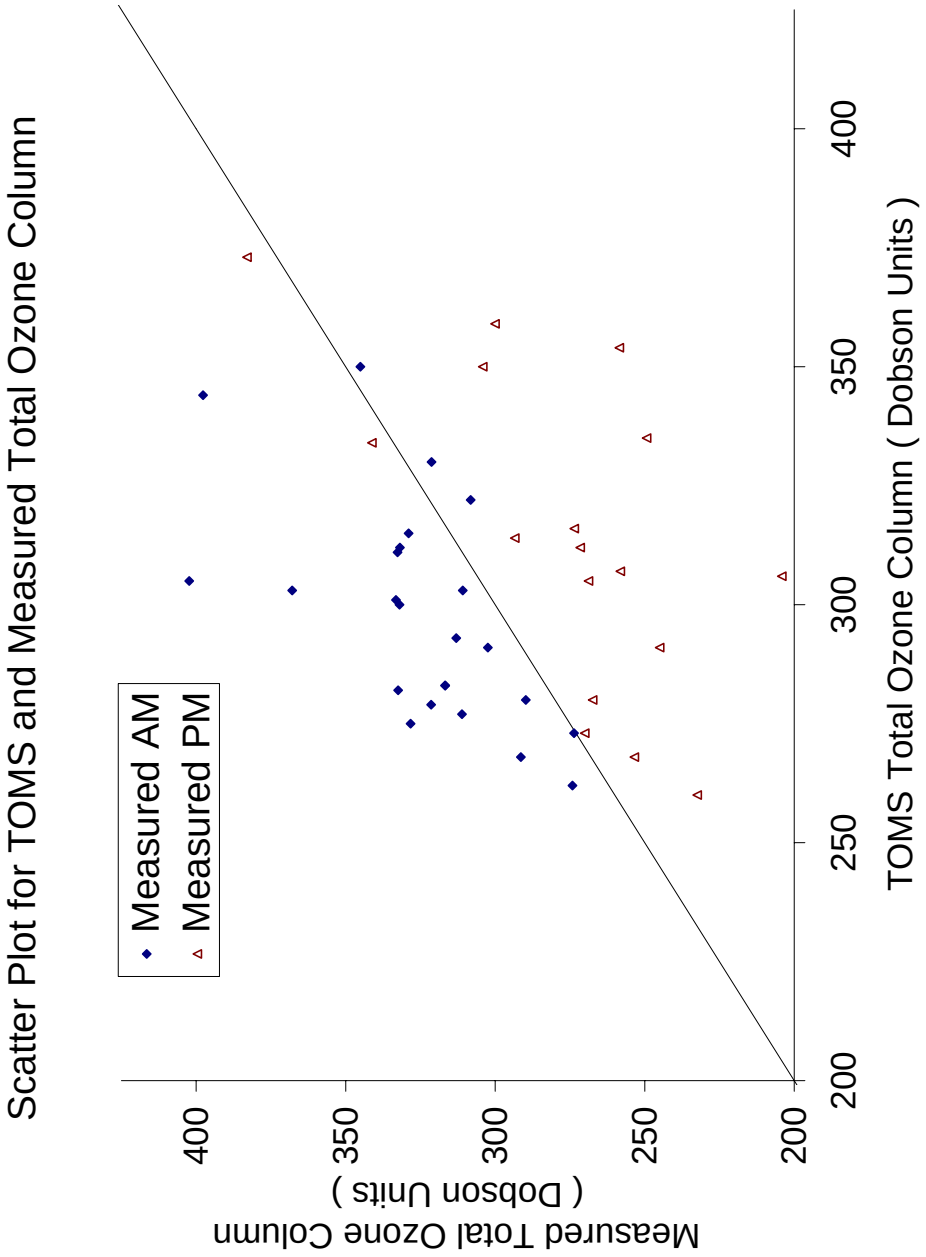

Figure 5.15: Scatter plot showing the variation of AM and PM measurement sets with TOMS data for 2005

Chapter 6

Conclusion and Recommendations

6.1 Summary

The work presented in this thesis project has involved automating the OSIRIS Developmental Model for ground-based measurements of scattered sunlight in the zenith over Saskatoon and a determination of the total ozone column to illustrate the instrument's capabilities. The DM is housed in a clean room in the Physics Building at the University of Saskatchewan in order to minimize dust collection on the important optical surfaces.

The sky signal was transmitted to the DM optics by means of a fiber optic cable that matched the input characteristics of the parabolic mirror collector and the DM. A shutter system was designed and implemented in order to remove dark current from collected data. The shutter system required the design and fabrication of a weather resistant hatch on top of the Physics Building as well as shutter circuitry and a computer interface. Computer control software was designed to facilitate measurements of the scattered sunlight during both the morning and evening twilight hours. This software runs continuously and automatically adjusts the exposure time to compensate for the changing intensity of skylight at both sunset and sunrise.

The DM was calibrated for its wavelength response, its point spread function, the pixel to pixel intensity ratio, and for dark current. As only one row of the CCD output was used, row 16, these calibrations have only been evaluated for that row. The wavelength response of the DM extended from 266.63 nm at one edge of the CCD to 809.91 nm at the opposite edge. Both the point spread function and

relative intensity ratio were calculated for all pixels on row 16 of the CCD. The shutter system allowed the capture of a dark current image that was subtracted from the science image to remove the thermally generated signal.

6.2 Results

The data collected for each twilight measurement set was analyzed to determine the Chappuis Depth as a function of solar zenith angle. This analysis was extended throughout the entire year. The Chappuis Depth was normalized to a solar zenith angle of 83° in order to remove the Mie scattering dependence and to allow for daily comparisons. The measured Chappuis Depth was compared with that determined from a simple single scatter model in order to derive the total column ozone (in Dobson Units) from the measurements. The ozone amounts determined from the measured data were comparable with those determined by TOMS. Skylight spectra collected in the presence of clouds were very noisy and ignored in the data analysis. A comparison between morning and evening twilight measurements for all of the clear sky data indicated that the measured ozone column is consistently larger at sunrise.

While the preliminary data set indicates a diurnal trend in the ozone column above Saskatoon, there is no support for this conclusion from TOMS. However, the TOMS data are obtained at local noon and generally fall between the sunset and sunrise values. This supports the ozone columns measured by the DM.

6.3 Future Considerations

1. Instrument-System Refinement - A few issues have been noted with the functioning of the OSIRIS USASK Ozone Observatory that need to be addressed. These include the need to move the data from the client computer to permanent storage and the correction of a problem introduced by an occasional shutter error.

2. Cloudy Data Analysis - A more detailed analysis of the cloudy data should be made to determine the possible use, if any, for the data collected on partly cloudy and overcast days; this encompasses the majority of the collected data.

This may be useful for the development of a cloud detection system or as a method for ozone measurement during cloudy weather.

3. Radiative Transfer Refinement - The radiative transfer model needs to be improved to assess the impact of atmospheric aerosols on the measured Chappuis Depth.

6.4 Conclusion

This thesis work has successfully demonstrated the development of a useable system for scattered sunlight measurements over Saskatoon. The system is essentially autonomous and requires little user interaction or monitoring. Preliminary data have been analyzed and ozone trends have been identified from the Chappuis Depth signatures. In conclusion, the OSIRIS USASK Observatory is now operational and providing scientific data in the twilight hours for further scientific analysis.

Bibliography

Bacis, R., A. Bouvier, and J. Flaud, The Ozone Molecule: Electronic Spectroscopy, *Spectrochim Acta*, *54*, 17–34, 1998.

Berk, A., G. Anderson, P. Acharya, J. Chetwynd, L. Bernstein, E. Shettle, M. Matthew, and S. Adler-Golden, MODTRAN4 User's Manual, 1999.

Brasseur, G., and S. Solomon, *Aeronomy of the Middle Atmosphere*, D. Reidel Publishing Company, 1986.

Brewer, A., A Replacement for the Dobson Spectrophotometer, *Pure Appl Geophys*, *106-108*, 919–927, 1973.

Brewer, A., and J. Milford, The Oxford-Kew Ozone Sonde, *Proc Roy Soc Lond A*, *256*, 470–495, 1960.

Brion, J., A. Chakir, J. Charbonnier, D. Daumont, C. Parisse, and J. Malicet, Absorption Spectra Measurements for the Ozone Molecule in the 350-830 nm Region, *J Atmos Chem*, *30*, 291–299, 1998.

Burrows, J., et al., The Global Ozone Monitoring Experiment (GOME): Mission Concept and First Scientific Results, *J Atmos Sci*, *56*, 151–175, 1999.

Chapman, S., A Theory of Upper-Atmospheric Ozone, *Mem R Met Soc*, *3*, 103–125, 1930.

Chappuis, J., Sur le spectre d'absorption de l'ozone, *C R Acad Sci Paris*, *91*, 985, 1880.

CRC, *CRC Handbook of Chemistry and Physics*, 55 ed., CRC Press, 1974.

Dobson, G., A Photoelectric Spectrophotometer for Measuring the Amount of Atmospheric Ozone, *Proc Phys Soc*, *43*, 324–339, 1931.

Dobson, G., Observer's Handbook for the Ozone Spectrophotometer, *Ann Int Geophys Year*, *5*, 46–89, 1957.

Dobson, G., D. Harrison, and J. Lawrence, Measurements of the Amount of Ozone in the Earth's Atmosphere and Its Relation to Other Geophysical Conditions. Part III, *Proc Roy Soc Lond A*, *122*, 456–486, 1929.

Flittner, D., P. Bhartia, and B. Herman, O_3 Profiles Retrieved From Limb Scatter Measurements: Theory, *Geophys Res Lett*, *27*, 2601–2604, 2000.

Gotz, F. P., A. Meetham, and G. Dobson, The Vertical Distribution of Ozone in the Atmosphere, *Proc Roy Soc Lond A*, *145*, 416–446, 1934.

Komhyr, W., and R. Grass, Dobson Spectrophotometer 83: A Standard for Total Ozone Measurements, 1962-1987, *JGR*, *94*, 9847–9861, 1989.

Krueger, A., L. Walter, P. Bhartia, C. Schnetzler, N. Krotkov, I. Sprod, and G. Bluth, Volcanic Sulfur Dioxide Measurements from the Total Ozone Mapping Spectrometer Instruments, *JGR*, *100*, 14,057–14,076, 1995.

Liou, K., *An Introduction to Atmospheric Radiation*, vol. 84 of *International Geophysics Series*, second ed., Academic Press, London, 2002.

Llewellyn, E., et al., The OSIRIS Instrument on the Odin Spacecraft, *Can J Phys*, *82*, 411–422, 2004.

Mcdonald, C., Ground-Based Measurement of Ozone Using Stellar Spectra, Master's thesis, University of Saskatchewan, 2006.

NASA, NASA's Goddard Space Flight Center Atmospheric Chemistry and Dynamics Branch, The Stratospheric Ozone Electronic Textbook, 2005.

Nett, H., J. Frerick, T. Paulsen, and G. Levrini, The Atmospheric Instruments and Their Applications: GOMOS, MIPAS, and SCIAMACHY, *ESA Bulletin 106*, 2001.

Read, W., Z. Shippony, M. Schwartz, N. Livesey, and W. Van Snyder, The Clear-Sky Unpolarized Forward Model for the EOS Aura Microwave Limb Sounder (MLS), *IEEE Trans Geosci Remote Sens*, *44*, 1367–1379, 2006.

von Savigny, C., et al., Stratospheric Ozone Profiles Retrieved from Limb Scattered Sunlight Radiance Spectra Measured by the OSIRIS Instrument on the ODIN Satellite, *Geophys Res Lett*, *30(14)*, 1755, 2003.

Wilcox, B., Ground Validation of OSIRIS Scattered Sunlight Measurements, Master's thesis, University of Saskatchewan, 2002.